Template-Assisted Fabrications of Nanostructure Arrays for Gas-Sensing Applications

Dissertation

zur Erlangung des Doktorgrades

Dr. rer. nat.

vorgelegt der

Fakultät für Mathematik und Naturwissenschaften der

Technischen Universität Ilmenau

von

M. Sc. Shipu Xu

Ilmenau

TECHNISCHE UNIVERSITÄT
ILMENAU

Doktorvater und 1. Gutachter: Prof. Dr. Yong Lei

2. Gutachter: Prof. Dr. Stefan Krischok

3. Gutachter: Prof. Dr. Fengqiang Sun

Tag der Einreichung: 06.07.2018

Tag der wissenschaftlichen Aussprache: 07.11.2018

urn:nbn:de:gbv:ilm1-2018000427

Abstract

The highly-sensitive gas-sensing proposes a high requirement to a sensing platform, for which the nanostructure-array-based platform is a promising candidate. Template-assisted method is an effective strategy to prepare various nanostructure arrays. Herein, by using templates of ultrathin alumina membranes and colloidal monolayers, two kinds of nanostructure array gas sensors (i.e., nanorod arrays and films with arrayed triangular convexes) are prepared and exhibit a series of morphology origin of enhanced performances. In gas-sensing works using SnO_2 nanorod arrays, the optimized gas-sensing is achieved by adjustments of the nanorod length from 20 to 340 nm and characterized by a low detection limit of 3 ppm ethanol gas at room temperature when the nanorod length is 40 nm. For the SnO_2 film gas sensor, its triangular convex adsorption active sites can enhance surface adsorptions. By ensembles of these adsorption active sites with different periods (289, 433, 577, and 1154 nm), these samples present an adsorption active site origin of sensitivity, and being capable of detecting a low concentration of 6 ppm ethanol gas. The above morphology-to-performance correlations confirm that the template-assisted fabrications of nanostructure arrays are efficient to the fabrication of high-performance gas sensors.

Zusammenfassung

Hochempfindliche Gasdetektion stellt hohe Anforderungen an die zu verwendende Messplattform, für welche Nanostrukturarray-basierte Messfühler vielversprechende Kandidaten sind. Die Templat-gestützte Methode stellt eine effektive Grundlage zur Herstellung verschiedener Nanostrukturarrays dar. In dieser Arbeit werden mit Hilfe von ultradünnen Aluminiumoxid-Membranen oder kolloidalen Monolayern als Templat zwei verschiedene Arten von Nanostrukturarray-Gassensoren (Nanorod-Arrays und dünne Schichten mit angeordneten dreieckigen Wölbungen) hergestellt, welche aufgrund ihrer Morphologie eine erhöhte Leistungsfähigkeit aufweisen. Bei der Gasdetektion mit SnO_2-Nanorod-Arrays wurde die optimierte Gasmessung durch Anpassung der Nanorod-Länge auf 20 bis 340 nm erreicht. Charakterisiert wird sie durch eine niedriges Detektionsschwelle von 3 ppm Ethanol-Gas bei Raumtemperatur und einer Nanorod-Länge von 40 nm. Bei den SnO_2-Dünnschicht-Gassensoren erhöhen die dreieckigen konvexen Wölbungen die aktive Adsorptionsfläche für die Gasmessempfindlichkeit. Die Anordnung dieser adsorptionsaktiven Punkte mit unterschiedlicher Periodizität (289, 433, 577 und 1154 nm) zeigt eine Sensitivitätsabhängigkeit auf, wobei eine niedrige Detektionsschwelle von 6 ppm Ethanol-Gas erreicht wird. Die obigen Korrelationen zwischen Morphologie und Leistungsfähigkeit bestätigen, dass die Templat-gestützte Herstellung von Nanostrukturarrays zur Produktion von hochleistungsfähigen Gassensoren effizient genutzt werden kann.

Acknowledgement

This work begins from September 2015 to July 2018 under the supervision of Prof. Dr. Yong Lei at the Institute of Physics and the Institute of Micro- and Nanotechnologies (IMN MacroNano®), Technische Universität Ilmenau.

First and foremost, I would like to highly appreciate my advisor Prof. Dr. Yong Lei for his permanent support, guidance, and encouragement during my academic research in his group. By his active supervisions on my research projects, I can always gain very valuable suggestions when my projects are subjected to dilemmas. Apart from the academic cases, he also encourages me to improve myself by participating DPG conferences and teaching activities. These enjoyable and precious experiences are really benefit for me during past 3 years, and I would like to thank Prof. Dr. Yong Lei very much.

Additionally, I want to thank all our group members for their kind assistances in the aspects of not only academic matters but also everyday life in Ilmenau. In the aspect related to the research discussion and technique support, I like to appreciate Dr. Huaping Zhao, Dr. Yang Xu, Dr. Min Zhou, and Mr. Rui Xu for their valuable suggestions and the time dedicated. Meanwhile, I am very pleasant to work with other group members, Dr. Yaoguo Fang, Mr. Max Sommerfeld, Mr. Huanming Zhang, Mr. Long Liu, Mr. Zhiqiang Zeng, Mr. Chenglin Zhang, and Mr. Yuhang Wu in the positive and harmonious group atmosphere.

I also want to appreciate the technique supports from the Institute of Micro- and Nanotechnologies. Many thanks to Dr.-Ing. Arne Albrecht, Mr. Joachim Döll, and Dr. Henry Romanus for their time and valuable supports.

Finally, I would like to thank the supports from the China scholarship council and my family. My father always tells me that, dedicate your efforts whenever. His words have always inspired me for the past 3 years.

Table of Content

List of Figures

List of Abbreviations

AAO	Anodic aluminum oxide
UTAM	Ultra-thin alumina membrane
CMDGS	Carrier mobility dominated gas-sensing
3D	Three-dimensional
δ	Debye length
D	Grain size
CDDGS	Carrier density dominated gas-sensing
SEM	Scanning electron microscopy
XRD	X-ray diffraction
XPS	X-ray photoelectron spectroscopy
TEM	Transmission electron microscopy
TCAAS	Triangular convex adsorption active sites
KFM	Kelvin force microscopy
AFM	Atomic force microscopy
d	The inter-TCAAS spacing
n	Carrier density
R	Roughness averages
SnO_2	Tin(IV) dioxide
$SnCl_4$	Tin(IV) chloride
SiO_2	Silicon(IV) dioxide
CH_2Cl_2	Dichloromethane
Ti	Titanium
Au	Gold
In	Indium

Mo	Molybdenum
H	Enthalpy
S	Entropy
G	Gibbs free energy
ALD	Atomic layer deposition
Si	Silicon
Pt	Platinum
C	Carbon

1. Introduction

Sensing gaseous molecules is important in environmental monitoring, control of chemical process, and agriculture applications.[1] Among them, it is a constant expectation that the sensing platform will be capable of high sensitivity, rapid response time, and good long-term stability. To this end, current researches have focused on optimizations of the sensor morphology such as nanostructuring the sensing platform.[1c, 1d, 1i, 2] In this mean, the generated regular arrays of nanostructures not only exhibit the above advanced sensing features, but are also highly controllable in terms of their performances.[1i, 2b, 3]

Considering that properties of the nanostructure-array-based sensing platform are morphology- and alignment-parameter dependent, and thus creation of a large scale array with controlled morphologies and structures becomes increasingly important.[4] To this end, the widely-used techniques involve photolithography, electron beam lithography, and scanning probe lithography.[5] However, photolithography is limited by a low resolution due to its diffraction-limited resolution, *ca.* $\lambda/2$ (λ is the photowavelength), and hence it cannot be developed for precisely nanostructural fabrications.[5a] Other lithographic routes such as electron beam lithography and scanning probe lithography still cannot be afforded by the high cost and the small-sample-size throughout.

Template-assisted method is of a high efficiency in fabrications of regular nanostructure arrays, by which we can produce a large area and highly-ordered array with precisely morphological controlling. Furthermore, an optimized sensing performance is achievable by adjusting morphology parameters of the nanostructure-array-based sensing platform. To date, the most widely-used templates include colloidal monolayer and anodic aluminum oxide (AAO). [1i, 1k, 2b, 3-4, 6]

The template of colloidal monolayer is well developed for fabricating various nanostructure arrays.[4, 7] Firstly, nanospheres self-assemble into a colloidal monolayer to be used as a

template. Following fabrications can determine shapes of arrayed nanostructures. For example, vertically depositing the desirable materials on template-covered substrates can produce triangle arrays or nanohole arrays. Alternatively, the way of etching can generate ordered arrays of nanodisks, nanotips, or nanopillars. Through wetting around nanospheres, nanorings arrays can be obtained. These generated regular nanostructure arrays serve as good sensing platforms those are widely used in gas-sensing applications.[8]

As another conventional template, the AAO can be employed with a large range of desirable materials due to the chemical stability of the template aluminum oxide. By different fabrication methods, different kinds of the nanostructure arrays can also be prepared accordingly. For example, the way of electrochemically depositing active materials is widely-used in preparations of the arrays of nanowires or nanopillars, alternatively, these arrays can also be easily acquired by the conventional sol-gel process. Chemical vapor deposition method is accessible to a homogeneous coating of the desired material on the AAO template, resulting in a nanotube or a nanopore array. As one kind of AAO, ultra-thin alumina membrane (UTAM) is of a below 500 nm thickness. In 1996, UTAM was firstly used as a stencil mask for preparing nanostructure arrays, conducted by Masuda and Satoh.[9] Since then, UTAM-based method has been popularized.[10] Given by the advantages of the easy accessibility and low cost, the UTAM is intensively used as a template for preparing the nanostructure array gas-sensors.

In this dissertation, by the templates of colloidal monolayer and UTAM, I prepare different kinds of gas-sensors which are formed by a nanorod array and a film on a triangle array. For their gas-sensing, I focus on the study of the morphology-performance correlation and find the following key results:

(1) For the SnO_2 nanorod array gas-sensors, I show that carrier mobility can be an efficient parameter to dominate gas sensing, by which the room temperature gas-sensing of inorganic semiconductors is realized via a carrier mobility dominated gas-sensing (CMDGS) mode. It is

found that a key for determining gas sensing mode is adjusting the length of the arrayed nanorods. With the nanorod length changing from 340 to 40 nm, the gas sensing behavior changes from the conventional carrier-density mode to a complete carrier-mobility mode. Moreover, comparing to the carrier density dominating gas-sensing, the proposed CMDGS mode enhances the sensor sensitivity. The CMDGS proves an emerging gas-sensing mode for designing inorganic semiconductor gas sensors with high performances at room temperature. (2) In the case of gas-sensing using SnO_2 film on the triangle array, this work shows a concept of adsorption active site to efficiently fulfill the sensitive gas-sensing, where the adsorption active site on the sensor enhances surface adsorption. By depositing an SnO_2 film on the triangle array, the sensor is of an ensemble of triangular convex adsorption active sites, and exhibits an adsorption-active-site-dependent sensitivity in a room temperature detection of ethanol gases ranging from 6 to 25 ppm. Shown by the sample with the largest adsorption active site, the most sensitive gas-sensing presents a low detection limit of around 6 ppm ethanol gas. In contrast, without adsorption active sites, a flat film of SnO_2 has no gas-sensing responses even to 25 ppm ethanol gas. To investigate the adsorption-active-site-origin of sensitivity, I utilize Kelvin force microscopy and characterize an adsorption enhancement on the adsorption active site by a large surface potential variation for introducing ethanol gas. These results confirm that the creation of adsorption active sites can efficiently increase surface adsorption of a gas-sensor for realizing its sensitive gas-sensing.

The above results confirm that the morphology of nanostructure is critical to gas-sensing performs. Template-assisted method is highly accessible to preparing and controlling the nanostructure array, which thus serves as an efficient approach to prepare high-performance gas-sensors.

2. Background

(This chapter is based on my published work: Xu, S.P.; Lei, Y.* Template-Assisted Fabrications of Nanostructured Arrays for Sensing Applications. *ChemPlusChem* **2018**, *83*, 741-755.)

2.1. Templated-Assisted Fabrications of Nanostructure Arrays.

By template-assisted methods, various arrays of nanostructures can be prepared as a gas-sensing substrate and exhibit high-sensing performances based on their advanced morphology features. As shown in Figure 2-1, these morphology advantages include: (i) the high-density alignment of arrayed nanostructures; (ii) the high surface-to-volume ratio; (iii) the convex-rich morphology. The arrays with the high-density alignment are highly accessible for the ensemble of per sensing signal from each unit of sensing blocks, resulting in a largely enhanced sensitivity for the gas detection. Additionally, by using the template of UTAM, we can also obtain the nanostructure arrays such as nanorod arrays, which are of a high sensitivity because of their large specific surface area. To acquire the arrays with the convex-rich morphology, another conventional template, the colloidal monolayer, is intensively utilized. Such convex-rich morphology is particularly sensitive to the environment changes due to its sharp corners and edges.

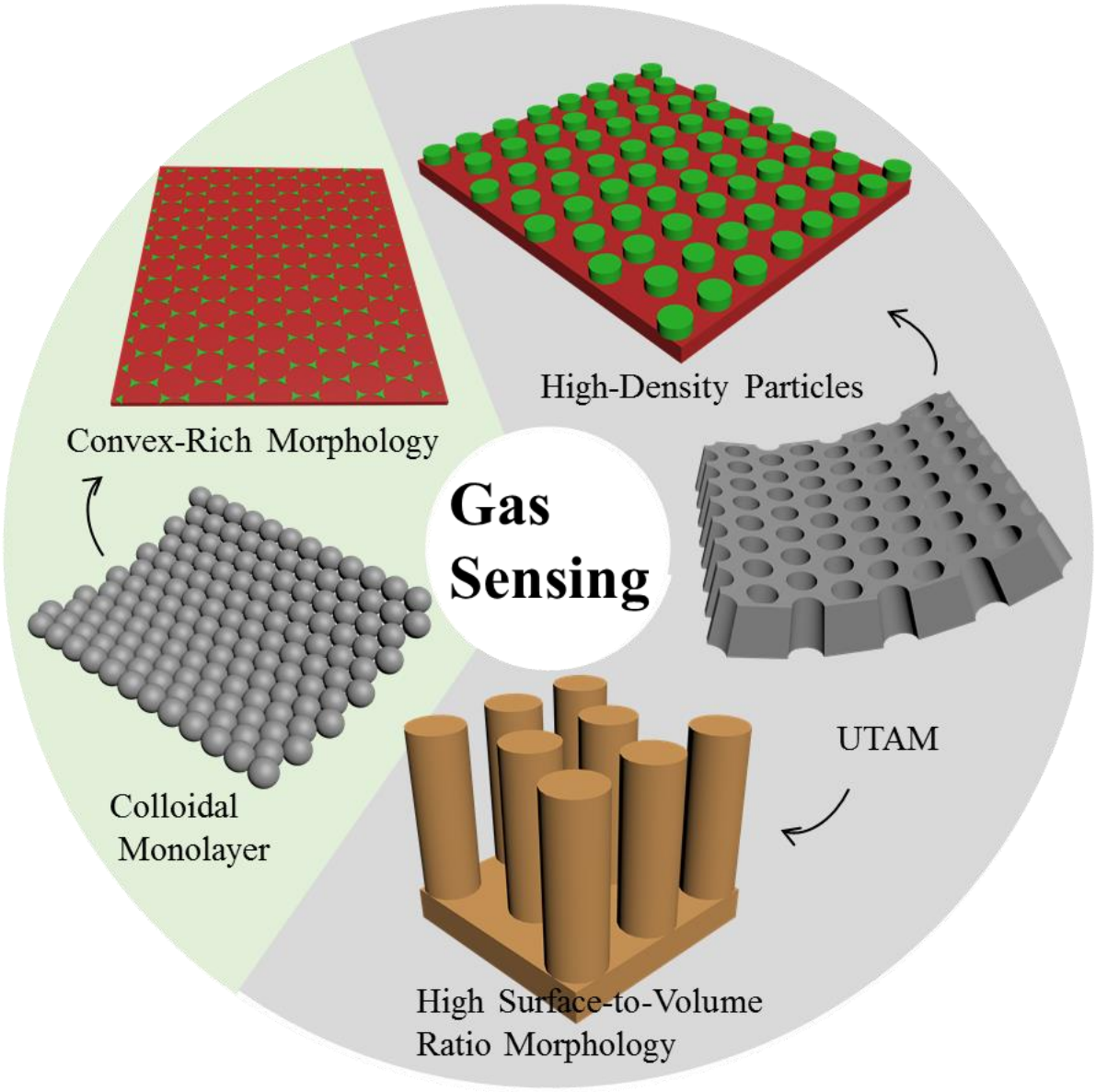

Figure 2-1. Schematic illustration showing template-assisted fabrications of nanostructure arrays those are of advanced morphology features, including high-density alignment of arrayed nanostructures, high surface-to-volume ratio, and convex-rich morphology.

2.1.1. UTAM-Assisted Fabrications of Nanostructure Arrays.

2.1.1.1. The UTAM Morphology.

UTAM, one kind of AAO, is of an ultra-thin thickness compared to the normal AAO. As shown in Figure 2-2a, the schematic diagram of the UTAM shows three its morphology parameters: (i) pore diameter, (ii) thickness and (iii) inter-pore spacing. The ranges of pore diameters and thickness can be 5-80 nm and 100-500 nm, respectively. The adjustment of these two

morphology parameters is based on turning the times of wet-etching and oxidation process respectively. The normal inter-pore spacing remains the value of 110 nm. Figure 2-2b and c show a plane and a tilted view of scanning electron microscopy (SEM) images of the UTAMs on the substrate, where the pores are regularly arranged in hexanol for a large area.

For fabrication of UTAM, its morphology is formed by electrochemical anodization of aluminum in liquid electrolytes with the balance between the growth and the localized dissolution of aluminum oxide. In this mean, an aluminum fossil with a compact oxide layer is anodized under a constant voltage, in which inhomogeneities of the oxide layer can induce locally focused electric fields at the oxide–electrolyte interface. These local electric fields allow electric-field-assisted dissolutions of the oxide layer, resulting in the localized pores. At this stage, these initial pores are ununiform, and serve as the sites for the further pore growth. By prolonging the anodization, the pore order can be improved, and the pore growth process reaches a steady state for forming uniformly distributed pores

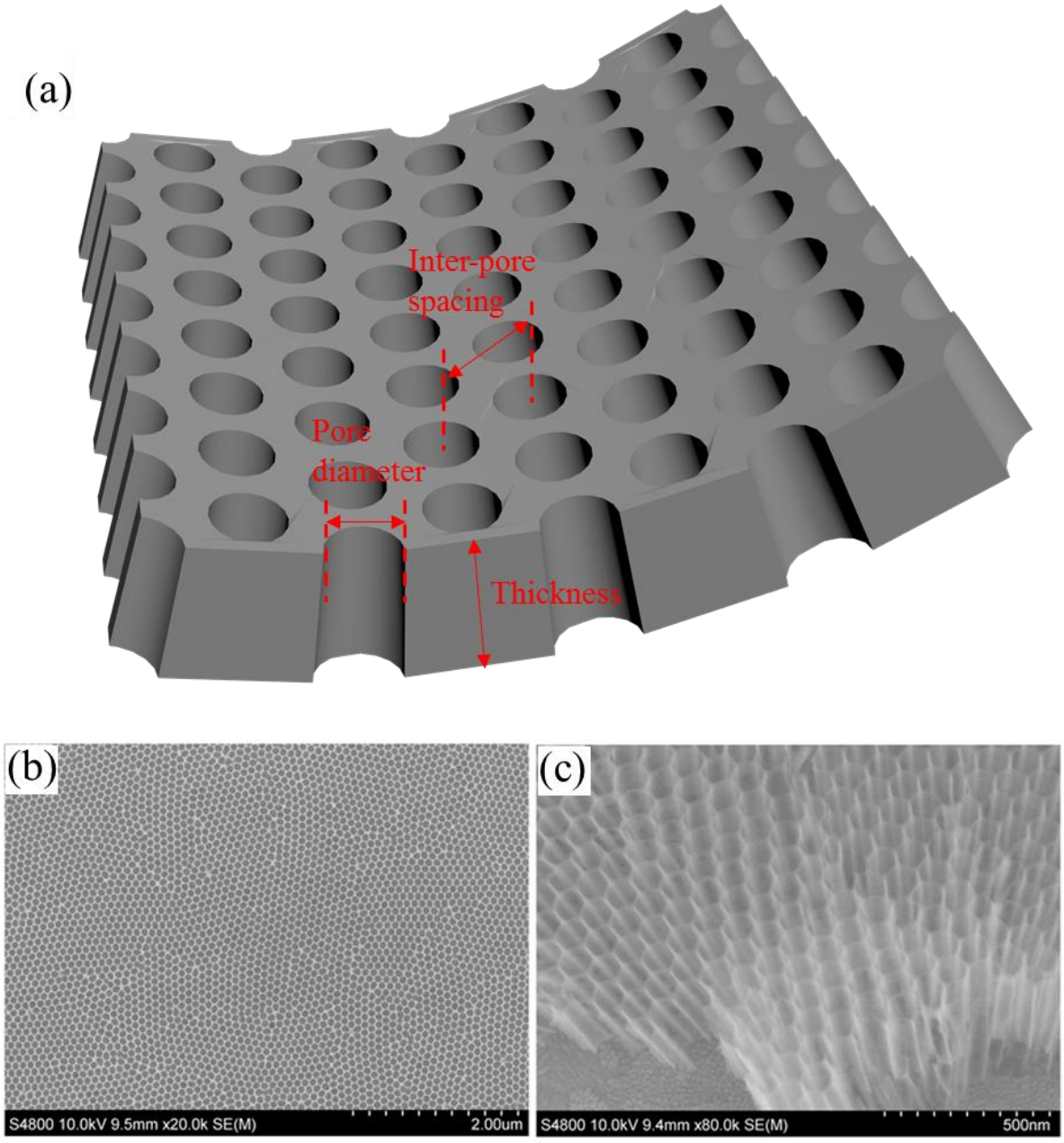

Figure 2-2. (a) The schematic diagram of the UTAM. SEM images show a plane (b) and a tilted view of the UTAM (c) on the substrate, respectively. Reproduction with permission from Ref. [10d]. Copyright 2018, American Chemical Society.

2.1.1.2. UTAM-Based Methods.

In 1996, UTAM was firstly used as a stencil mask for preparing nanostructure arrays, conducted by Masuda and Satoh.[9] Since then, UTAM-based method has been popularized.[10] As compared to the other nanostructure patterning techniques (e.g., electron-beam direct

writing, focused ion beam milling, and nanoimprinting lithography), the UTAM-based way exhibits the unique advantages of the easy accessibility and low cost.

Figure 2-3 summarizes UTAM-based methods to nanostructure fabrication.[11] These methods begin with fabricating UTAMs on substrates, in which two kinds of UTAMs can be constructed on the substrate: (i) attached UTAM (A1-A2-A3) and (ii) connected UTAM (B). Using such UTAMs on substrates, Figure 2-3 shows four fabrication routes to prepare nanostructure arrays (Routes I–VI). Through evaporation or sputtering processes, nanodot arrays can be fabricated on substrates (Route I: a1-a2) followed by the removal of the UTAM. At the same time, the evaporated material also accumulates on the UTAM surface to form a porous layer. The pores of this layer will be closed by the further evaporation, and generating nanoring structures on the bottom surface of this layer (a3). By transferring to the surface of another substrate, a film with nanoring features can be obtained (Route II: a1 - a3 - a4). Based on the template of UTAMs, the nanopillar arrays are easily accessible by various ways. For example, via evaporation, wet-chemical or polymerization process, the nanopillar arrays can be synthesized on the top of an UTAM (b1). Alternatively, these kinds of nanopillar arrays can also be attached on another substrate from the backside and be separated from the UTAM (Route III: b1 - b2 - b3). For preparations of nanohole arrays, fabrication routes such as using reactive ion or plasma etching processes can excavate nanoholes on substrates (c1). After removing the UTAM, ordered nanohole arrays on substrates are acquired (Route IV: c1 - c2). Note that during the etching process, eliminating the etching ions and radicals bouncing at the gap between the mask and the substrate needs a conformal contact of the UTAM to the underlying substrate. The conformal contact is critical to realize the regularity of the generated structure. To this end, conducted by Jung et. al., poly(methyl methacrylate) (PMMA), the contact layer, was spin-coated on surface of the Si substrate prior to transferring the AAO membrane. This additional step enhanced

the ordered degree of the nanohole array, where the introduced PMMA interlayer avoids unwanted surface etching of the Si substrate, resulting in a smooth Si nanopore array.[10c]

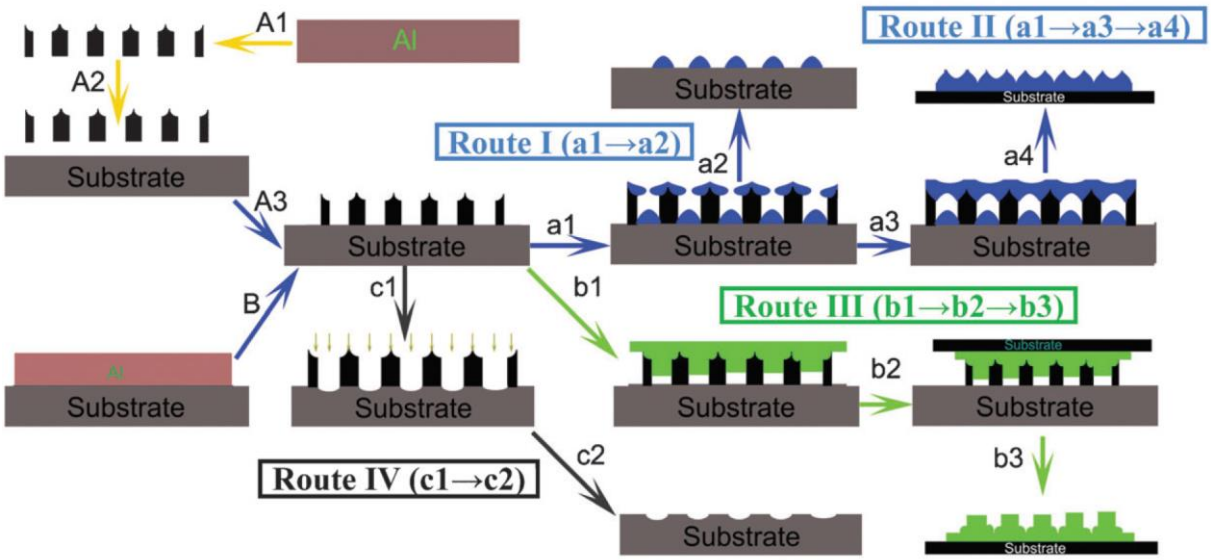

Figure 2-3. Schematic illustration (cross-sectional view) of the UTAM-assisted fabrication of nanostructure arrays. Two types of UTAMs are prepared on substrates: attached UTAM (A1-A2-A3) and connected UTAM (B). Herein, four routes are shown for preparations of nanostructure arrays (Routes I-VI): (I) nanodot arrays (a1-a2), a1: evaporation, a2: removing UTAM; (II) nanoring arrays (a1-a3-a4), a3: further evaporating until the UTAM pores are fully capped, a4: removing the top layer and transferring to another substrate; (III) nanopillar arrays (b1-b2-b3), b1: filling in the UTAM pores, b2: adhering another substrate on the top, b3: removing UTAM; (IV) nanohole arrays (c1 - c2), c1: the ion or the plasma etching, c2: removing UTAM. Reproduction with permission from Ref. [11]. Copyright 2011, The Royal Society of Chemistry.

2.1.2. Colloidal-Monolayer-Assisted Fabrications of Nanostructure Arrays.

2.1.2.1. Colloidal Monolayers by Self-Assembling.

Firstly reported by Fischer and Zingsheim in 1981, nanospheres self-assemble into a colloidal monolayer on a glass plate.[12] Since then, colloidal monolayer has attracted great attentions as

a template for fabrication of nanostructure arrays, and recently the group of Van Duyne has improved the colloidal monolayer-based technology greatly.[13]

The monolayer colloidal is formed by a monolayered colloidal nanosphere array with the hexagonal-closed-packed arrangement, and can be obtained by a self-assembling process. In this mean, nanospheres are firstly dispersed in the solution, being impacted by the interactions containing Van der Waal, steric repulsion, and Coulombic repulsion. These interactions govern the stable dispersion of the nanospheres in a solution.[7b] The following evaporation of the dispersion solution will induce the self-assemble of the nanospheres, where the attractive capillary forces between the nanospheres is critical to their regular alignment. The high quality of the colloidal monolayer relies on the well-controlling of the attractive capillary forces during the drying stage. In order to acquire the high quality of the colloidal monolayer, various self-assembling ways have been developed and introduced in the following sections.

Dip-coating is an efficient and simple strategy to self-assemble monodispersed nanospheres into a colloidal monolayer.[14] Figure 2-4a schematically presents the dip-coating process, where the ordering process of the component nanospheres begins at the moment when the liquid level of the suspension becomes lower than the top surface of the nanospheres because of the evaporation of the liquid. Then a meniscus between the neighboring nanospheres occurs and generates attractive capillary forces those induce the nanospheres from a ununiform distribution to be a regular two-dimensional (2D) array. Note that the capillary forces are allowed only at the triple point of the suspension/substrate/air interface during the evaporation. The evaporation rate dominates the quality of this ordered arrays. For controlling the evaporation rate, a step motor can be utilized to slowly lift up the wet substrate from the colloidal suspension.[15] In this method, a large-scale monolayer composed of a nanospheres diameter ranging from hundreds of nanometers to a few micrometers can be acquired.

As compared with the method of dip-coating, spin-coating is a fast method to prepare colloidal monolayer.[16] As illustrated in Figure 2-4b, during spin-coating, the solvent flows across the substrate at a certain shear rate, while the nanospheres are densely and rapidly packed on the substrate by capillary forces and shears. The quality and thickness of nanosphere array is a product of the spin speed, the colloidal-suspension concentration, the suspension rheology, the substrate wettability, and different charge between substrate and nanospheres. By the modulation of self-assembling conditions, a high-quality colloidal monolayer can be rapidly obtained.

For the accessible fabrication of the colloidal monolayer on the desired substrate, we can let nanospheres self-assemble at the air-liquid interface. This way begins with the modification of the surface hydrophobicity of the substrate. Then the nanospheres on the substrate intend to move to the air-liquid interface, self-assembling into a colloidal monolayer (Figure 2-4c).[17] Subsequently, the generated colloidal monolayer can be transferred onto the desired substrate, regardless of surface polarity, roughness, or curvature.[18]

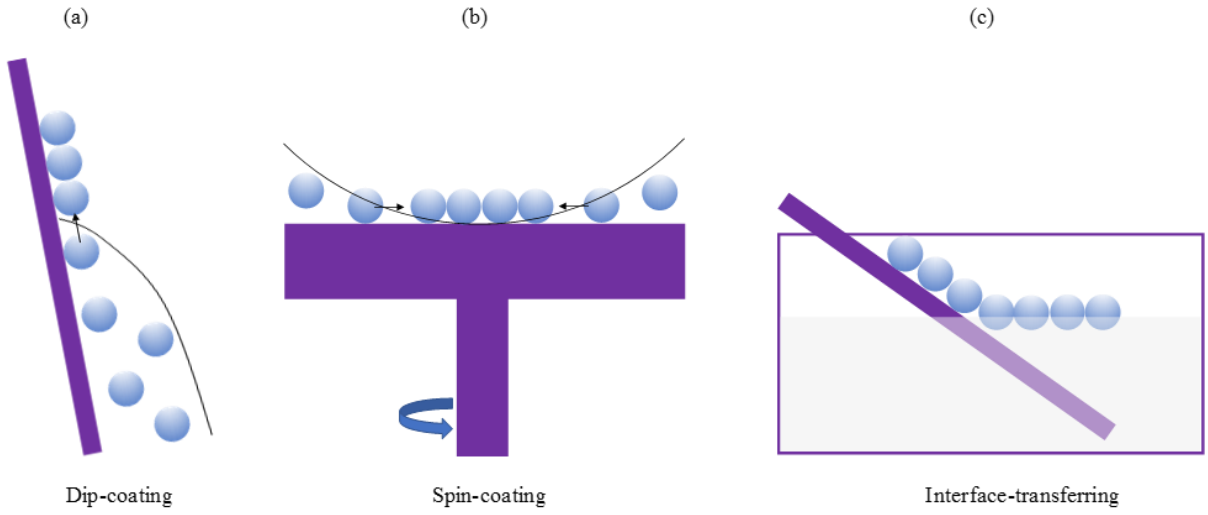

Figure 2-4. Strategies of self-assembling nanospheres into a colloidal monolayer. (a) Dip-coating in which capillary forces and evaporation induce nanosphere self-organizations. (b) Spin-coating in which capillary forces and shear drive nanosphere self-organizations. (c) Interface-transferring in which nanospheres self-assemble on the air-liquid interface.

2.1.2.2. Colloidal Monolayer-Based Methods.

Using a colloidal monolayer as a template, different fabrication methods are accessible for arrays of different nanostructures. As shown in Figure 2-5, depositing desired materials on template-covered substrates is a conventional method to generate a nanostructure array with a high-density alignment.[19] In this mean, the sputtering instruments, such as a magnetron sputter, e-beam, or a thermal evaporator, can be used without limitations of the deposited materials. In Figure 2-5, arrays of triangular nanoparticles and rounded nanoparticles can be prepared with a non-rotating (i) and a rotating substrate (iv), respectively; alternatively, by tilting the sputtering direction, a crescent-shaped nanoparticle array can be obtained (ii); a complete depositing on both two sides of the colloidal monolayer is accessible to a hollow nanosphere array on the substrate (iii).

As another method, the etching process can produce a nanohole array through the template-covered substrate. Turning the etching orientation and time, the morphology of the generated nanopatterns such as the depth can be adjusted directly. Further etching can not only induce a larger depth, but also narrow the connect neck between nanospheres and the substrate to produce a three-dimensional (3D) nanostructure array.[20]

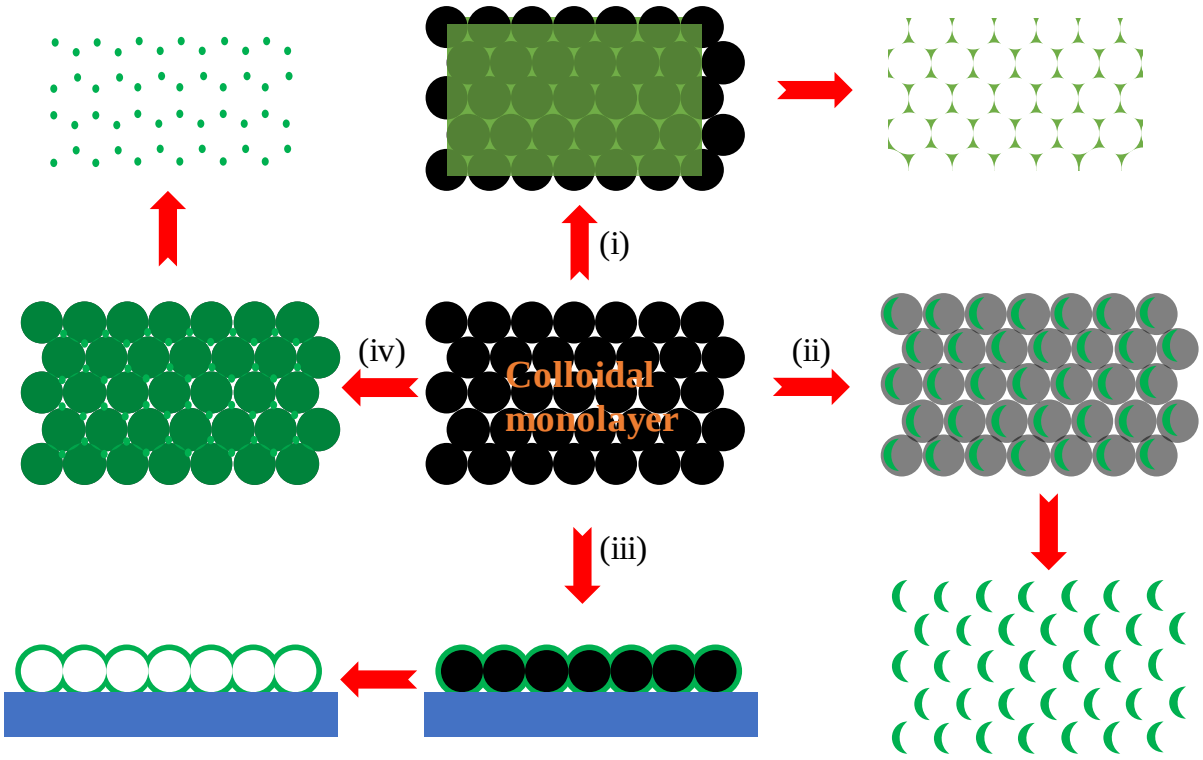

Figure 2-5. Schematic illustration of colloidal-monolayer-assisted depositions for fabrications of nanostructure arrays. Four widely-used processes of the deposition are presented as follows: (i) and (iv) vertically depositing on a non-rotating and a rotating colloidal-monolayer-cover substrate; (ii) depositing on the substrate in a tilted direction; (iii) completely depositing on both two sides of the colloidal monolayer.

2.2. Metal Oxide Gas Sensors.

Metal oxide gas sensors are the most widely used solid state gas sensors due to the advantage features of low cost and high sensitivity. The working principle of metal oxide gas sensors relies on the variation in electrical properties for the gas adsorption, and this method is highly available for the practical applications. Table 2-1 compares different types of gas sensors, some of which are based on the methods such as electro-chemical reactions.[1l]

Table 2-1. Comparison of Different Types of Gas Sensors.[a)]

Parameters	Types of Gas Sensors				
	Metal Oxide Gas Sensors	Catalytic Combustion Gas Sensors	Electro-Chemical Gas Sensors	Thermal Conductivity Gas Sensors	Infrared Absorption Gas Sensors
Sensitivity	Excellent	Good	Good	Poor	Excellent
Selectivity	Fair	Poor	Good	Poor	Excellent
Response Time	Excellent	Good	Fair	Good	Fair
Stability	Good	Good	Poor	Good	Good

a) Reproduction with permission from Ref. [1l]. Copyright 2007, Elsevier.

Table 2-1 compares different types of gas sensors regarding the features of sensitivity, selectivity, response time, and stability. It is found that, the metal oxide gas sensors process an excellent performance in sensitivity and response, but being with a fair selectivity. As compared to the other type of gas sensors, the advantages of the metal oxide gas sensors such as the short time response enable their wide usage in the emergency events.

2.2.1. Adsorption on the Surface.

The interaction between gaseous molecules and solid surface is a fundamental process that provides an understanding of the working principle of gas sensors, during which adsorption is an initial stage. In the adsorption, molecules, atoms, or ions are attached to a solid surface. According the types of attractions between adsorbates and the solid surface, there are two types of adsorptions: (i) physical adsorption and (ii) chemisorption. Physical adsorption is a weak

adsorption, where the interact forces involve intermolecular forces such as Van der Waal force but do not induce a substantial change in the electronic orbital of the species. It is considered that physical adsorption is reversible and non-activated, whereas chemisorption is irreversible at a certain temperature. In the case of chemisorption, the interact forces involves valence forces as those occurring in the formation of chemical compounds. Additionally, chemisorption includes ionosorption, in which atoms or molecules are ionized through capturing electrons from the bulk during the adsorption process.

Figure 2-6 shows the Lennard-Jones potential-energy diagram, where the energy of the system is plotted against the distance of the adsorbates from the surface. In cure A, the energy of the adsorbate molecule works as a function of the distance, where the lowest energy exists when the molecule reaches a distance d_p from the surface. In this condition, the physical adsorption occurs with ΔE_p. In contrast, curve B presents the energy system if two atoms are close to the surface. The strong chemisorption, with ΔE_c, occurs as the atom has a distance d_c from the surface.

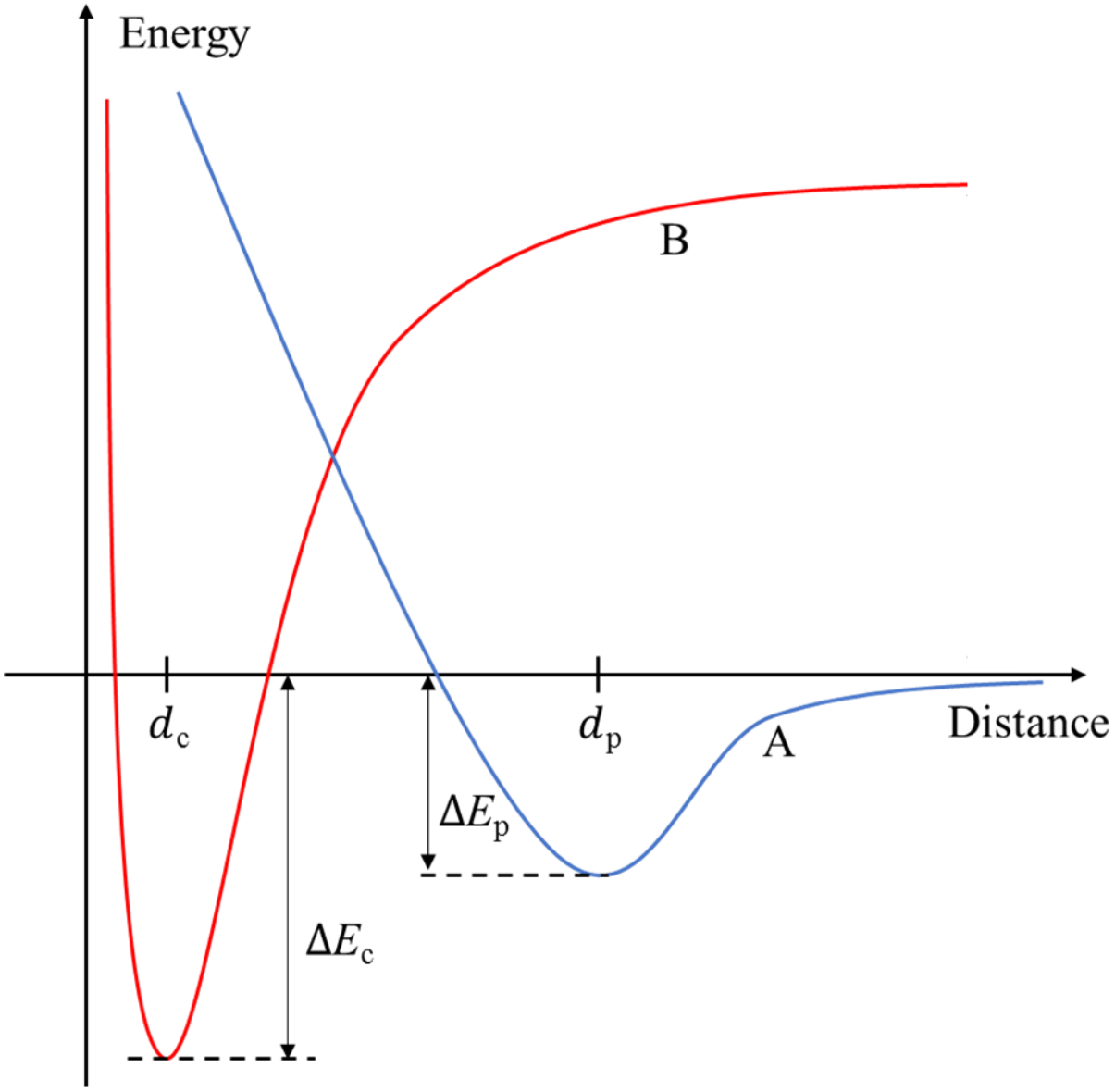

Figure 2-6. Lennard-Jones potential-energy of physical adsorption and chemisorption: A, physical adsorption of molecules; B, chemisorption of molecules.

Oxygen chemisorption on SnO_2 is a typical chemisorption, and its adsorption process is regarded as a model for the other metal oxides gas sensors. When SnO_2 is put in air, many atmospheric oxygen molecules can be adsorbed on its surface, and following reaction happens:

$$O_2 \xrightarrow{e^-} O_2^- \xrightarrow{e^-} 2O^-$$

where at room temperature O_2 is mainly physically adsorbed, and as the temperature increases, the adsorbed O_2 traps electrons from the SnO_2 to form oxygen ions such as O^- on the SnO_2 surface.[1m]

2.2.2. Performance of Gas Sensors.

The performance of gas sensors can be evaluated by different parameters, including sensitivity, selectivity, response time, and stability. Sensitivity is usually defined as the ratio of the resistances in air and in the detecting gas. Sensitivity can reflect the detection limit of a gas sensor, where the high sensitive gas sensor is of a low detection limit. Selectivity is the ability of the gas sensors to distinguish a specific gas from a mixture of gases. The response time is defined as the time required for reaching 90% of the equilibrium value in the detecting atmosphere. Stability manifests as a property of a gas sensor to reproduce results for a certain period. For a gas sensor with high performances, we expect that this sensor could be capable of high sensitivity, high selectivity, the short time response, and good long-term stability.

2.2.3. SnO_2 Gas-Sensing.

2.2.3.1. Progress of SnO_2 Gas-Sensing Study.

SnO_2, one kind of conventional gas-sensing materials, is widely-used in solid-state gas sensors due to its low cost and high gas-sensing sensitivity. During the period of 1998-2017, the total publications related to the SnO_2 gas-sensing is increasing per year (Figure 2-7a). Meanwhile, the sum of times cited by year also shows an increasing tendency, where the sum of times in 2017 is up to 15612 (Figure 2-7b). It is confirmed that the study on the SnO_2 gas-sensing arouses researchers more and more interests. Recently, most works about the SnO_2 gas-sensing have focused on nanostructuring SnO_2 for the sensitive gas-sensing. Among them, template-assisted method is intensively reported as an effective strategy to prepare the SnO_2 nanostructure gas sensors with high sensing performances.

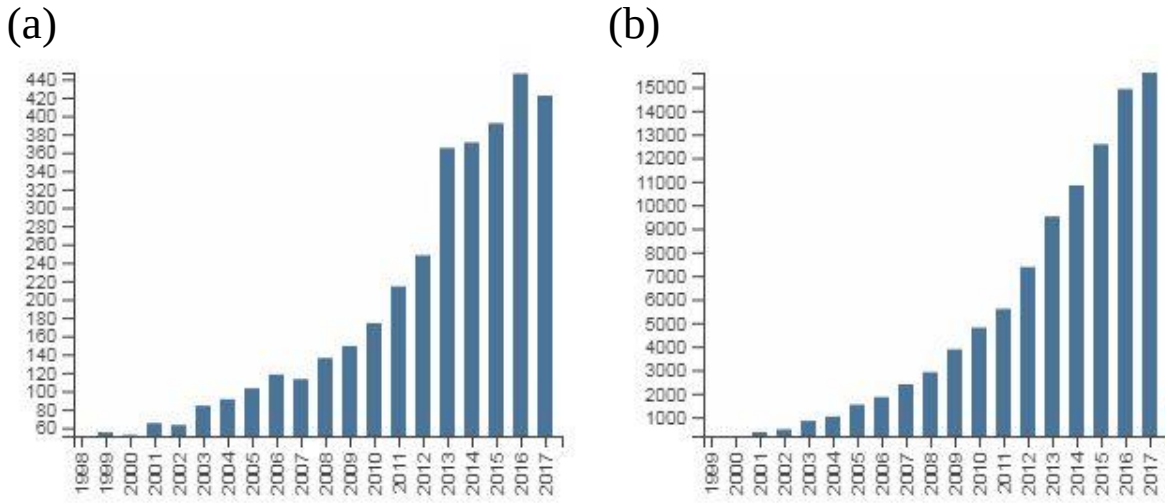

Figure 2-7. The published works related to SnO_2 gas-sensing during 1998-2017. (a) Total publications by year. (b) Sum of times cited by year. The data is from Web of Science.

2.2.3.2. SnO_2 Gas-Sensing Modes.

Among a broad variety of gas-sensing materials, SnO_2 has been subject to the largest number of studies.[21] Its sensing behaviour to ethanol[21b] provides a definitive example for realizing the correlation between adsorbed surface species and conductivity in semiconductor metal oxides. Meanwhile, it has set the basis for two general descriptions[22] of the sensing mechanism: (i) the oxygen-vacancy model (reduction-reoxidation mechanism)[22-23] and (ii) the ionosorption model.[21b, 24] Both gas-sensing models can describe all the experimental observations, where this work mainly concentrates on the ionosorption model which can serve as a guideline for understanding the structural-functional relation of nanostructured SnO_2 materials.

In the ionosorption model, the SnO_2 gas-sensing involves two stages: (i) the stage in air and (ii) the stage after introducing target gas. In air, the SnO_2 physisorbes oxygen species. These oxygen species can trap electrons from SnO_2 to form as free oxygen ions electrostatically stabilized on the oxide surface (Figure 2-8a). These ions can scatter electrons within the Debye length δ of the SnO_2 (3 nm for SnO_2 at 250℃), generating a depleted region with reduced

electron mobility near the oxide surface.[22] The formation of the depleted region thus results in a reduction of the SnO_2 conductivity. If a reducing analyte is inserted, the reaction between the reducing analyte and the ionosorbed oxygen (b) will decrease these scattering centers (O^-) and releases the trapped electrons, thereby increasing the SnO_2 conductivity (Figure 2-8b). Under this mode, the conductivity change mainly relies on the ratio between grain size (D) and 2-times Debye length.[21b] If $D \gg 2\delta$ (Figure 2-8c), the ratio between the depletion width and the grain size is very low. Then only a small part of the semiconductor is affected by its interaction with the analyte, resulting in a low sensitivity for the sample. If $D > 2\delta$ (Figure 2-8d), a conduction channel with high conductivity exists but its wideness (Lc) is controlled by the surface concentration of oxygen ions. In this case, for example, the introduced ethanol gas leads to moderate sensitivities. If $D \leq 2\delta$ (Figure 2-8e), the whole grain is depleted and changes in the surface oxygen concentration largely affects the whole semiconductor to induce a high sensitivity.[25]

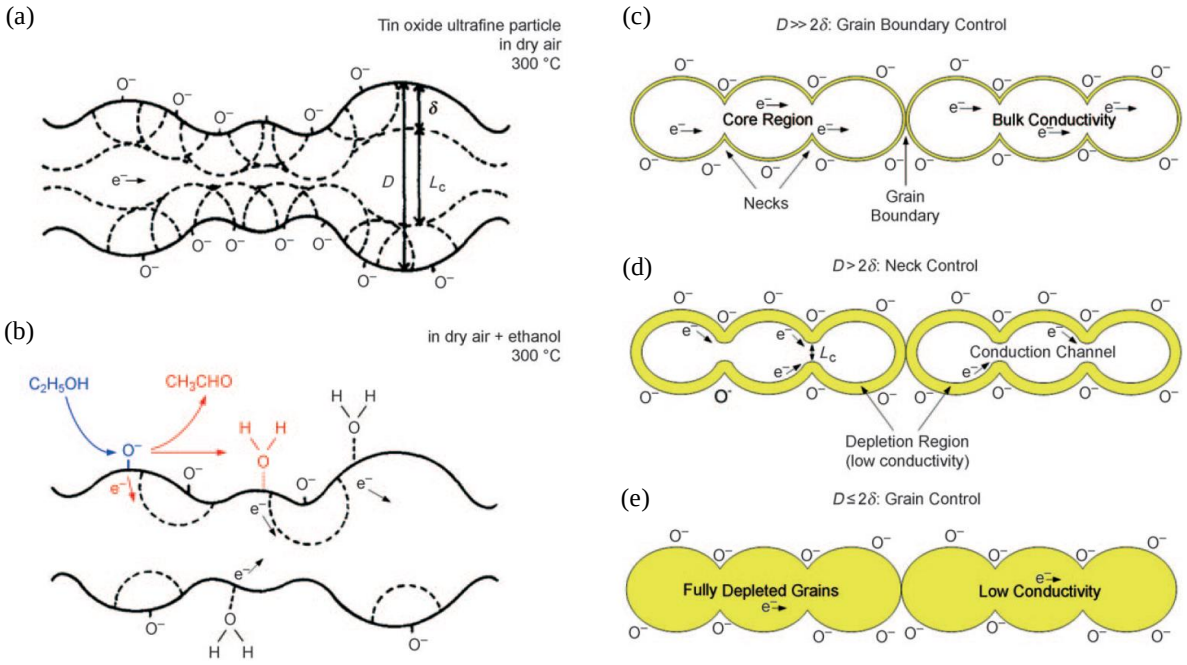

Figure 2-8. Schematic model of oxygen ionosorption on the SnO_2 surface in pure dry air and with ethanol. (a) The adsorbed oxygen species trap electrons from SnO_2 to form oxygen ions, O^-, on the surface. (b) The reaction between ethanol and the adsorbed oxygen ions decreases

the scattering centers and releases the trapped electrons to increase the SnO_2 conductivity. (c) When $D \gg 2\delta$, a low sensitivity to the analyte is expected as only a small part of the semiconductor affected by interaction with the analyte. (d) When $D > 2\delta$, a moderate sensitivity exists for the fact that the conduction channel is controlled by the surface concentration of oxygen ions at a limited level. (e) As $D \leq 2\delta$, the whole grain is depleted and changes in the surface oxygen concentration affect the whole semiconductor to induce a high sensitivity. Reproduction with permission from Ref. [25]. Copyright 2004, American Institute of Physics.

3. UTAM-Assisted Fabrications of SnO_2 Nanorod Array Gas Sensors

(This chapter is based on my published work: Xu, S.P.; Zhao, H.P.; Xu, Y.; Xu, R.; Lei, Y.* Carrier Mobility-Dominated Gas Sensing: A Room-Temperature Gas-Sensing Mode for SnO_2 Nanorod Array Sensors. *ACS Applied Materials &Interfaces* **2018**, *10*, 13895-13902.)

3.1. Design Concept of SnO_2 Nanorod Array Gas Sensors.

Inorganic semiconductor gas sensors are most wildly-used solid-state gas sensors owing to their high sensitivity, fast-response time, and high chemical stability.[1a, 1b, 26] Development of inorganic semiconductor gas sensors is dependent on gas-sensing modes, among which the dominant gas-sensing mode relies on a fact that surface adsorption on inorganic semiconductors can influence their carrier density to vary the conductivity.[24, 27] The surface adsorption origin of the carrier density variation is the key to this dominant gas-sensing mode, which is therefore denoted as 'carrier density dominated gas-sensing' (CDDGS) in the following description. Operating the CDDGS needs a high temperature. For example, the operating temperature for an SnO_2 gas sensor is usually higher than 200 ºC,[27] which may cause tedious operations, over-consumptions of energy, and even some safety issues when such a CDDGS-mode gas sensor is employed.

Besides carrier density, other crucial carrier characteristics of gas-sensing materials such as carrier mobility might also play a key role for gas sensing.[28] It has been shown that hydrogen detection using platinum nanowires is related to adsorption-induced degradation of carrier mobility.[28a, 28b] Actually, a similar adsorption-origin of the carrier mobility degradation also exists in inorganic semiconductor gas-sensing, but only being limited on the surface.[1b, 21b] In the case of the oxygen adsorption on the SnO_2 film,[21b] an oxygen molecule is adsorbed and forms a scattering center on the surface of SnO_2. This scattering center radiates a spherical region with Debye length (*ca.* 3 nm), and carrier mobility is distinctly diminished within this region. This region can completely occupy the carrier channel as the thickness of the SnO_2 film

decreases to 2-times Debye length, generating a carrier mobility degradation for most carriers. Recently, the adsorption-induced degradation of carrier-mobility has also occurred when using a 4.8-nm-thin phosphorene nanosheet to detect NO_2 gas.[1b] The 4.8 nm thickness of the phosphorene nanosheet causes that the adsorbed NO_2 molecules can directly diminish the carrier mobility through the carrier channel. The resulting degradation of carrier mobility is positively associated with the concentration of NO_2 gas. However, limited by the low surface area of the above-mentioned platforms (e.g., the SnO_2 film and the phosphorene nanosheet), the adsorbed quantity of the oxygen molecule or the NO_2 molecule is still far from achieving a carrier mobility degradation which is large enough to produce an obvious variation of conductivity, and consequently so far such carrier mobility degradation has not been utilized to dominate gas-sensing of inorganic semiconductors.

Based on these recognitions and considering a fact that carrier mobility has a positive correlation with the conductivity of inorganic semiconductors, it shall be worthy to explore a concept of carrier mobility dominated gas-sensing (i.e., CMDGS) as an alternative gas-sensing mode of inorganic semiconductors. Here we design a gas-sensing configuration of inorganic semiconductors to realize the CMDGS, aiming at room-temperature gas-sensing. This design involves two key points: (i) vertically aligned nanorods and (ii) a bottom film. The inter-electrode bottom film specifically serves as a conductive channel, and the carrier mobility within the channel could be modulated by a large adsorption on the nanorods.

As a proof-of-concept, SnO_2, a traditional inorganic semiconductor for gas-sensing,[29] is chosen as a model material; and an ultra-thin alumina membrane (i.e., UTAM)[10b, 30] is applied as a template. Regular arrays of SnO_2 nanorods on a bottom film are then fabricated with different nanorod lengths (340, 140, 110, and 40 nm), which are used to construct a room temperature gas sensor. It is found that, when the nanorod length decreases from 340 to 40 nm, the gas-sensing mode changes from the carrier density dominated gas-sensing (i.e., CDDGS)

to carrier mobility dominated gas-sensing (i.e., CMDGS). For the 340-nm-length nanorod array, its gas sensing still stays in CDDGS, while the CMDGS mode appears for the 140-nm-length nanorod together with CDDGS. With further decreasing of nanorod length, the CMDGS becomes obvious for the 110-nm-length nanorod array, and finally the gas sensing of the 40-nm-length nanorod is completely in the CMDGS range. Importantly, the CMDGS-mode sensor (i.e., 40-nm-length nanorod array) shows a more than 4-times higher sensitivity compared to that of the CDDGS-mode sensor. To fully understand the mechanism of the changing from CDDGS to CMDGS mode, two representative SnO_2 nanorod arrays (40 and 340 nm nanorod lengths) are fabricated into field-effect transistors. For all three target gases of ethanol, acetone, and isopropanol, electric characterizations of the field-effect transistors show that the carrier mobility of the 40-nm-length nanorod array decreases for more than 90% after introducing gases. Together with the morphological origin of electric field distributions, a large adsorption-induced degradation of carrier mobility is demonstrated for the 40-nm-length nanorod array, endowing it with sensitive responses of CMDGS at room temperature. Based on the above, the proposed CMDGS is confirmed as an efficient gas-sensing mode for obtaining a room temperature gas sensor with high sensitivity.

3.2. Experiment and Instruments.

3.2.1. Synthesis of UTAMs.

UTAMs were synthesized from high purity Al foils by a two-step anodization process. This anodization process included a 6-hour-first and a short-time-second anodization, at 40 V in 0.3 M oxalic acid. The second anodization was conducted at 2 ºC. The UTAMs with 80, 110, 140, and 340 nm of thicknesses can be respectively obtained by 2, 3, 5, and 10 minutes of the second anodization. Next the samples were correspondingly transferred into a 5 wt% H_3PO_4 solution at 30 ºC for 4, 8, 15, and 25 minutes to widen the pore diameter up to 60 nm. A polymethylmethacrylate (i.e., PMMA) layer formed by 6% PMMA/Chlorobenzene solution

was subsequently deposited on the top of the Al layer to support the UTAM. The Al layer on the backside of the UTAM/PMMA was removed in a mixture solution of $CuCl_2$ and HCl. With the aid of a plastic strainer, the UTAM/PMMA was transferred in the H_3PO_4 solution at 30 ºC for 14 minutes to remove the barrier of the UTAM. After removal of the PMMA in acetone, the UTAM with uniform opened pores was obtained.

3.2.2. Fabrication of SnO_2 Nanorod Arrays.

Different weights of $SnCl_4$ were dissolved in deionized water to form homogeneous transparent solutions with different concentrations, ranging from 0.01 to 0. 1 M. Herein, the 0.1M and the 0.01 M $SnCl_4$ aqueous solution represented the high and the low concentration precursor solution, and were used for the fabrications of the long (i.e., 340, 140, and 110 nm nanorod length) and the short (i.e., 40 nm nanorod length) SnO_2 nanorod array. As shown in Figure 3-2a, a UTAM was slowly immersed into an $SnCl_4$ aqueous solution, and then it was floated onto the surface of the solution. Subsequently, this floated template was picked up with a device substrate. Next the sample was annealed using a heat-treatment process normally for achieving nanocomposites or nanoparticles, in a furnace with a first hot plate at 150 ºC for 2 hours and an immediate second hot plate at 450 ºC for 2 hours. Finally, the SnO_2 nanorod array was obtained after the removal of the UTAM in a H_3PO_4 solution (5 wt%).

3.2.3. Gas-Sensing Tests.

Gas-sensing tests were conducted in an air-tight chamber with electrical feedthroughs. A constant voltage of 4 V was applied to a device and the variation of the output current was monitored and recorded with the change in the gas environment using a Keithley semiconducting testing system. The reducing gases (25 ppm of ethanol, propanol, and acetone gases) were respectively chosen as a target gas. A typical gas-sensing measurement consists of three sequential steps: (1) a base value of the output current from the sensor in air was recorded; (2) a calculated volume of the reducing gas was introduced into a chamber, and the signal on

the variation of output current was simultaneously recorded; (3) after the signal stabilized, the chamber was opened for removing the gas, and the signal of the output current was also simultaneously recorded until it reached a steady state. Characterizations of the field-effect transistor were also conducted by this sensing system.

3.2.4. Characterizations.

The morphology of SnO_2 nanorod arrays on device substrates was examined by scanning electron microscopy (i.e., SEM, S4800 Hitachi and Quanta 250 FEG). The compositions were characterized by X-ray diffraction (XRD, D/max2200, with Cu-Ka radiation) and X-ray photoelectron spectroscopy (XPS, ESCALAB 250). Samples for these measurements were prepared on silicon (Si) substrates under the same conditions as those prepared on the device substrate. For preparing the specimens of transmission electron microscopy (TEM), the SnO_2 nanorod array was scraped off and transferred onto carbon-coated transmission electron microscopy grids. A JEOL JEM 2010 transition electronic microscope was used for the TEM analysis.

3.3. Results and Discussions.

3.3.1. Simulated Electric Field of the SnO_2 Nanorod Array and Its CMDGS mode.

To reveal a possibility of the CMDGS mode based on the designed SnO_2 nanorod array, we perform a simulation of electric field on the SnO_2 nanorod array and a comparison to that of an SnO_2 film. The top parts of Figure 3-1a and b show cross-sectional electric field distributions of an SnO_2 film and the SnO_2 nanorod array, respectively, and the bottom parts of Figure 3-1a and b present the electric field strengths on the area arrowed in red. It is shown that, a higher electric field strength exists on the surface of bottom film (more than 0.49×10^6 V/m) rather than that of the film (0.4×10^6 V/m), meaning more cumulative charges (i.e., carrier). Considering the bottom film of the SnO_2 nanorod array is specifically designed to be a conductive channel, the adsorption on the bottom film surface therefore has a higher possibility

to induce carrier scattering. Additionally, the vertical nanorods shall introduce a larger surface adsorption for the SnO_2 nanorod array, as portrayed in Figure 3-1c and d. These results indicate that the gas-sensing of the SnO_2 nanorod array could be subject to a larger adsorption-induced degradation of carrier mobility than that of the SnO_2 film. Hence, it is highly possible that the SnO_2 nanorod array can exhibit a CMDGS response. As shown in Figure 3-1c and d, the CMDGS of the SnO_2 nanorod array with the large adsorption-induced degradation of carrier mobility would manifest as a more obvious decrease of current intensity (Figure 3-1d) than that of the SnO_2 film (Figure 3-1c).

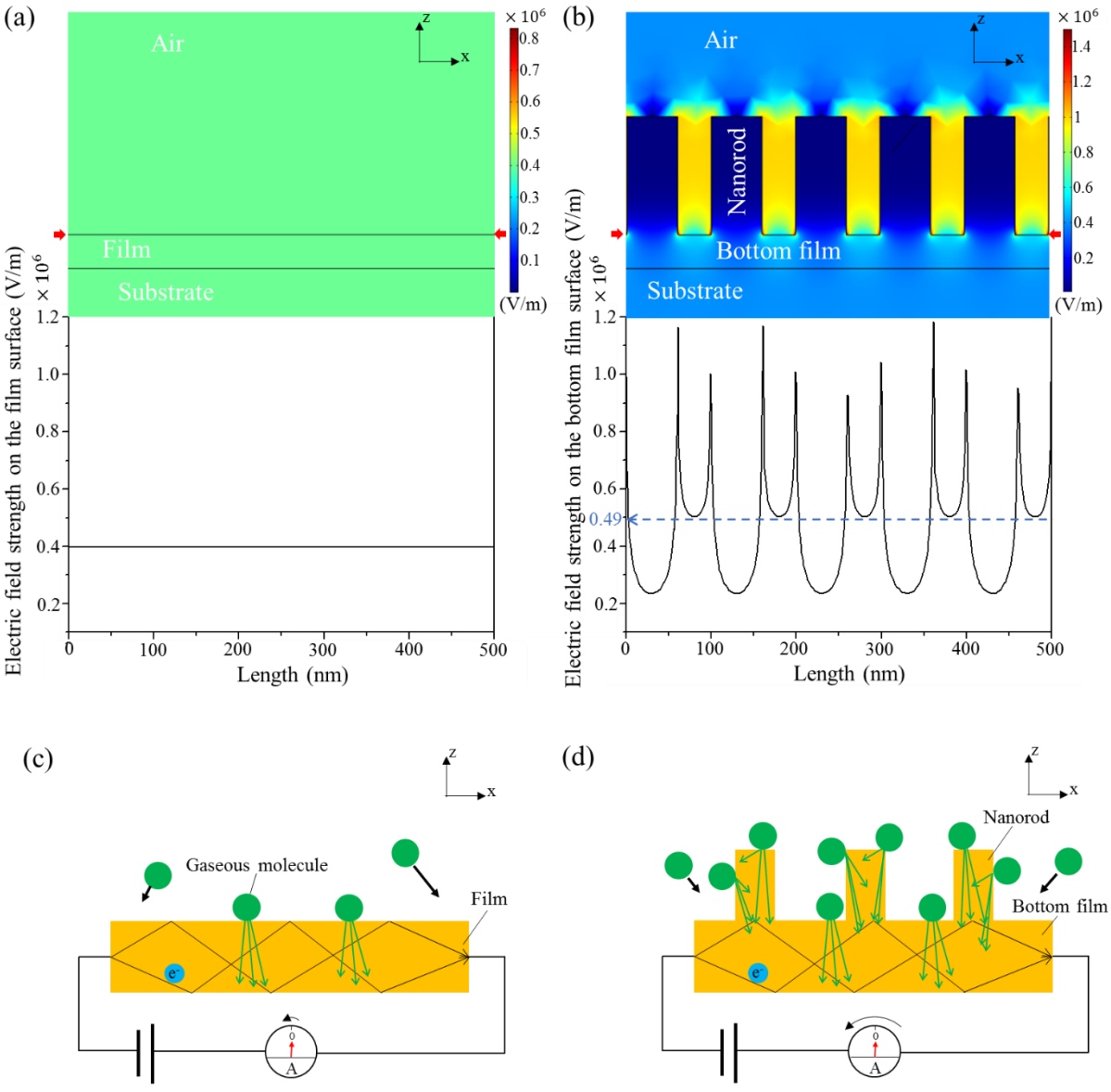

Figure 3-1. (a and b) Electric fields of the SnO_2 film (a) and the SnO_2 nanorod array (b) in air (the top parts of a and b), and their electric field strength on the area arrowed in red (the bottom parts of a and b). (c and d) Schematics of gas-sensing responses (i.e., current variation) of the SnO_2 film (c) and the SnO_2 nanorod array (d). Applied with a constant voltage, the SnO_2 nanorod array with a large adsorption-induced degradation of carrier mobility would exhibit a more obvious current decrease than that of the SnO_2 film, reflecting a distinct CMDGS response.

3.3.2. Fabrication of SnO_2 Nanorod Arrays on Device Substrates.

For the designed configuration of SnO_2 nanorod array gas sensors, the key point is that the bottom film bridging over two sensor electrodes serves as a conductive channel. Then a UTAM-based fabrication of SnO_2 nanorod arrays is used and schematically illustrated in Figure 3-2a. The UTAM was firstly immersed into precursor solution of SnO_2 (Figure 3-2a_1), then floated on the surface of solution (Figure 3-2a_2). The solution filled each channel of the UTAM due to the capillary effect.[31] Next this floated UTAM was picked up by a device substrate (Figure 3-2a_3). For the construction of the device substrate, interdigitated platinum/titanium (Pt/Ti) electrodes were seated on a substrate, a p-type Si substrate capped with a 300-nm-thick oxide layer. The UTAM covered the surface of the device substrate with the solution permeating its channels and bottom interval (Figure 3-2a_4). The existence of the bottom interval enabled the following growth of the bottom film on the device substrate, as depicted in the magnified image of Figure 3-2a_4. Then a heating measurement was performed on this sample (Figure 3-2a_5), resulting in the vertical SnO_2 nanorods in the UTAM channels and the bottom film in the bottom interval, of which SEM image is shown in Figure 3-2b. Finally, the SnO_2 nanorod array gas sensor was obtained after the removal of the UTAM in an aqueous H_3PO_4 solution.

Using the above-mentioned UTAM-based technique, this work prepares SnO_2 nanorod arrays with different lengths ranging from 340 to 40 nm. In a plane view of the SnO_2 nanorod array (Figure 3-2c), its SEM image depicts that nanorods are vertically and hexagonally arranged with a period of 100 nm. In cross-section views, different lengths of the nanorods can be observed, such as 340 nm (the upper part of Figure 3-2d), 140 nm (the upper part of Figure 3-2e), 110 nm (the lower part of Figure 3-2e), and 40 nm (the lower part of Figure 3-2d). Additionally, a 40-nm-thick bottom film can be clearly found in the 340 nm sample (the upper part of Figure 3-2d). Then this work uses these nanorod arrays as a gas sensor for following measurements.

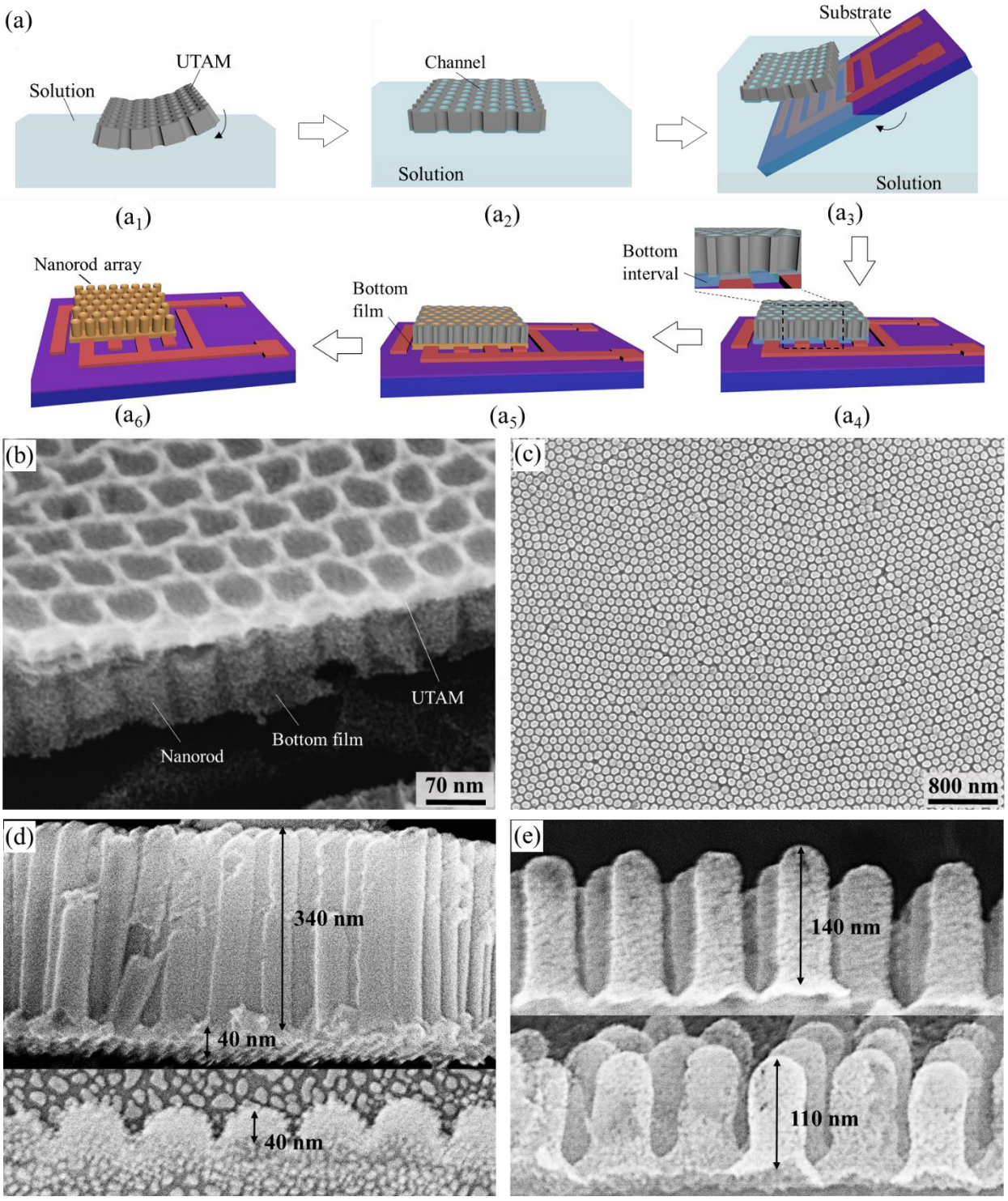

Figure 3-2. The SnO_2 nanorod array gas sensor fabrication. (a) The schematic representation of procedures for fabricating the SnO_2 nanorod array on a device substrate: (a_1) transferring a UTAM to the precursor solution; (a_2) the UTAM floated on the precursor solution; (a_3) picking up the UTAM with a device substrate; (a_4) the UTAM covering on the device substrate, the magnified image of the selected area showing the solution permeates the UTAM channels and

bottom interval; (a_5) drying and annealing both the UTAM and the device substrate; (a_6) the SnO_2 nanorod array obtained after the removal of the UTAM. (b) An SEM image showing the SnO_2 nanorod array without the removal of the UTAM. (c) A plane view of the SnO_2 nanorod array. (d and e) Cross-section views of the SnO_2 nanorod arrays with different nanorod lengths, involving 340 nm (the upper part of d), 40 nm (the lower part of d), 140 nm (the upper part of e), and 110 nm (the lower part of e). An obvious 40-nm-thick bottom film is observed from the 340-nm-length nanorod array (the upper part of d).

3.3.3. Composition Characterization of SnO_2 Nanorod Arrays.

Samples for transmission electron microscopy (i.e., TEM), X-ray diffraction (i.e., XRD) and X-ray photoelectron spectroscopy (i.e., XPS) characterizations are prepared under the same conditions as those of the preparation on the device substrate. Figure 3-3a shows a TEM image of SnO_2 nanorods scraped off from the device substrate. Small particles of SnO_2 are piled up into nanorods. The inset in Figure 3-3a displays the selected area electron diffraction (SAED) pattern of SnO_2 nanorods. The (110), (101), and (211) planes of the SnO_2 nanorods are discerned by diffraction rings, meaning the SnO_2 nanorod is of a polycrystalline structure. Figure 3-3b shows an XRD pattern of the SnO_2 nanorod array. Main diffraction peaks of SnO_2 (JCPDS FILE No. 70-4177) are observed, explaining that SnO_2 is formed by a solution-heated method in this work. Chemical compositions and oxidation states of existing elements in the SnO_2 nanorod array are determined by XPS. Figure 3-3c shows a survey scan XPS spectrum of the SnO_2 nanorod array and proves only two existed elements (Sn and O). The Sn 3d peak presents two distinct peaks at binding energies of 486.5 and 494.9 eV those correspond to the $3d_{3/2}$ and $3d_{5/2}$ states of Sn^{4+}.[29d] The O 1s spectrum (Figure 3-3d) can be resolved into two peaks corresponding to O^{2-} and O^- with binding energies of 532.4 and 531.6 eV. These ionized oxygen species on the SnO_2 surface indicate that, when SnO_2 nanorod arrays are put in air,

many atmospheric oxygen molecules can be adsorbed on the surface, and following reaction[1m] happens:

$$O_2 \xrightarrow{e^-} O_2^- \xrightarrow{e^-} 2O^-$$

where O_2 traps electrons from the SnO_2.

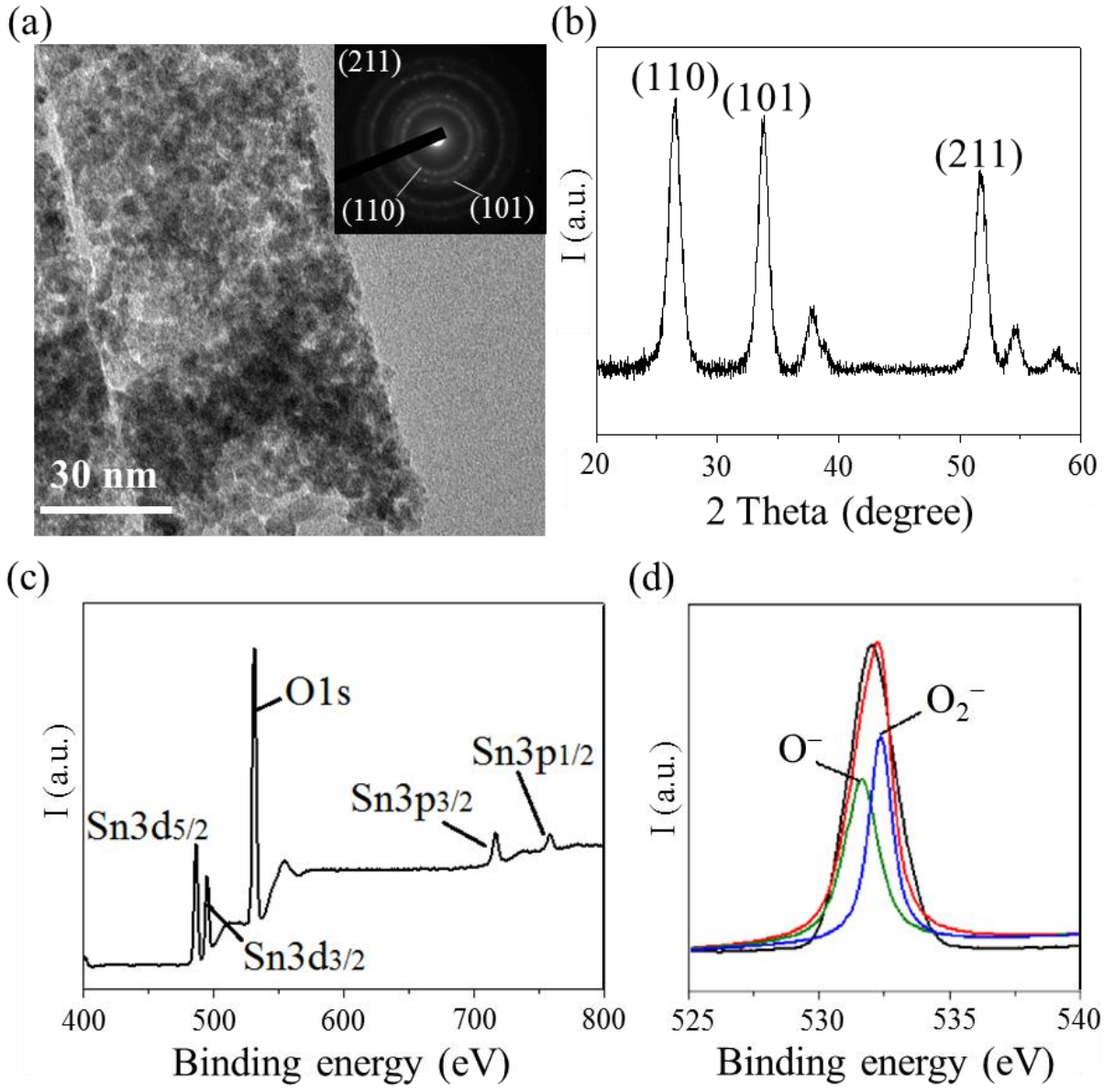

Figure 3-3. (a) The TEM pattern of the SnO_2 nanorod and its SAED pattern (the inset in a). (b-d) XRD (b) and XPS (c) patterns of the SnO_2 nanorod array and its O1s XPS spectrum (d).

3.3.4. Formation Mechanism of SnO_2 Nanorod Arrays.

The formation of SnO_2 nanorod arrays includes three steps, which are depicted exaggeratedly in Figure 3-4a and b. Firstly, a UTAM, with a 140 nm thickness and a 60 nm pore-diameter, is transferred to the surface of the precursor solution (the $SnCl_4$ aqueous solution). Given by the high energy surface of UTAM pore channels, the precursor solution spontaneously wets these pore channels (Figure 3-4a_1 and b_1). The wetting behavior on the surface can be described by the spreading parameter, which is defined as $s = \gamma_{sv} - \gamma_{sl} - \gamma_{lv}$ (γ_{sv}, γ_{sl}, and γ_{lv} are the solid-vapor, solid-liquid, and liquid-vapor interfacial tensions). Next 2-hour drying at 150 ^oC makes the $Sn(OH)_4$, firstly formed by the hydrolysis of $SnCl_4$, rapidly decomposed into SnO_2 after the volatilizing of solvent. Then the system of the precursor solution becomes viscous. Its viscosity (v) can be calculated by the Equation 3-1 as follow:

$$v = \exp(\exp(\frac{x \times VBN - 10.975}{14.534})) - 0.8 \quad (3\text{-}1)$$

where VBN is the viscosity blending index, and x is the mass fraction of the component of the precursor solution. For the systems of high concentration solutions (e.g., 0.1 and 0.06 M), a higher viscosity and a higher cohesive force will be obtained after volatilizing of solvent. Thus, a thick film liked sol-gel then can be formed on the inner wall of UTAM channels. If the thickness of the film is just equal to the diameter of the channels, the nanorod completely permeating the UTAM channel will be acquired finally (Figure 3-4a_2). Based on that, this work can gain nanorod arrays with different nanorod lengths by using corresponding thicknesses of UTAMs. In the case using a low concentration precursor solution (e.g., 0.01 M), as-induced film after the solution-heated process will be thin (Figure 3-4b_2) in the UTAM channel. These films are subject to severe defects (e.g., microtwins and stacking faults), and thus, these films are easy to be scraped off with the removal of the UTAM. Apart from these thin films, the short nanorods on the bottom of the UTAM is formed during the volatilizing of the solvent.

Therefore, this work can acquire the short nanorod arrays (e.g., 40 nm of nanorod length) by the low concentration of the precursor solution.

As a proof-of-concept, the 140-nm-thick UTAMs are filled with the high and the low concentration precursor solution and then processed heating measurements. In Figure 3-4c and e, SEM images shows plane views of the UTAMs where thermal-mismatch defects do not exist on the surface. In tilted views of SEM images (Figure 3-4d and f), high concentration of the precursor solution (e.g., 0.1 M) makes SnO_2 permeated the UTAM channels, resulting in the nanorods with length consisted with the thickness of the UTAM (Figure 3-4d). In contrast, the low concentration of the precursor solution makes only bottom parts of the channels filled with the SnO_2 (Figure 3-4f). This part of the SnO_2 will be remained after the removal of the UTAM, leaving behind short nanorods on the bottom film. The subsequent high-temperature treatment at 450℃ produces a firm adherence between the SnO_2 nanorod array and the substrate (Figure 3-4a_3 and b_3).

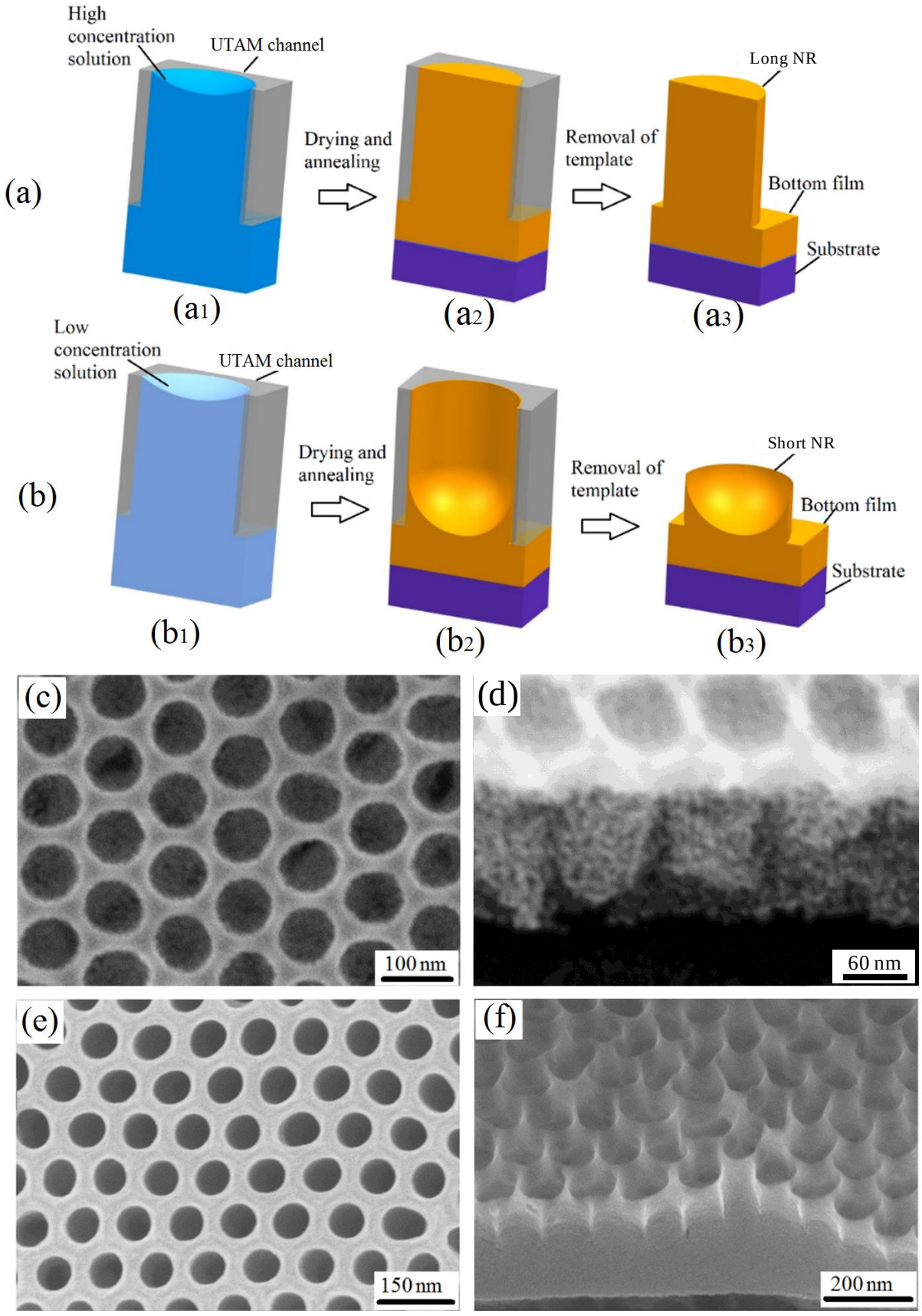

Figure 3-4. (a and b) Schematics represent formation processes of a long (a) and a short (b) SnO_2 nanorod array based on a high (0.1M) and a low concentration (0.01M) of the precursor

solution. (c-f) SEM images show SnO_2 nanorod arrays without the removal of UTAMs (140 nm thickness) from a plane and a tilted view. The SnO_2 nanorod arrays are prepared from a 0.1 M (c and d) and a 0.01 M (e and f) of precursor solutions, respectively. Herein, the NR is the short term of nanorod.

3.3.5. SnO_2 Nanorod Arrays Prepared by Modulating the Precursor Solution Concentration.

With a 110-nm-thick UTAM, this work modulates the concentration of the precursor solution, ranging from 0.01 to 0.1 M, to prepare SnO_2 nanorod arrays. Figure 3-5a and b show SEM images of the short nanorod array prepared from a 0.01 M precursor solution, from a plane and a tilted view. A few of thin roll films exist on the surface, as depicted in Figure 3-5a. These residues prove the occurrence of the thin film around the UTAM channel during the solution-heated process. In contrast, the long nanorod arrays can be acquired when the concentration of the precursor solution is generally up to 0.06 and 0.1 M. The generated nanorods (Figure 3-5c-f) are of a 60 nm diameter and a 110 nm length, which are consistent with the parameters of the UTAM channel, i.e., pore diameter and thickness. Compared with the nanorod array prepared from 0.1 M precursor solution (Figure 3-5e and f), the one prepared from 0.6 M precursor solution shows many defects (Figure 3-5c and d). These defects indicate that the SnO_2 growth in the UTAM channel is easy to agglomerate somewhere and cannot reach designated positions during the solution-heated process. This non-uniform growth of nanorods thus generates defects.

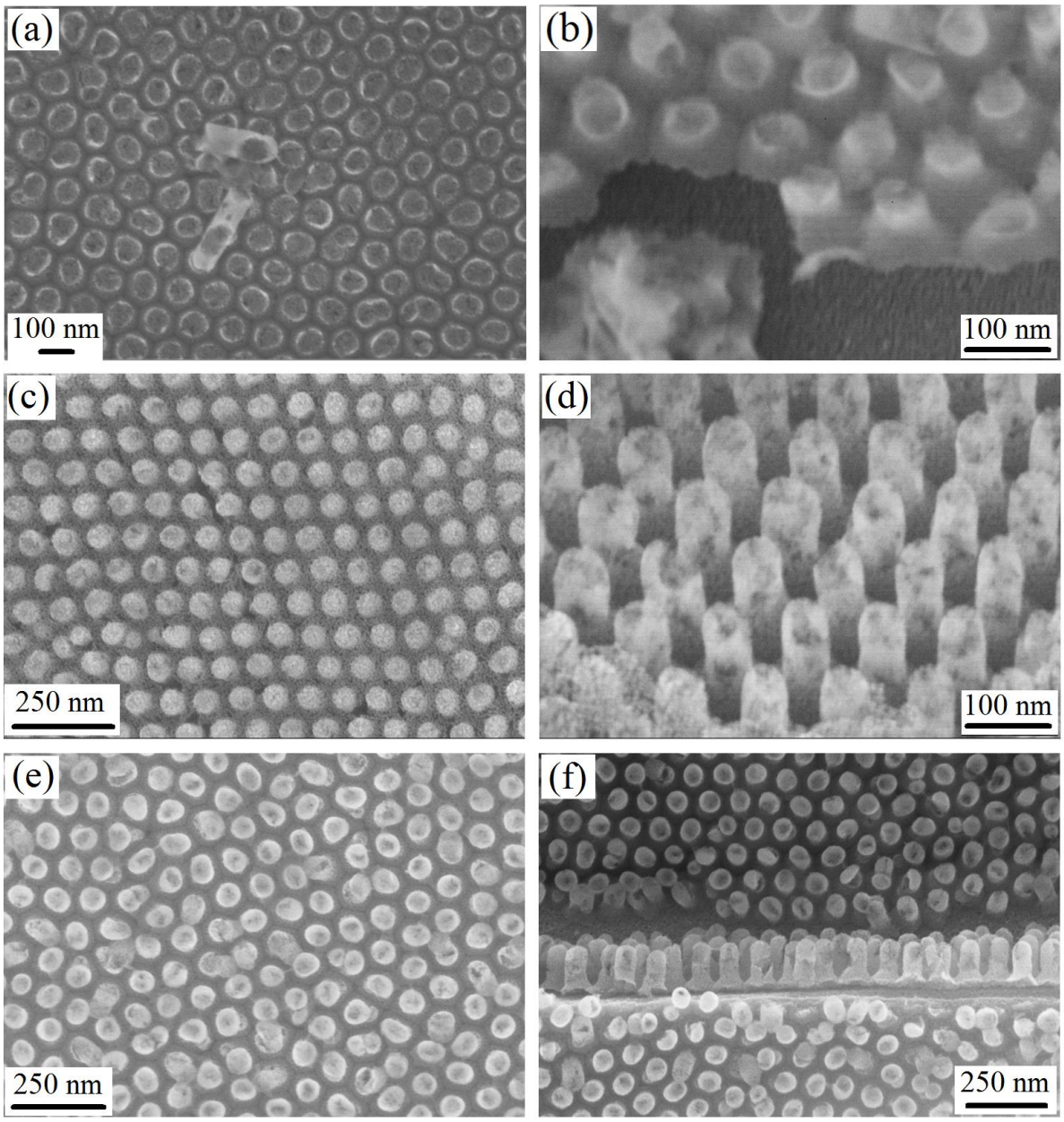

Figure 3-5. SnO_2 nanorod arrays prepared from different concentrations of the precursor solutions. (a-f) SEM images showing the SnO_2 nanorod arrays prepared by 0.01 M (a and b), 0.06 M (c and d), and 0.1M (e and f) of $SnCl_4$ aqueous solutions, from a plane and a tilted view.

3.3.6. Agglomerations of SnO_2 Nanorods Unconnected with the Bottom Film.

Agglomerations of SnO_2 nanorods unconnected with the bottom film are schematically illustrated by Figure 3-6a. Figure 3-6b shows the SEM image of agglomerated SnO_2 nanorods from a tilted view (the inset in Figure 3-6b). The nanorods cannot be orderly arranged and favor agglomerating into big particles.

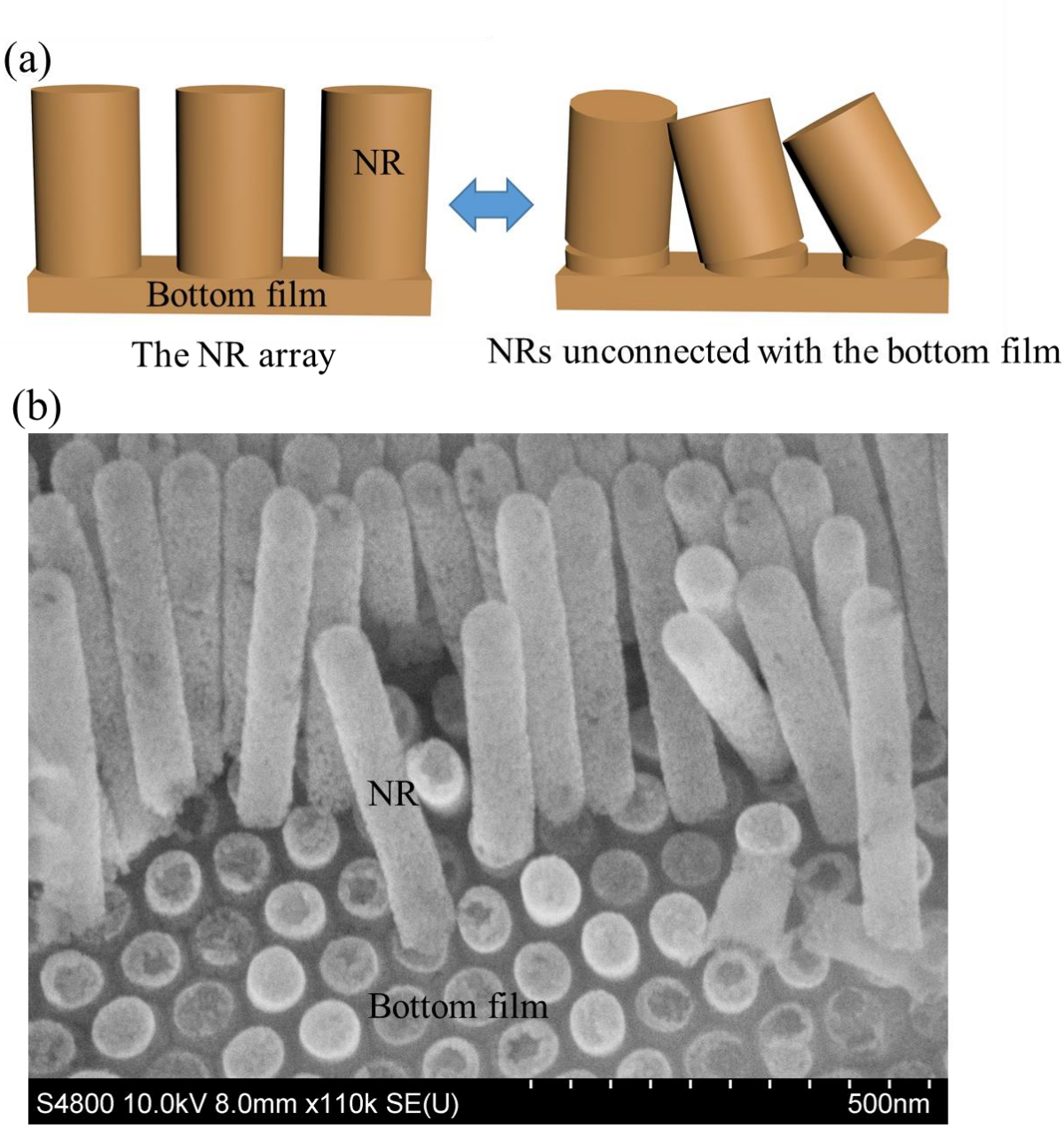

Figure 3-6. (a) The schematic illustration of agglomeration of long SnO_2 nanorods unconnected with a bottom film. (b) SEM image showing SnO_2 nanorods unconnected with a bottom film from a tilted view. Herein, the NR is the short term of nanorod.

3.3.7. Output Characterizations of SnO_2 Nanorod Arrays.

Herein, a 340-nm-length and a 40-nm-length SnO_2 nanorod array are fabricated into field effect transistors for output characterizations. Figure 3-7a and b show I_{ds}-V_{ds} curves of both nanorod arrays obtained by V_g varying from 2 to 0.8 V (step = -0.2 V). Among them, I_{ds} and V_{ds} are respectively a drain-to-source current and a voltage, and V_g is a gate voltage. An n-type behave

can be seen by a fact that the increasing V_g led to the increasing of I_{ds}, showing for both two SnO_2 nanorod arrays. This n-type behave means that electron is charge carrier in samples, of which conductivity is positively associated with electron density. Meanwhile, a schottky contact, manifested as a nonlinear I_{ds}-V_{ds} relationship, can be also observed.

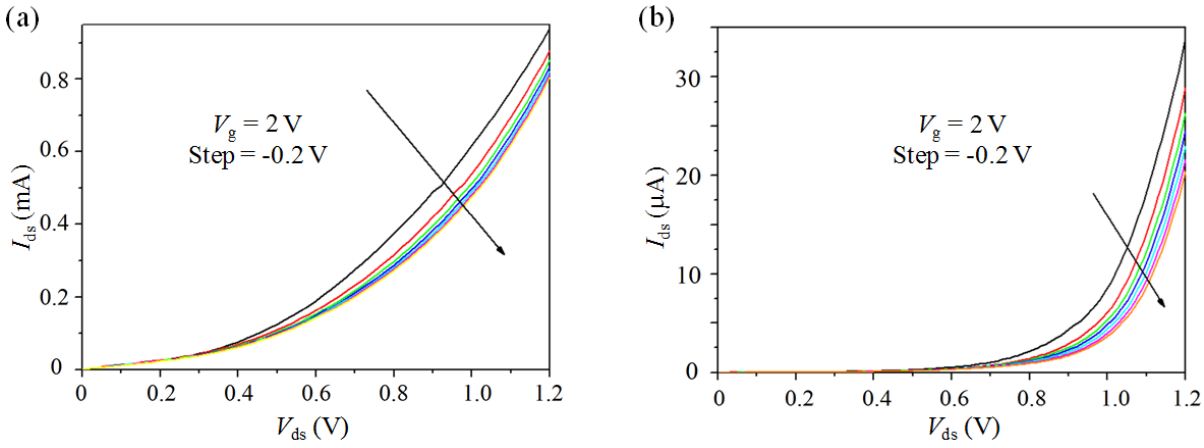

Figure 3-7. (a and b) I_{ds}-V_{ds} output curves of the 340-nm-length (a) and the 40-nm-length SnO_2 nanorod array (b). Both SnO_2 nanorod arrays behave as an n-type conductance channel.

3.3.8. The Gas-Sensing of SnO_2 Nanorod Arrays.

In our gas-sensing measurements, applied with a constant voltage of 4 V, changes of I_t/I_0 value from gas sensors on exposure to detected gases are monitored and recorded as sensing signals.[29b, 32] I_0 and I_t are output currents of a sensor in air and detected atmospheres, respectively. Detected gases involve 25 ppm of ethanol, isopropanol, and acetone gas. Figure 3-8a-d show room temperature gas-sensing responses of SnO_2 nanorod arrays consisting of different nanorod lengths (340, 140, 110, and 40 nm). It can be seen that the positive gas-sensing response ($I_t/I_0 > 1$) turns negative ($I_t/I_0 < 1$) when the nanorod length decreases from 340 to 40 nm. As the SnO_2 nanorod array is applied with a constant voltage, a positive and a negative gas-sensing response indicate an increase and a decrease of sample conductivity respectively after the introduction of detected gases. Figure 3-8a describes the conductivity of the 340-nm-length SnO_2 nanorod array increases after the introduction of detected gases. All the detected gases (ethanol, isopropanol, and acetone gases) are reducing gases those can react

with the oxygen ions (O^{2-} and O^{-}) on SnO_2 surface, resulting in releasing of trapped electrons.[33] As SnO_2 is a n-type semiconductor, the releasing of trapped electrons from oxygen species to SnO_2 effectively increases the carrier density in the SnO_2 nanorod array, therefore increasing the SnO_2 conductivity. It suggests that the positive gas-sensing response of 340-nm-length SnO_2 nanorod array is a typical CDDGS response. In the detection of 25 ppm acetone gas, this sample exhibits a gas-sensing response with the I_t/I_0 of 1.13. However, this response to the acetone gas becomes weak ($I_t/I_0 \sim 0$) when the nanorod length decreases to 140 nm (Figure 3-8b), and then turns to an unusual negative ($I_t/I_0 = 0.93$) response as the length of nanorod continuously decreases to 110 nm (Figure 3-8c). This kind of negative gas-sensing response indicates that, for the 110-nm-length SnO_2 nanorod sample, the introduction of the acetone gas doesn't increase the conductivity but rather decreases it. This conductivity decreasing could be only caused by the decrease in carrier density and/or the degradation of carrier mobility. Considering the aforementioned fact that reducing gases (e.g., acetone gas) always lead to the carrier density increase in the SnO_2 nanorod arrays, the conductivity decreasing of the 110-nm-length SnO_2 nanorod array shall be attributed to a large degradation of carrier mobility. When the nanorod length further decreases to such as 40 nm (Figure 3-8d), this negative gas-sensing response caused by the degradation of carrier mobility becomes more distinct, revealing that a carrier mobility dominated gas-sensing (i.e., CMDGS) mode dominates the gas-sensing when the nanorod length is 40 nm. Importantly, the CMDGS mode shows an enhanced gas-sensing sensitivity. Take the detection of 25 ppm acetone gas as an example, the CMDGS-mode sensor (i.e., the 40-nm-length sample) has a current decrease of about 58% ($1 - I_t/I_0 = 0.58$) while the CDDGS-mode sensor (i.e., the 340-nm-length sample) shows a current increase of about 13% ($I_t/I_0 - 1 = 0.13$), indicating that the sensitivity of CMDGS-mode is more than 4-times higher than that of CDDGS.

A similar gas sensing behavior changing from CDDGS to CMDGS exists in detections of the other two reducing gases (ethanol and isopropanol). However, a changing point from CDDGS to CMDGS referring to nanorod length is not in the same range for different gases (Figure 3-8a-d): the changing point of acetone, isopropanol, and ethanol shall be in the ranges of 340-140 nm, 140-110 nm, and 110-40 nm, respectively. To further investigate the CDDGS-CMDGS changing related to the nanorod length, an 80-nm-length and a 20-nm-length SnO_2 nanorod array are prepared, and 25 ppm ethanol gas is selected as a target gas. Both the 80-nm-length and the 20-nm-length samples exhibit a negative gas-sensing response, showing a typical CMDGS mode. Figure 3-8e portrays a correlation of the gas-sensing mode (characterized by $I_t/I_0 > 1$ for CDDGS, or $I_t/I_0 < 1$ for CMDGS) with the nanorod length. The SnO_2 nanorods exhibit the CMDGS when the nanorod length decreases to 80 nm, indicating that the CDDGS-CMDGS changing point of nanorod length for ethanol is located within the range of 110-80 nm.

As indicated in Figure 3-8e, the CMDGS is more dominated with the deceasing of nanorod length from 80 to 40 nm. However, with the further decreasing of length from 40 to 20 nm, the CMDGS dominating becomes weaker. To understand this mechanism, this work estimates the scattering length of adsorbed ethanol gaseous molecules on SnO_2. Similar to the close relation of Debye length to gas sensing of adsorbed oxygen molecules on SnO_2,[21b] the scattering length of adsorbed ethanol molecules shall play an important role for gas-sensing. For a certain gaseous molecule adsorbed on the surface of SnO_2 nanorod, when its scattering length is large enough to reach the bottom film, it shall influence the carrier mobility in the film and hence cause the CMDGS. In the case of ethanol, the CDDGS mode exists for 110-nm-length sample and turns to the CMDGS when the nanorod length decreases to 80 nm, suggesting that the scattering length of ethanol molecules could be in the range of 80-110 nm. For the 40-nm-length nanorods on a 40-nm-thickness bottom film, all the adsorbed molecules with scattering

lengths (80-110 nm) shall be capable of influencing the carriers in the bottom film, and hence contributing to the degradation of carrier mobility and generating a distinct CMDGS. However, the further shortening of nanorods would also decrease the overall number of the adsorbed molecules which leads to a degraded capability to influence the carrier mobility, like the case of the 20-nm-length sample with a reverse trend of the CMDGS. Therefore, an optimum length of nanorods is achievable for obtaining the best CMDGS response, such as 40 nm of nanorod length as the best value for ethanol.

For the sake of further practical applications, detection limitation and long-term stability of CMDGS need to be studied. The 40-nm-length SnO_2 nanorod array, a typical CMDGS-mode gas sensor, is served as a model gas sensor. In the study on the detection limit at room temperature, different concentrations of ethanol gases (18, 12, 6, and 3 ppm) are introduced. Then the 40-nm-length SnO_2 nanorod array exhibits corresponding I_t/I_0 of 0.849, 0.921, 0.974, and 0.988 (Figure 3-8f). This concentration-dependent sensitivity indicates that CMDGS of 40-nm-length nanorod array has a low detection limit of 3 ppm ethanol gas at room temperature. This ethanol-detection limit of the SnO_2 nanorod array is competitive as compared with those of other SnO_2 gas sensors. Additionally, the 40-nm-length SnO_2 nanorod array exhibits a high long-term stability (the inset in Figure 3-8f). After the sensor experiences all the tests shown in Figure 3-8f and is placed in ordinary surrounding for more than 6 months without any protections, it still exhibits nearly the same sensitivity as that when it is first used in detecting different concentrations of ethanol gases.

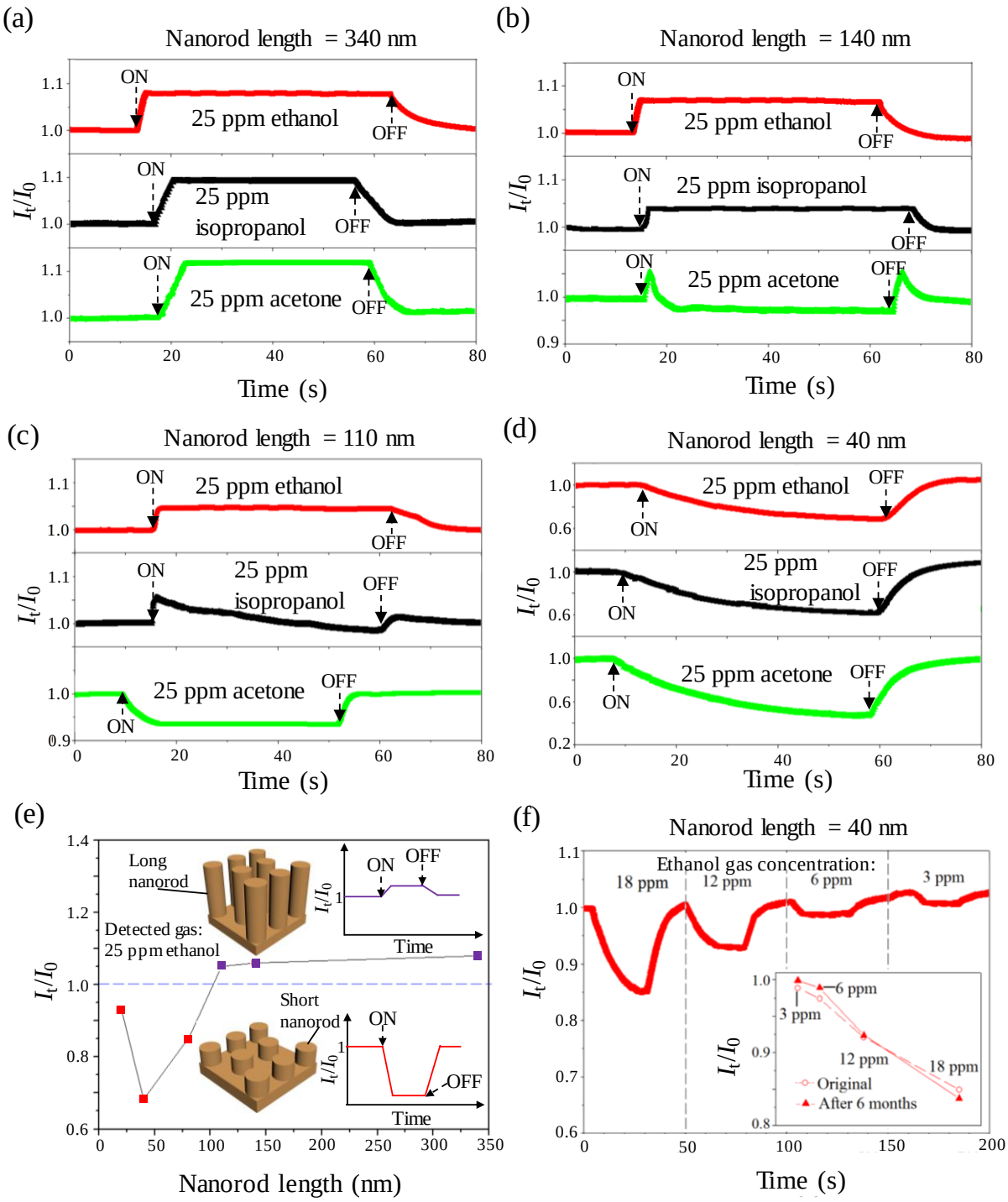

Figure 3-8. Gas-sensing characteristics of SnO_2 nanorod array gas sensors. (a-d) Gas-sensing responses to 25 ppm of ethanol, isopropanol, and acetone gases at room temperature versus time for the SnO_2 nanorod arrays with different nanorod lengths, such as 340 nm (a), 140 nm (b), 110 nm (c), and 40 nm (d). A voltage of 4 V is applied to a device. As the nanorod length decreases from 340 to 40 nm, all sensing responses vary from the positive ($I_t/I_0 > 1$) to the

negative ($I_t/I_0 < 1$). (e) The I_t/I_0 of the SnO_2 nanorod array gas sensor versus the nanorod length (340, 140, 110, 80, 40, and 20 nm) in the detection of 25 ppm ethanol gas, describing that the CMDGS (i.e., $I_t/I_0 < 1$) substitutes the CDDGS (i.e., $I_t/I_0 > 1$) as the nanorod length is shorter than or equal to 80 nm. (f) Gas-sensing responses to 18, 12, 6, and 3 ppm of ethanol gases at room temperature versus time for the 40-nm-length SnO_2 nanorod array. The inset compares the original I_t/I_0 of the 40 nm one with that after 6 months.

3.3.9. The Gas-Sensing of the 40-nm-Length Nanorod Arrays with Different Nanorod Diameters.

To confirm the negative gas-sensing response of the 40-nm-length nanorod array, this work prepares the samples with different nanorod diameters, such as 40, 60, and 70 nm, and uses them to detect 25 ppm ethanol gas. Figure 3-9a-b show plane views of these array, where the same alignment period of 100 nm is observed for the samples with different diameters, involving 40 nm (Figure 3-9a), 60 nm (Figure 3-9b), and 70 nm (Figure 3-9c). In the detection of 25 ppm ethanol gas, these samples exhibit the negative response that aroused by their conductivity decreases. It indicates that, similar to the gas-sensing behaviour of the 60-nm-diameter sample, the other two arrays (i.e., the 40-nm-diameter and the 70-nm-diameter sample) are also subject to a large degradation of carrier mobility to present the negative responses. In these negative responses, these samples show different sensitivities. The samples with 40, 60, and 70 nm diameter are of sensitivities of 0.625, 0.675, 0.725 (Figure 3-9d).

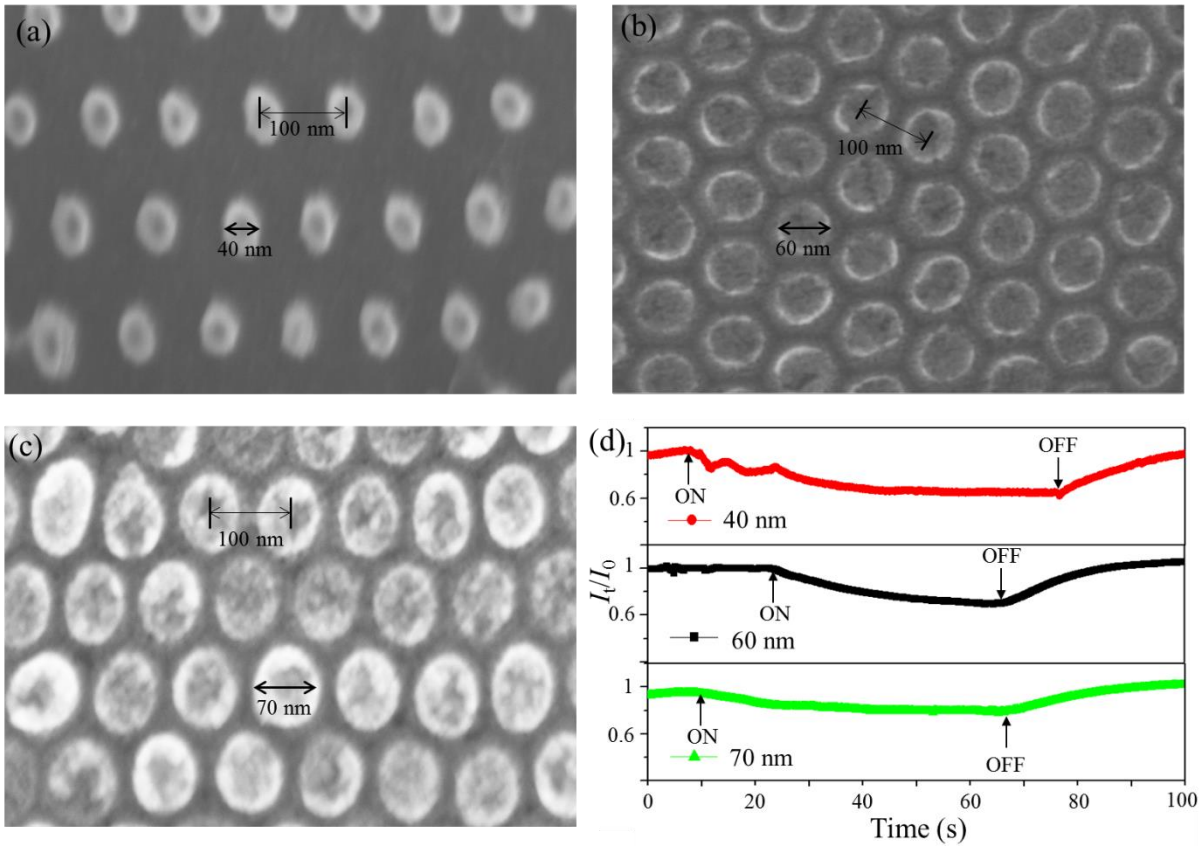

Figure 3-9. (a-c) SEM images of the 40-nm-length nanorod arrays with different diameters, such as 40 nm (a), 60 nm (b), and 70 nm (c). From their plane views, the same nanorod alignment of 100 nm is observed for all the samples. (d) The gas-sensing properties of the samples with 40, 60, and 70 nm nanorod diameters in the detection of 25 ppm ethanol gas.

3.3.10. The Adsorption-Induced Degradation of Carrier Mobility in SnO_2 Nanorod Arrays.

To demonstrate a large adsorption-induced degradation of carrier mobility in the CMDGS of the 40-nm-length SnO_2 nanorod array, the simulation of electric field is firstly performed on two representative SnO_2 nanorod arrays (i.e., the 340-nm-length and the 40-nm-length SnO_2 nanorod array). Figure 3-10a and b display their electric field strengths on two desirable areas: (i) the bottom film surface and (ii) the interface between nanorods and the bottom film. It is shown that, on the interface between nanorods and the bottom film, the lowest electric field strength of the 40 nm sample (0.27×10^6 V/m) is larger than that of the 340 nm (0.21×10^6 V/m).

The stronger electric field strength suggests that the adsorption on the 40-nm-length nanorods might produce a more obvious carrier scattering on the bottom film than that of 340-nm-length nanorods, resulting in a larger carrier mobility degradation in the 40-nm-length nanorod array. Field-effect transistor characterizations, a well-accepted way to the investigation of carrier mobility,[1a] is used to reveal the carrier mobility variation of the SnO_2 nanorod arrays after the introductions of reducing gases. The 40-nm-length and the 340-nm-length SnO_2 nanorod array are fabricated into field-effect transistors. Two 50-nm-thick Pt electrodes are respectively served as a source and a drain metal contact. The underlying SiO_2 and the p-doped Si substrate are used as a gate dielectric and a gate contact, respectively. Figure 3-10c and d depict I_{ds}-V_{ds} characteristics of the 340-nm-length (Figure 3-10c) and the 40-nm-length SnO_2 nanorod array (Figure 3-10d) measured in reducing gas atmospheres (25 ppm of ethanol, isopropanol and acetone) and air at room temperature. Among them, I_{ds} and V_{ds} are drain-to-source current and voltage, respectively. V_g is the gate voltage and equals to 0 V. It is shown that, as the V_{ds} sweeps from 0 to 5 V, the I_{ds} intensity in air is larger than those exposed to reducing gases for the 40-nm-length SnO_2 nanorod array, while that of the 340-nm-length is reverse. This comparison reveals that the conductivity of the 40-nm-length nanorod array decreases after the introduction of reducing gases.[34]

In order to measure whether the electron mobility (i.e., carrier-mobility) of the 40-nm-length SnO_2 nanorod array decreased in the adsorption-induced conductivity reduction or not, I_{ds}-V_g transfer curves of the 40-nm-length SnO_2 nanorod array in different detected atmospheres are measured at V_{ds} = 4 V as compared to that of the 340 nm (Figure 3-10e and f). It is found that, an I_{ds}-V_g hysteresis in reducing gases is large for the 40-nm-length nanorod array, indicating its electron mobility should have a distinct variation when the detected atmosphere turns from air to reducing gases.[35] Herein the variation of the electron mobility is defined as $(\mu_r - \mu_{air})/\mu_{air}$.

μ_r and μ_{air} are the electron mobilities in the reducing gas and air, respectively. The electron mobility (μ) can be estimated using the following expression, Equation 3-2:[1a]

$$\mu = (\frac{dI_{ds}}{dV_g}) \times (\frac{L^2}{C_{ox}}) \times (\frac{1}{V_{ds}}) \quad (3\text{-}2)$$

where dI_{ds}/dV_g is the transconductance extracted from the linear region of the I_{ds}-V_g curve, L is the distance between two neighboring electrodes. As the nanorod array has a regular geometry and a much larger size (1.2×10^4 μm^2) than the dielectric layer thickness (300 nm), the capacitance (C_{ox}) of the nanorod array with respect to the p++ gate (i.e., the Si substrate) can be approximated as a capacitance between two parallel plates. Combined with the Equation 3-2, the variation of the electron mobility can be calculated by the Equation 3-3 as follow:

$$\frac{\mu_r - \mu_{air}}{\mu_{air}} = \frac{\frac{dI_{ds-r}}{dV_{g-r}} - \frac{dI_{ds-a}}{dV_{g-a}}}{\frac{dI_{ds-a}}{dV_{g-a}}} \quad (3\text{-}3)$$

where $dI_{ds\text{-}r}/dV_{g\text{-}r}$ and $dI_{ds\text{-}a}/dV_{g\text{-}a}$ are the transconductances of the I_{ds}-V_g curves in reducing gas and air, respectively. Then the electron mobility of the 40-nm-length nanorod array is estimated to decrease 92.7, 98.9, and 99.9% after introductions of 25 ppm of ethanol, isopropanol, and acetone gases. These more than 90% degradations of the carrier mobility prove a large adsorption-induced degradation of carrier mobility in the CMDGS of the 40-nm-length SnO_2 nanorod array.

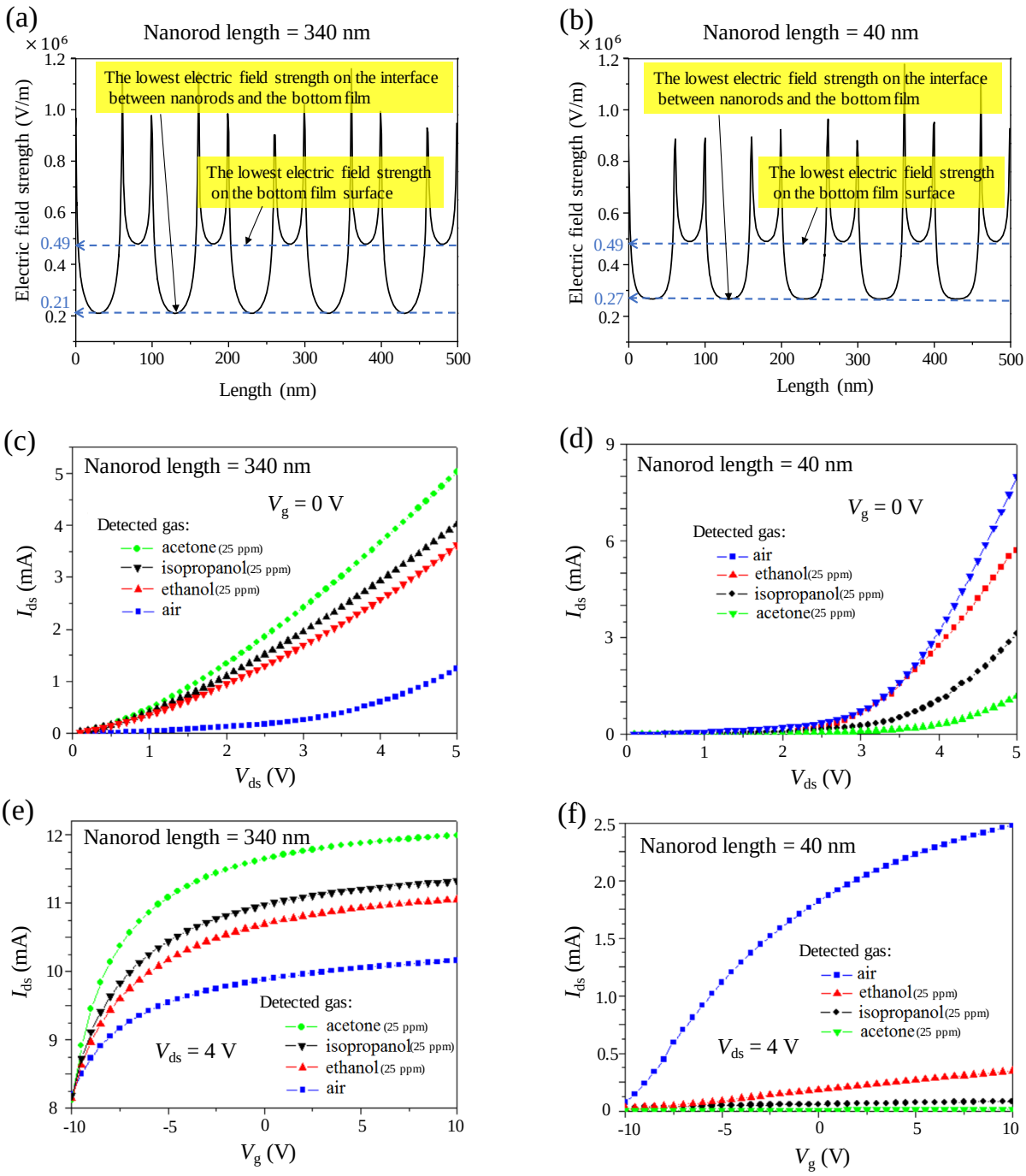

Figure 3-10. Electric characteristics of SnO_2 nanorod arrays. (a and b) Electric field strengths on two desirable areas of the 340-nm-length (a) and the 40-nm-length nanorod array (b) in air: (i) the bottom film surface and (ii) the interface between nanorods and the bottom film. (c and d) I_{ds}-V_{ds} curves of the 340-nm-length (c) and the 40-nm-length SnO_2 nanorod array (d) obtained at different detected atmospheres, at room temperature, and V_g = 0 V. (e and f) I_{ds}-V_g

transfer curves of the 340-nm-length (e) and the 40-nm-length SnO_2 nanorod array (f) at different detected atmospheres, at room temperature, and V_{ds} = 4 V.

3.4. Conclusions.

In summary, this work indicates a different gas-sensing mode of CMDGS from the conventional CDDGS mode for inorganic semiconductor gas sensors. To demonstrate this CMDGS, this work firstly designs and fabricates a regular array of SnO_2 nanorods on a bottom film, then uses it for room temperature gas-sensing. By modulating the length of arrayed nanorods, the gas-sensing behavior changes from CDDGS to a complete CMDGS mode. Moreover, the realized CMDGS-mode gas sensor is of a more than 4-times higher sensitivity than that of the CDDGS-mode. It is anticipated that the proposed CMDGS mode shall be applicable to other gas sensing systems of different inorganic semiconductors, providing a concept for designing gas sensors.

4. Colloidal-Monolayer-Assisted Fabrication of an SnO_2 Film on Triangle Arrays for the Sensitive Gas-Sensing

(This chapter is based on my published work: Xu, S.P.; Xu, Y.; Zhao, H.P.; Xu, R.; Lei, Y.* Sensitive Gas-Sensing by Creating Adsorption Active Sites: Coating an SnO_2 layer on Triangle Arrays. *ACS Applied Materials &Interfaces* **2018**, *10*, 29092-29099.)

4.1. Design Concept of the SnO_2 Film Gas Sensor.

Sensing gaseous molecules is important to environmental monitoring, control of chemical process, and agriculture applications.[1a, 1b, 1d, 1e, 1g, 36] Among them, sensitive gas-sensing is always a constant pursuit. To this end, nanostructuring a gas sensor is a widely-used strategy, and the generated nanostructure gas sensor usually exhibits a desirable gas-sensing sensitivity.[1d, 1e, 36a, 36b] However, the conventional nanostructuring way is of a low efficiency for the eventual applications of gas sensors, in which nanostructuring and bonding the whole sensing block into a device substrate need complex manipulations. It is worthy to explore an efficient approach to prepare a gas sensor with high sensitivity.

Gas-sensing sensitivity of nanostructure gas sensors is closely related to their surface adsorption. Tracing the origin of the surface adsorption and exploiting it in gas-sensing provide a high possibility to enhance the sensitivity of gas sensors. Thermodynamically, the surface adsorption is a spontaneous process accompanying with decreasing of Gibbs free energy ($\Delta G < 0$). In this decreasing of Gibbs free energy, there is a correlation between the change in Gibbs free energy, entropy (S), and enthalpy (H):

$$\Delta G = \Delta H - T\Delta S \quad (4\text{-}1)$$

Adsorption confines a gaseous molecule to the substrate, which induces an unfavourable entropy change, $\Delta S < 0$. Thus, ΔH shall be negative (exothermic) for the gaseous molecules turned from the gas phase to the adsorbed phase ($H_a - H_g < 0$). A low enthalpy of the adsorbed phase (i.e., H_a) exists when a gaseous molecule is adsorbed on the substrate area with a lot of

stepped and kinked crystal surfaces. Therefore, the substrate area rich of the stepped and kinked crystal surfaces should tend to adsorb more gaseous molecules than that of the other area. For example, in a gas-sensing work using 3D pore arrays,[37] the structure of the 3D pore is divided into two adsorption areas: (i) pore wall and (ii) the convex along the surface pore. The pore convex is a typical area with lots of stepped and kinked crystal surfaces.[38] As a result, this pore convex absorbs more gaseous molecules than that of the pore wall. Inspired by the high efficiency of the convex related to surface adsorption, it is worthy to create a gas sensor with convex-rich morphology for realizing the sensitive gas-sensing.

Triangle is of a convex-rich morphology and already developed for sensing gaseous molecules.[39] By colloidal-monolayer-based method, triangles can be easily aligned into a regular array and further adjusted to achieve an optimized performance in sensing applications.[13, 39a, 40] This adjustment includes changing the sensing volume by controlling the triangle nanoparticle size, period, and shape, for which we just need to vary the deposition parameters during the sample preparation: (i) the monolayer-nanosphere size and (ii) deposition time.[13, 40b] Considering such easy accessibility of the triangle array morphology related to the sensitive sensing, we herein deposit an SnO_2 film on the triangle array for an ensemble of triangular convex adsorption active sites (i.e., TCAASs), by which a surface adsorption enhancement of the SnO_2 film can be realized for sensitive gas-sensing.

As a-proof-of-concept, colloidal monolayers consisting of different diameters of nanospheres (500, 750, 1000, and 2000 nm) are used as a template for fabricating a series of triangle arrays. Then an SnO_2 film is coated on these arrays and characterized by the different TCAAS sizes. It is found that, the sample with the largest TCAAS exhibits the highest sensitivity, which is characterized by a low detection limit of around 6 ppm ethanol gas at room temperature. Comparably, without adsorption active sites, a flat film of SnO_2 has no gas-sensing responses even to a high concentration of 25 ppm ethanol gas. To reveal this adsorption-active-site-origin

of sensitivity, we use Kelvin force microscopy (KFM) to investigate adsorption quantity on the TCAAS by its surface potential variation after introducing ethanol gas. Importantly, the KFM results distinctly present an adsorption enhancement on the TCAAS. These results confirm that the creation of the adsorption active site can efficiently enhance the surface adsorption of gas sensors for their sensitive gas-sensing.

4.2. Experiment and Instruments.

4.2.1. Fabrication of a Colloidal Monolayer.

Monodispersed polystyrene nanosphere suspensions (2.5 wt% in water, surfactant free) were bought from Alfa Aesar Company. An ordinary glass substrate (1.5 × 1.5 cm^2) was ultrasonically cleaned in acetone and then in ethanol for 1 hour. Subsequently, the substrate was mounted on a custom-built spin coater. An amount of 10 μL of the nanosphere suspension was dropped onto the substrate. A large-area colloidal monolayer (> 1 cm^2) was fabricated by a spin-coating method at a speed of 800 rotations per minute.

4.2.2. Fabrication of SnO_2 Films on Ti Triangle Arrays.

A colloidal monolayer was used as a deposition mask, through which a 10-nm-thick layer of Ti was deposited by physical vapour deposition. The deposition rate was maintained at 0.02 Å/s, and the vacuum level was lower than 10E-6 Pa. After the deposition process, the colloidal monolayer was immersed into CH_2Cl_2 within 10 minutes for its removing. The generated Ti triangle array was then coated with a 6.85-nm-thick film of SnO_2 by using a PicoSun SUNALE R-150 atomic layer deposition system (PicoSun, Finland), according to the following procedure. In this process, the reaction chamber was firstly heated to 250 °C, and $SnCl_4$ and H_2O were respectively chosen as the precursors of Sn and O. $SnCl_4$ was pulsed for 0.1 s and purged for 10 s, followed by a 0.1 s pulse and a 10 s purge of H_2O. This procedure was repeated 500 times, according to the growth rate of ~0.14 Å per cycle to reach a thickness of 6.85 nm.

In this mean, colloidal monolayers with different diameters of nanospheres were used as a template, and SnO_2 films on different triangle arrays can be obtained.

4.2.3. Characterizations of KFM.

The sample was placed on the sample stage and was grounded. A Pt/Si tip with 75 Hz of resonance was used. The scan rate was set at 1 Hz, and the scan area is 3.5 μm^2. The measurement system was conducted in a sealed box, by which different detected atmospheres can be introduced and removed. The detected atmosphere was changed prior to the KFM acquaintance: (i) in air and (ii) with 25 ppm ethanol gas.

4.2.4. Gas-Sensing Tests.

With electrical feedthroughs, gas-sensing tests were carried out in an air-tight chamber. Applying with a voltage of 4 V, the Keithley semiconducting testing system monitored and recorded the sample' variation of the output current towards the changes in the gas environment using. The main target gas is the reducing gas, 25 ppm ethanol. The gas-sensing measurement includes the following steps: (1) the output current intensity from the sensor in air was recorded as the basic value; (2) with introduction of a calculated volume of detected gas into the chamber, the variation of output current was simultaneously recorded as the response signal; (3) as the signal stabilized and manifested as a platform, the chamber was opened to remove the detected gas, meanwhile, the signal of the output current was recorded till a steady state occurred. For the *I-V* measurements, they were also performed by this sensing system.

4.2.5. Characterizations.

The morphology of the samples on the device substrate were examined by SEM (S4800 Hitachi and Quanta 250 FEG) and atomic force microscopy (AFM, Dimension V Veeco-Bruker). The compositions were characterized by XRD (D/max2200, with Cu-Kα a radiation) and XPS (ESCALAB 250, Al-Kα radiation with energy of 1486.8 eV and spot size of 650 μm). Samples for the XRD and XPS measurements were prepared on the Si substrates under the same

conditions as that prepared on the device substrate. The KFM measurement was performed by NTEGRA Spectra system. The TEM was characterized by a JEOL JEM 2010 transition electronic microscope. The thickness of the SnO_2 layer was measured by the ellipsometry (SENTECH SE500).

4.3. Results and Discussions.

4.3.1. Adsorption Enhancements on the Triangular Convex.

Considering that the triangular convex is designed as an adsorption active site for enhancing surface adsorption, adsorption enhancement on the triangular convex shall be proved before the further ensemble of the triangular. To this end, we firstly investigate adsorption behaviors on the model material, i.e., SnO_2. In air, SnO_2 adsorbs atmospheric oxygen molecules (O_2), and a surficial reaction occurs, as shown in the following Equation 4-2:[1m]

$$O_2 \xrightarrow{e^-} O_2^- \xrightarrow{e^-} 2O^- \tag{4-2}$$

where O_2 is regarded as a charge accepting molecule to withdraw electrons from SnO_2. The resulting oxygen ions (e.g., O_2^- and O^-) with binding energy of 532.4 and 531.6 eV, different to the Sn^{4+}-bounded O (530.9 eV),[41] are demonstrated to exist on the SnO_2 surface by X-ray photoelectron spectroscopy (i.e., XPS, the inset in Figure 4-1b). The oxygen ions can carry negative surface potential on the SnO_2 surface.[33, 42] We introduce the ethanol gas to adjust the surface potential of the sample, where the previously negative surface potential will turn positively via the following reaction, Equation 4-3:[21b, 43]

$$C_2H_5OH_{(g)} + \frac{1}{2}O^- + \frac{1}{4}O_2^- \rightarrow CH_3CHO_{(g)} + H_2O_{(g)} + \frac{3}{4}e^- \tag{4-3}$$

in this mean, we can characterize adsorption quantity on the TCAAS by its surface-potential variation.

It is anticipated that, a large surface-potential increase would occur on the TCAAS when the TCAAS could adsorb more ethanol gaseous molecules. In this regard, we use KFM, a well-

accepted characterization of the surface-potential,[21b, 44] to estimate a surface-potential increase on the TCAAS.

Figure 4-1a schematically presents a KFM setup for measuring a surface-adsorption behavior on the TCAAS from a tilted and a cross-section view (the insets in Figure 4-1a), and the AFM image in Figure 4-1b shows that the TCAAS is formed by an SnO_2 layer coated on a convex substrate.

In a KFM scan, an alternating current (AC) voltage (V_{AC}) at frequency ω is added to the direct current (DC) voltage (V_{DC}) applied to the probe, and the voltage difference (ΔV_0) between the probe and the sample is presented by the following equation, Equation 4-4:

$$\Delta V_0 = V_{DC} - V_{PD} + V_{AC}\sin(\omega t) \quad (4\text{-}4)$$

where V_{PD} is a potential difference between the sample surface and the tip. The electrostatic force (F_{es}) between the tip and sample can thus be formulated as follow, Equation 4-5:

$$F_{es} = -\frac{1}{2}\frac{\partial C(z)}{\partial z}[V_{DC} - V_{PD} + V_{AC}\sin(\omega t)]^2 \quad (4\text{-}5)$$

where $\partial C(z)/\partial z$ is the gradient of the capacitance between the tip and the sample surface. From Equation 4-5, we can get the following equation, Equation 4-6:

$$F_{\omega} = -\frac{\partial C(z)}{\partial z}(V_{DC} - V_{PD})V_{AC}\sin(\omega t) \quad (4\text{-}6)$$

where F_{ω} with frequency ω is used to measure the V_{PD}. A lock-in amplifier is utilized to extract F_{ω}. As the output signal of the lock-in-amplifier is nullified and F_{ω} equals zero, the V_{PD} value can be measured by applying V_{DC} to the tip. Considering the sample is grounded, the value of V_{PD} is thus equal to the surface potential of the sample aroused by the adsorbed oxygen ions.

Based on the above mechanism of KFM, successive changes in atmospheres are made prior to each KFM image acquisition: (i) in air and (ii) with 25 ppm ethanol gas. Figure 4-1c and d respectively show surface potentials in air (Figure 4-1c) and with 25 ppm ethanol gas (Figure 4-1d). The corresponding potential profiles across a same selected area (Figure 4-1e) show that a distinct surface potential increase (ΔV = 2 mV) occurs on the TCAAS rather than the flat area,

after introducing the ethanol gas. This comparison of surface-potential variations demonstrates a fact that the TCAAS can adsorb more ethanol gaseous molecules to react with the surficial oxygen ions, proving an adsorption enhancement on the TCAAS.

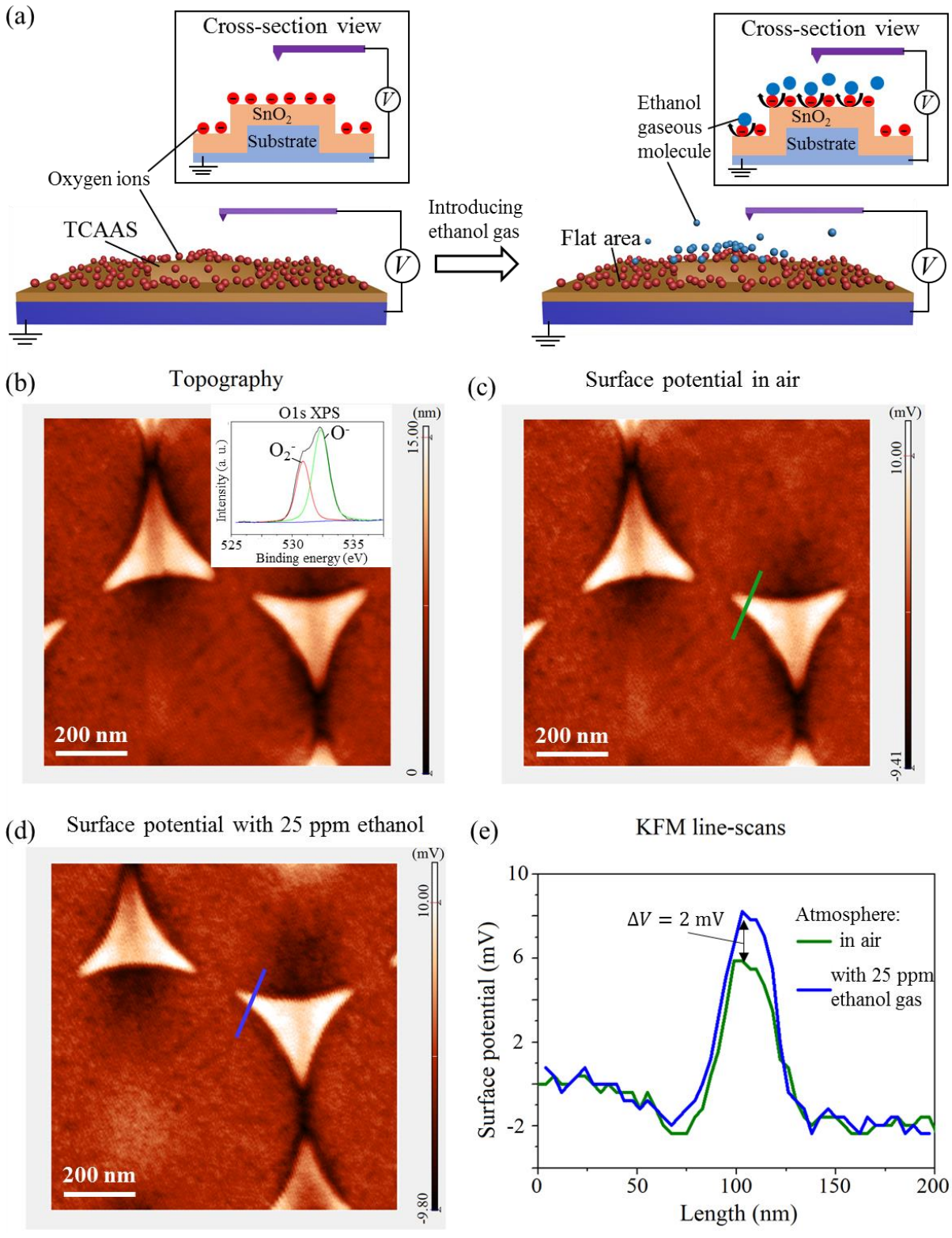

Figure 4-1. Adsorption enhancement on the TCAAS (i.e., triangular convex adsorption active site). (a) Schematic representations showing the KFM setup for measuring the adsorption enhancement on the TCAAS, an SnO_2 film on a substrate with the convex, from a tilted and a cross-section view (the insets in a). The TCAAS can adsorb more ethanol gaseous molecules to react with surficial oxygen ions than that of the flat area. (b-d) AFM (b) and KFM images (c and d) from the same area of the sample, and the sample O1s XPS spectrum (the inset in b) showing surficial oxygen ions (O_2^- and O^-) with binding energy of 532.4 and 531.6 eV. Successive changes in atmosphere are made prior to each KFM image acquisition: (c) in air and (d) with 25 ppm ethanol. (e) Surface potentials of line-scans across the TCAAS in air and with 25 ppm ethanol. Herein, a distinct surface-potential increase (ΔV = 2 mV) occurs on the TCAAS.

4.3.2. Fabrication of SnO_2 Film on a Triangle Array.

4.3.2.1. The Triangle Bases of Different Materials.

As a comparison, this work has used the colloidal monolayer (1000 nm nanosphere diameter) as a template, through which different materials, such as 10 nm of Ti, In, Au, and Mo are deposited. After removing the template, Figure 4-2a-d illustrate the SEM images of these deposited materials that all the deposited particles are defined into the same triangular morphology, however, their stacks are different. As compared to the Ti in Figure 4-2a, the In, Au, and Mo in Figure 4-2b-d show a particle distribution which is not suitable for the homogenous coating of SnO_2. In this regard, this work has chosen the Ti as the deposited materials.

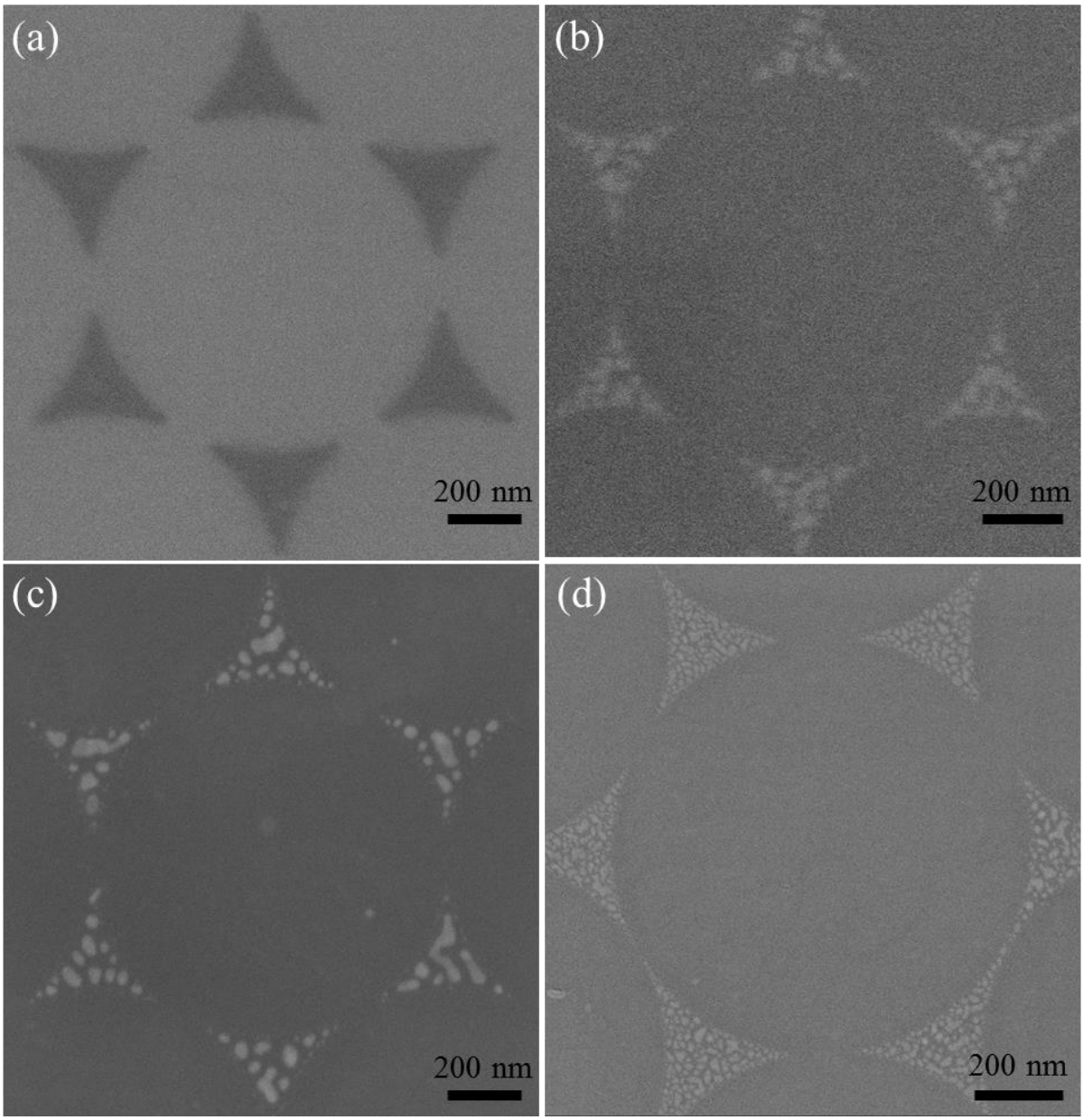

Figure 4-2. (a-d) The SEM images of the triangle bases for different deposited materials, such as Ti (a), In (b), Au (c), and Mo (d). The colloidal monolayer template consists of 1000-nm-diameter nanospheres.

4.3.2.2. AFM Images of Ti Triangle Bases.

By using the colloidal monolayers consisted of different diameters of nanospheres (from 500 to 2000 nm) as the templates, this work firstly deposits the 10 nm thickness of Ti on these template-covered areas. After removing the templates in CH_2Cl_2, all the samples are performed a measurement of AFM. In Figure 4-3a-d, the AFM images present that the Ti arrays have two

critical morphology parameters, i.e., the period (*d*) and highness, wherein the period ranges from 289-1154 nm and both of the Ti arrays are of the same highness of 10 nm. These period values are closely related to the template parameters, and the 10 nm of the Ti highness is equal to the deposited thickness. These two parameters indicate the formation of the Ti triangle array.

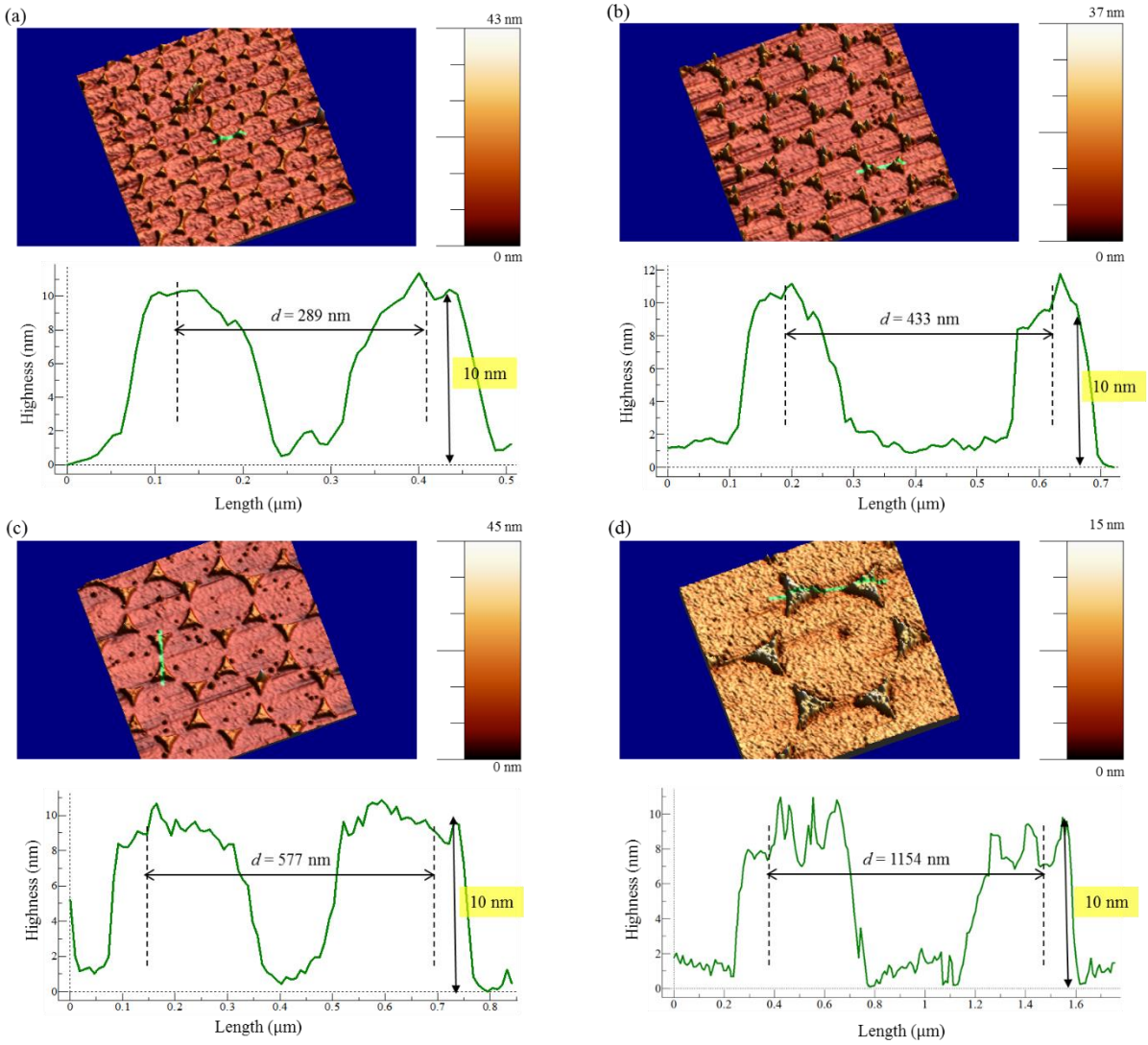

Figure 4-3. (a-b) The AFM images of the Ti triangle bases and their profiles. These bases are acquired by the colloidal monolayers consisted of 500 nm (a), 750 nm (b), 1000 nm (c), and 2000 nm (d) nanospheres.

4.3.2.3. The Ti Triangle Bases Coated with Different Deposition Cycles of SnO_2 in the ALD Process.

To acquire an optimized thickness of SnO_2, this work has deposited different thicknesses of SnO_2 layer on the Ti triangle array by varying the cycle number in the ALD process. Figure 4-4a-d show the Ti triangle arrays deposited with 0, 250, 500, 600 cycles of SnO_2 in the ALD. Without the SnO_2 deposition, the triangular morphology of the Ti base can be distinctly distinguished, and there are no particles on its surface (Figure 4-4a). Deposited with 250 cycles of the SnO_2, Figure 4-4b presents that small SnO_2 particles distribute sparsely on the triangle region and the other area. As the deposition cycle increases to 500, SnO_2 particles homogenously cover on the triangle base, especially on the triangle region, and form a continuous layer consisted of the triangular convexes (Figure 4-4c). Figure 4-4d confirms that, by the 600-cycle deposition, an SnO_2 layer is coated on the triangle base, whereas the triangle morphology on the SnO_2 layer is ambiguous. It suggests that an SnO_2 layer can be formed by 500 cycles of the SnO_2 deposition, but the excess deposition of SnO_2 such as the 600 cycles deposition is not good for the formation of the triangle structure on the SnO_2 layer. Therefore, the 500 cycles in the SnO_2 deposition is the optimized number, by which the thickness of the SnO_2 layer is characterized as 6.85 nm.

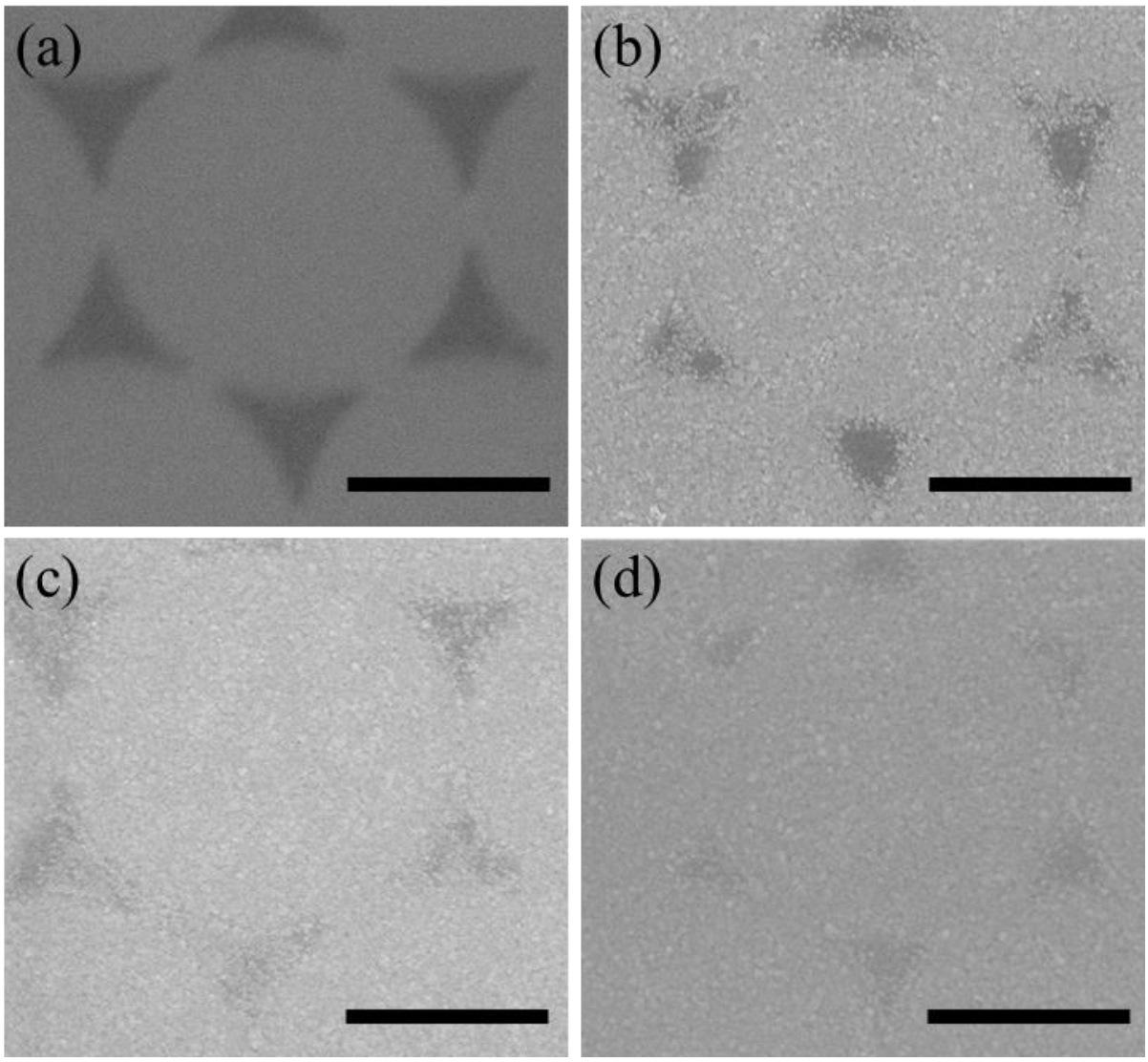

Figure 4-4. (a-d) The SEM images of the Ti triangle bases deposited with different cycles in the ALD process, such as 0 (a), 250 (b), 500 (c), and 600 (d). The bar length is 500 nm.

4.3.2.4. Fabrication Process of the Samples.

Fabrication process of the sample is described in Figure 4-5. Firstly, a colloidal monolayer was transferred to water (Figure 4-5i) and floated on the gas-liquid interface (Figure 4-5ii). Next this floated colloidal monolayer was picked up with a device substrate (Figure 4-5iii). For the configuration of the device substrate, interdigitated Pt/Ti electrodes were seated on a substrate, a p-type Si substrate capped with a 300-nm-thick oxide layer. After being dried up at room temperature for a day, the colloidal monolayer covered on the device substrate surface (Figure

4-5iv). This colloidal monolayer contains triangular voice spaces created by three neighboring nanospheres (the magnified image in Figure 4-5iv). A 10-nm-thick layer of Ti was then deposited over the colloidal-monolayer-coated substrate. In a lift-off step, the colloidal monolayer was removed in CH_2Cl_2, leaving behind a Ti triangle array (Figure 4-5v). Using this triangle array as a base, I deposited a 6.85-nm-thick film of SnO_2 for an ensemble of TCAASs and obtained a gas sensor (Figure 4-5vi).

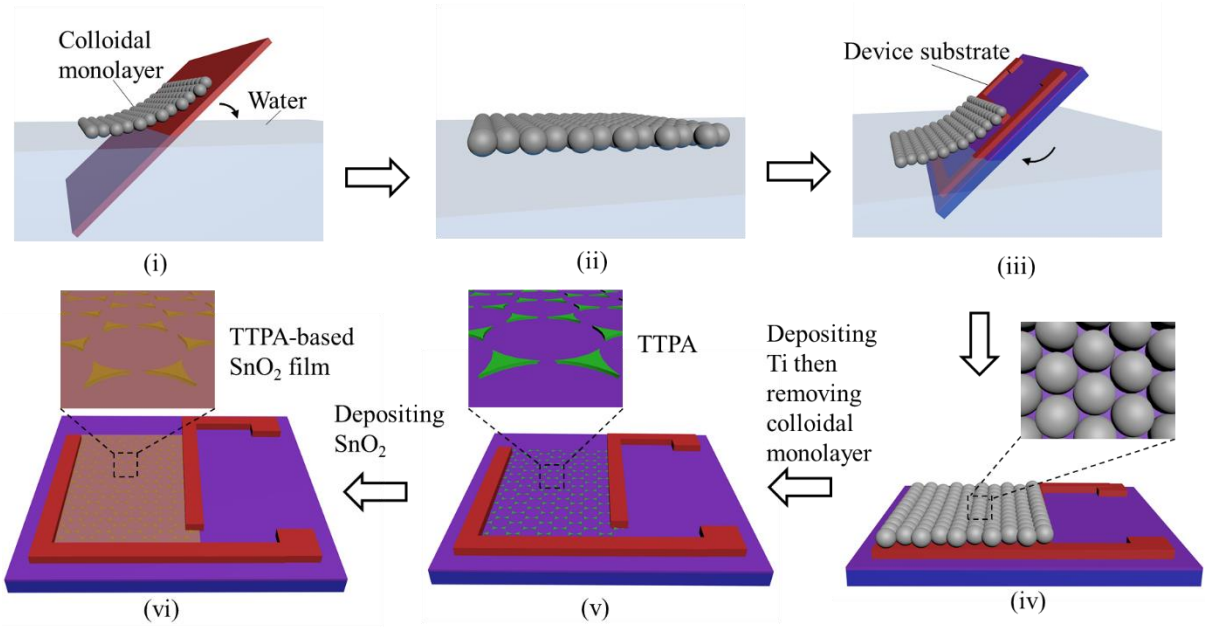

Figure 4-5. Schematic representation of procedures for directly fabricating the sample on a device substrate: (i) transferring a colloidal monolayer to water; (ii) the colloidal monolayer floated on the water; (iii) picking up the colloidal with a device substrate; (iv) the colloidal monolayer covering on the device substrate (the inset in iv showing the magnified image of the colloidal monolayer); (v) a triangle array obtained by physical vapour deposition method after the removal of the colloidal monolayer (the inset in v showing the magnified image of the array); (vi) the SnO_2 film on the array obtained after coating SnO_2 (the inset in vi showing the magnified image of the SnO_2 film).

4.3.3. The Morphology of SnO_2 Films on Triangle Arrays.

In Figure 4-6a-c, plane views of SEM images show colloidal monolayers consisting of different sizes nanospheres, such as 500 nm (Figure 4-6a), 750 nm (Figure 4-6b), 1000 nm (Figure 4-6c), and 2000 nm (Figure 4-6d) are hexagonally arranged to a large area that covers two neighboring electrodes. These colloidal monolayers, with triangular voice spaces, are then served as masks for physical vapor deposition of Ti. The insets in Figure 4-6e-h show the generated Ti triangle array with different alignment periods, such as 500 nm (the inset in Figure 4-6e), 750 nm (the inset in Figure 4-6f), 1000 nm (the inset in Figure 4-6g), and 2000 nm (the inset in Figure 4-6h). After coating with SnO_2, Figure 4-6e-h present a homogenous SnO_2 film on all triangle arrays, where a series of the arrayed triangular convexes are characterized by different alignment periods and sizes.

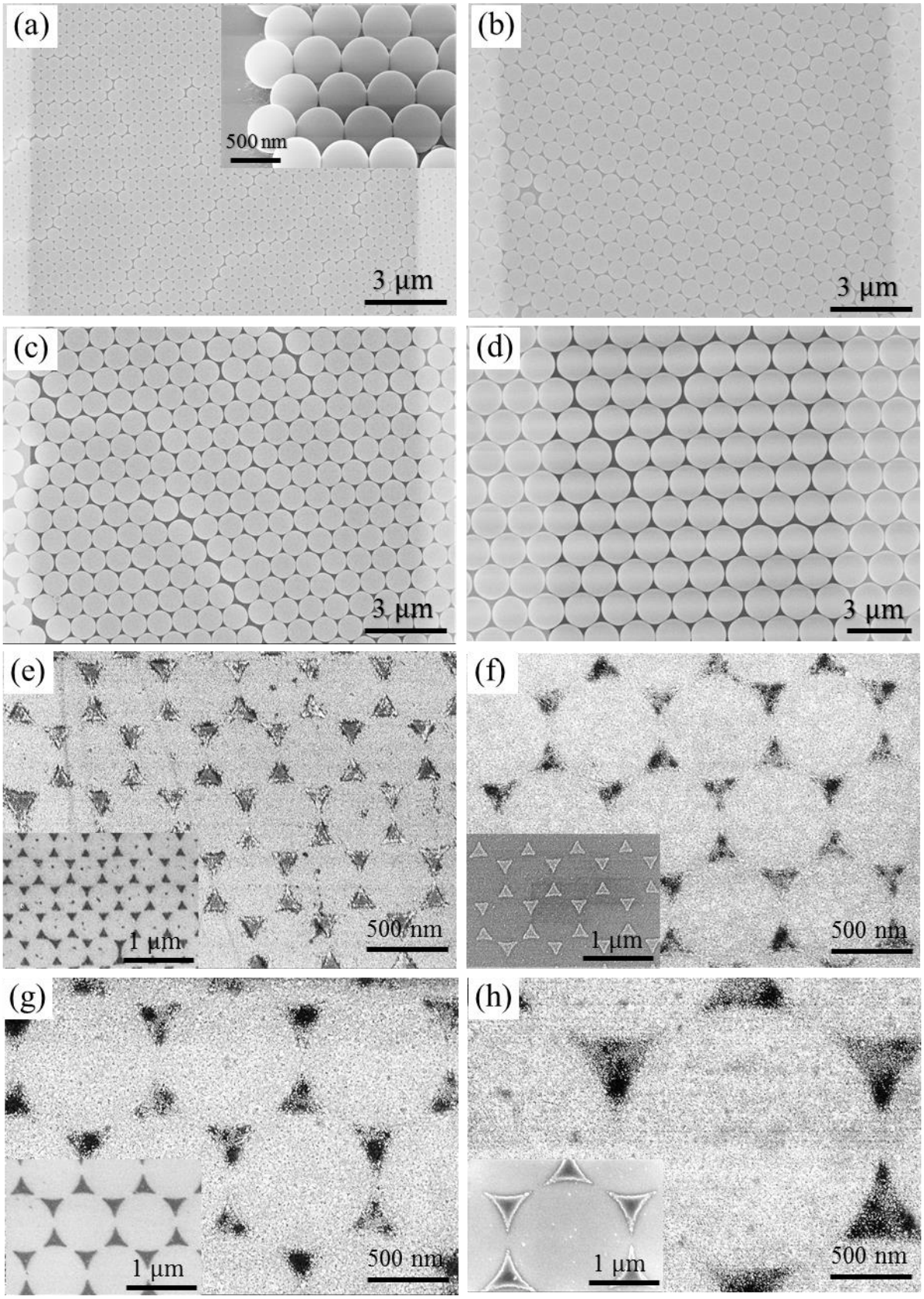

Figure 4-6. SEM images of samples and their colloidal monolayer templates. (a-d) Plane views of SEM images showing colloidal monolayers consisting of different sizes nanospheres, such

as 500 nm (a), 750 nm (b), 1000 nm (c), and 2000 nm (d) are hexagonally arranged to cover two neighboring electrodes. (e-h) SEM images showing SnO_2 films on the bases and these triangle array bases (the insets in e-h). The SnO_2 films with different inter-TCAAS spacings can be observed, such as 289 nm (e), 433 nm (f), 577 nm (g), and 1154 nm (h).

In Figure 4-7a-h, AFM images of the samples and their profile images describe the SnO_2 films are of different values of inter-TCAAS spacing (i.e., *d*) versus the template nanosphere diameters (*D*): 289 nm/500 nm (Figure 4-7a and b), 433 nm/750 nm (Figure 4-7c and d), 577 nm/1000 nm (Figure 4-7e and f), and 1154 nm/2000 nm (Figure 4-7g and h). The above morphology metrics produce different roughness averages for the samples with different *d*: 1.94 for the 289 nm, 1.59 for the 433 nm, 1.58 for the 577 nm, and 0.73 for the 1154 nm. These roughness averages indicate an order of the TCAAS from large to small for the sample with different *d*: the 289 nm > the 433 nm > the 577 nm > the 1154 nm. Additionally, the periods of these SnO_2-coated samples are consistent with those of their Ti bases.

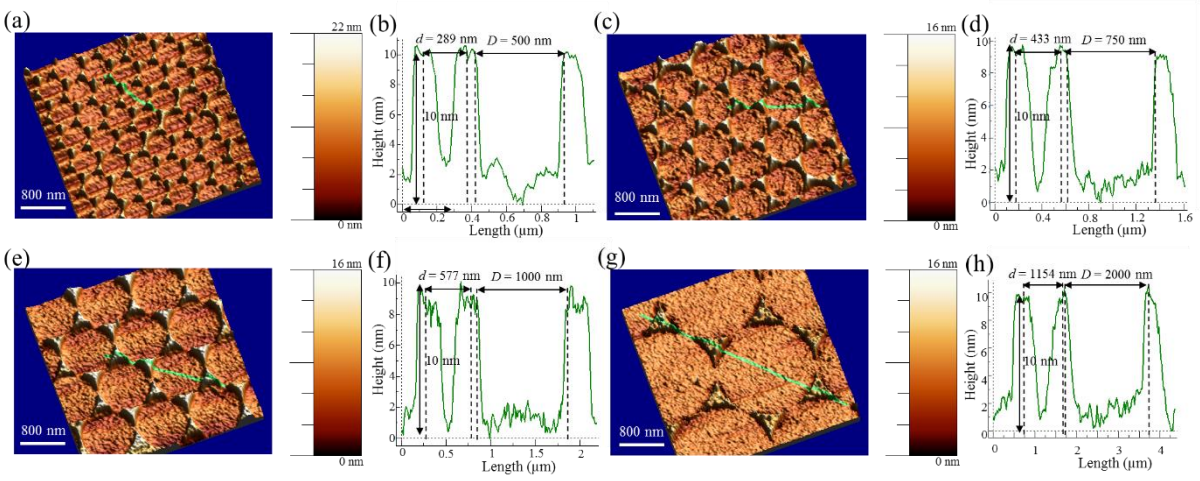

Figure 4-7. (a-h) AFM images and their profiles across selected areas showing SnO_2 films on triangle arrays with different values of *d*, such as 289 nm (a and b), 433 nm (c and d), 577 nm (e and f), and 1154 nm (g and h). *D* and *d* are the template nanosphere diameter and the inter-TCAAS spacing, respectively.

4.3.3. Composition Characterizations of the SnO_2 Film.

For the TEM characterization, the sample is scraped off from the SiO_2 substrate and collected for the measurement. Figure 4-8a shows the TEM image of the SnO_2 layer, of which average size of the crystallites is around 4 nm.

Samples for the XRD and the XPS characterization are prepared under the same conditions as those of the preparation on the device substrate. Figure 4-8b shows an XRD pattern of an SnO_2 layer on a Ti triangle array base, where the existence of main diffraction peaks (110), (101), and (211) of SnO_2 (JCPDS FILE No. 70-4177) proves that SnO_2 is formed by ALD. Chemical compositions of the SnO_2 layer on the base are determined by XPS, where Figure 4-8b shows four existed elements (Sn, O, Ti, and C) for the samples. The Sn3d peak presents two distinct peaks at binding energies of 486.5 and 494.9 eV those correspond to the 3d3/2 and 3d5/2 states of Sn^{4+}.[45] The O1s peak is associated with the oxygen ions on the sample surface. The Ti2p peak shows two distinct peaks at binding energies of 456 and 462 eV those correspond to metal Ti with few oxidation states from the process of the sample synthesis (the inset in Figure 4-8c),[46] demonstrating the existence of the Ti triangle array base. For the existence of C, it should be attributed to the residual template of polymer nanospheres.

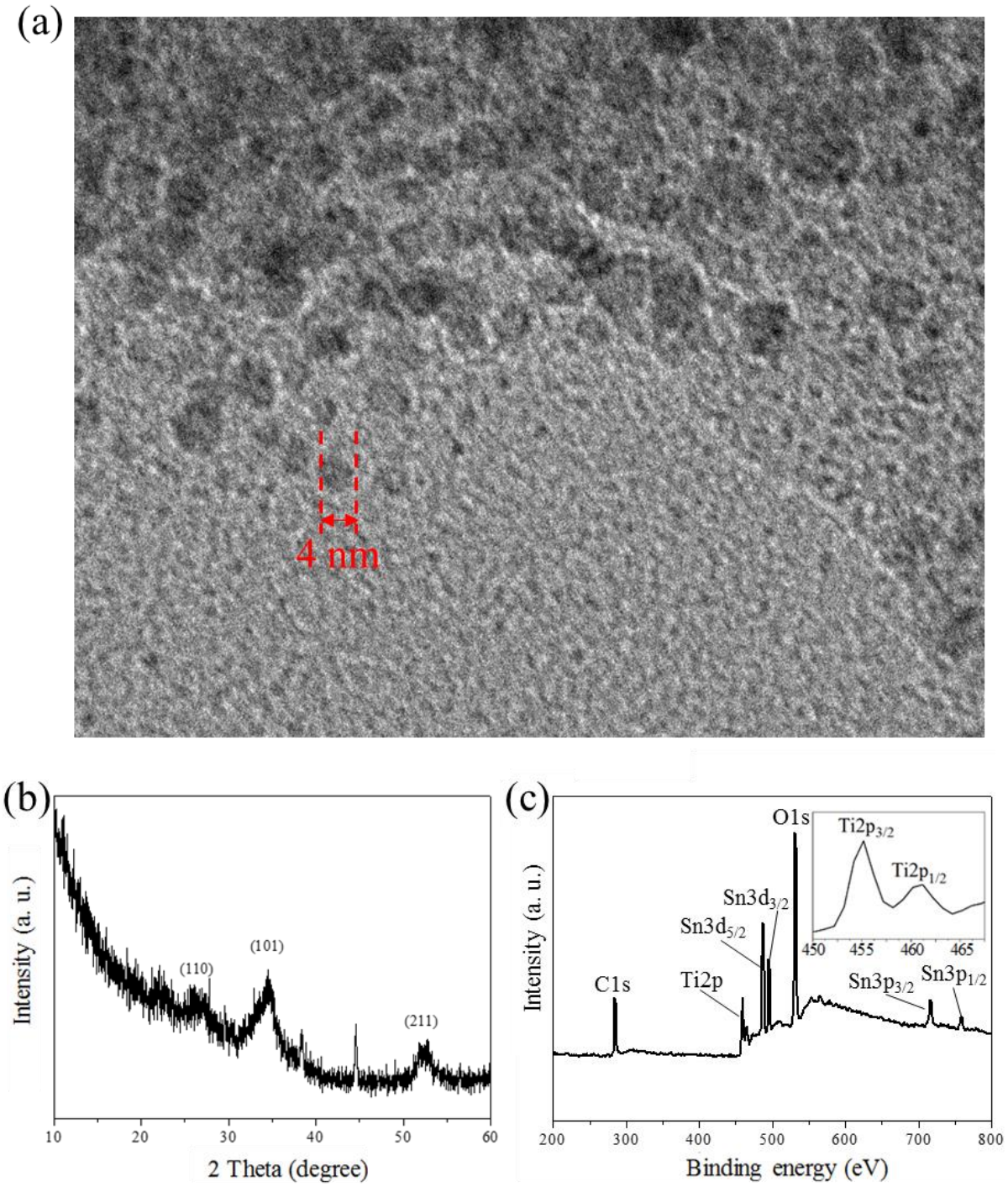

Figure 4-8. (a) The TEM image of the SnO_2 layer. (b) An XRD pattern of an SnO_2 layer on a Ti triangle array. (c) A survey scan XPS spectrum of an SnO_2 layer on the Ti triangle array, and the inset in c showing the high resolution of the XPS spectrum of Ti2p.

4.3.4. Gas-Sensing Properties of the SnO_2 Film Gas Sensor.

SnO_2 films with different TCAAS sizes are used as a gas sensor (the inset in Figure 4-9b) for detecting different concentrations of ethanol gases (25, 18, 12, and 6 ppm) at room temperature.

Applied with a voltage of 4 V, the gas sensor sensitivity is defined as I_{gas}/I_{air}. I_{gas} and I_{air} are output currents of the sensor in air and the detecting atmosphere, respectively. Figure 4-9a presents gas-sensing responses to different concentrations of ethanol gases for the samples with *d* values of 289, 433, 577, and 1154 nm. It is found that the gas-sensing sensitivity increases with the increasing of the TCAAS (i.e., decreasing of *d*). Shown by the sample with the largest TCAAS (*d* = 289 nm), the most sensitive gas-sensing is of the sensitivity (i.e., I_{gas}/I_{air}) that can be up to 2.42, 1.99, 1.67, and 1.52 for 25, 18, 12, and 6 ppm of ethanol gases. These sensitive gas-sensing responses indicate that this sample has a low detection limit of around 6 ppm ethanol gas or even the lower. In contrast, the sample with the smallest TCAAS (*d* = 1154 nm) is of a degraded sensitivity that is more than 2-times weaker than that of the largest TCAAS in detections of 6-25 ppm ethanol gases. Even the ethanol gas is up to 25 ppm, the gas-sensing sensitivity of the sample with *d* of 1154 nm is just 1.08. Without TCAASs on an SnO_2 film (i.e., *d* = 0), the sample does not have gas-sensing responses to the ethanol gas ranging from 6 ppm to 25 ppm, as depicted in Figure 4-9b.

To investigate the mechanism of this TCAAS origin of gas-sensing, we firstly fabricate the samples into a field effect transistor. Varying V_g from 0 to 10 V (step = 2 V), Figure 4-9c-f show I_{ds}-V_{ds} output curves of the samples with different *d*: 289 nm (Figure 4-9c), 433 nm (Figure 4-9d), 577 nm (Figure 4-9e), and 1154 nm (Figure 4-9f). Among them, I_{ds} and V_{ds} are respectively a source-drain current and a voltage, and V_g is a gate voltage. That the increasing V_g leads to the increasing of I_{ds} suggests that an n-type conductance channel exists on all SnO_2 films,[32] of which carrier density (*n*) is around 2.3×10^{23} cm^{-3} (characterized by Hall effect measurements). Introduced ethanol gaseous molecules can increase carrier density ($\Delta n > 0$) of these n-type samples to enhance their current intensity (characterized by $I_{gas}/I_{air} > 1$).[27] As shown in Table 4-1, with introducing 25 ppm ethanol gas, the current intensity increases 142%, 45%, 12%, and 8% for the samples with *d* = 289, 433, 577, and 1154 nm (calculated by $\Delta I/I_{air}$,

$\Delta I = I_{gas} - I_{air}$). Given by the correlation between the current and the carrier density variation ($\Delta I = \Delta nAvQ$, A, v, and Q are respectively the cross-sectional area of conductor, carrier velocity, carrier charge), the carrier density increase is then estimated to 3.27×10^{23}, 1.04×10^{23}, 0.28×10^{23}, and 0.18×10^{23} cm^{-3} for the samples with TCAAS from large to small. According to Equation 4-2, one introduced ethanol gaseous molecule can react with 3/4 adsorbed oxygen ion to increase 3/4 carrier for SnO_2. The adsorption quantity of ethanol gaseous molecules is then estimated to 4.35×10^{23}, 1.38×10^{23}, 0.37×10^{23}, 0.25×10^{23} for the sample with TCAAS from large to small. The estimated adsorption quantity of ethanol gas on the large-TCAAS sample is distinctly higher than that of the small-TCAAS. Together with the TCAAS-dependent sensitivity, these results suggest that the high sensitivity manifested by the large-TCAAS sample should be attributed to its large adsorption quantity of ethanol gas.

Table 4-1. Calculated adsorption quantity of ethanol gas for samples with different TCAAS sizes (i.e., different d values).

d [nm][a)]	$\Delta I/I_{air}$ [%]	Δn [cm^{-3}][b)]	N[c)]	I_{gas}/I_{air}
289	142	3.27×10^{23}	4.35×10^{23}	2.42
433	45	1.04×10^{23}	1.38×10^{23}	1.45
577	12	0.28×10^{23}	0.37×10^{23}	1.12
1154	8	0.18×10^{23}	0.25×10^{23}	1.08
0	0	0	0	1

[a)]The inter-TCAAS spacing; [b)] Carrier density variations for introducing 25 ppm ethanol gas; [c)]Adsorption quantity of ethanol gas under 25 ppm ethanol gas.

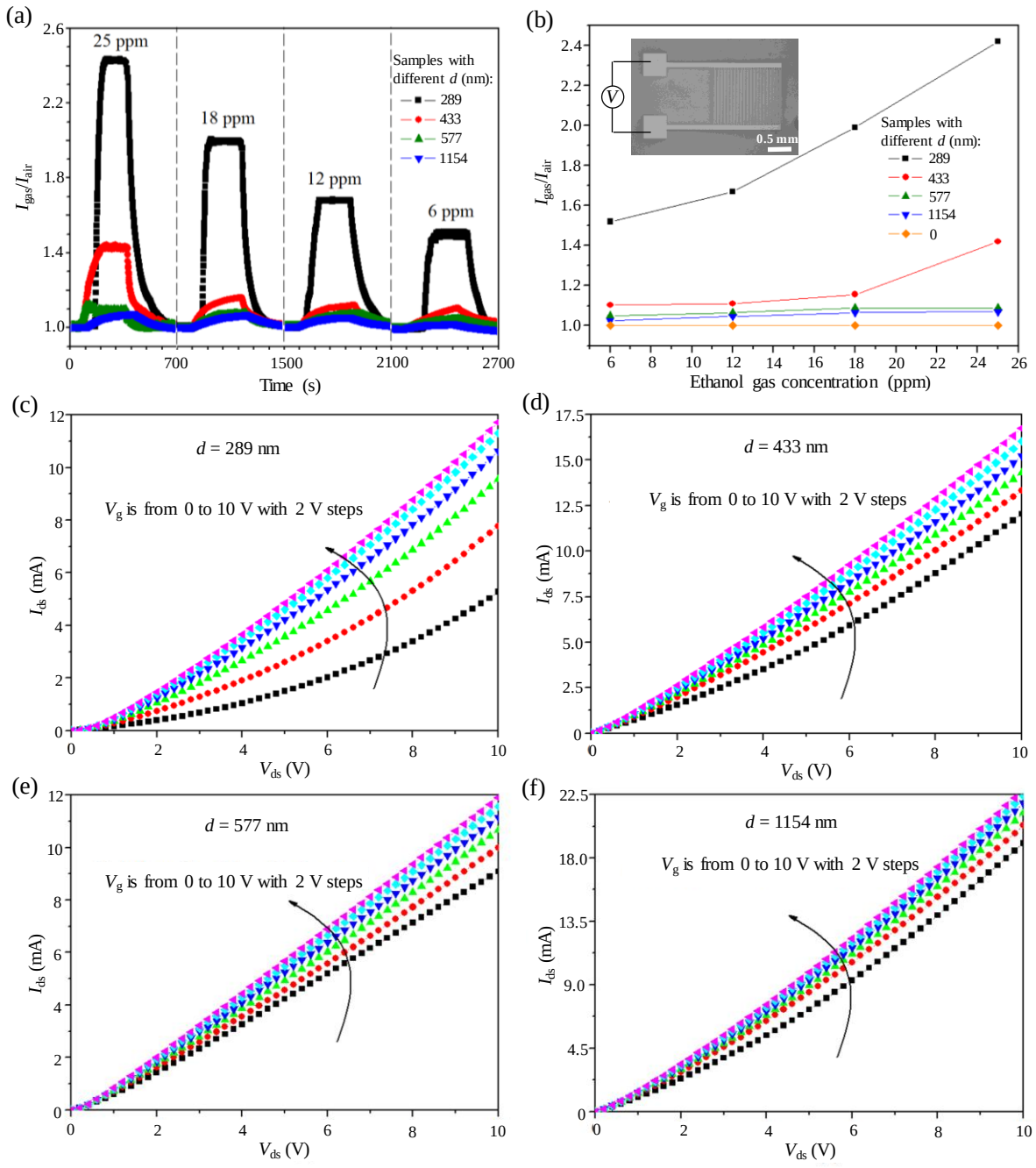

Figure 4-9. Gas-sensing of the samples: (a) Gas-sensing responses to different concentrations of ethanol gases for different samples at room temperature. The samples are of different values of *d*, such as 289, 433, 577, and 1154 nm. (b) The gas-sensing sensitivity (I_{gas}/I_{air}) versus ethanol concentration (6, 12, 18 and 25 ppm) for the SnO_2 films on triangle arrays and the flat SnO_2 thin film (i.e., *d* is 0 μm). The inset shows an SEM image of the gas sensor device. (c-f) I_{ds}-V_{ds} output curves of SnO_2 films with different *d*, such as 289 nm (c), 433 nm (d), 577 nm

(e), 1154 nm (f). All the I_{ds}-V_{ds} curves were obtained by V_g varying from 0 to 10 V (step = 2 V). An n-type behaviour of the samples can be seen by a fact that the increasing V_g leads to the increasing of I_{ds}.

Additionally, this work has measured the gas-sensing stability of the sample. For the long-term stability, this work has tested the gas-sensing response of the 289 nm sensor to the 25 ppm ethanol for three times. Each time has an interval time of a week, during which this work preserves the sample in air without considerate conditions. As a result, Figure 4-10a shows the sensitivity of the gas sensor can stay in the range of 2.30-2.45, indicating the sample is of a good long-term stability for two weeks. Considering that the humidity usually influences the gas-sensing stability, this work has carried out a gas-sensing measurement for the 289 nm sample, where the humidity is varied from 28% to 32%. It is found that the sensor remains a stable response to 25 ppm ethanol (Figure 4-10b).

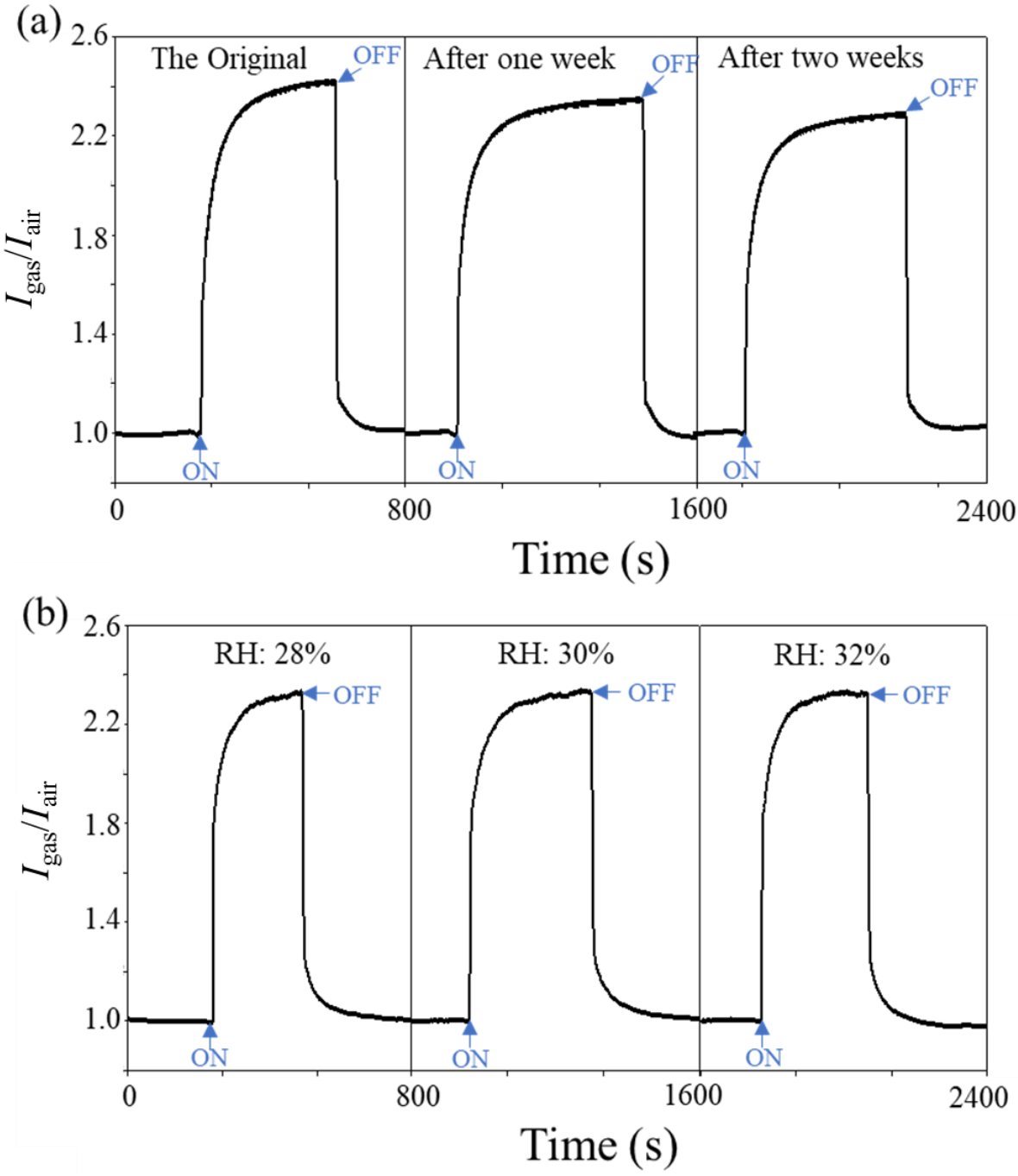

Figure 4-10. (a) The room-temperature response of the 289 nm sample to 25 ppm ethanol gas in a two-week measurement. Each test has an interval time of a week. (b) The gas-sensing response of the 289 nm sample to 25 ppm ethanol gas under different humidities (RH), ranging from 28% to 32%, at room temperature.

In Figure 4-11, the investigation of gas-sensing selectivity confirms the specific response of the sample (e.g., the 289-nm-period sample) to ethanol gas. In this work, the target gases

include 5% H_2, 10% oxygen, and 25 ppm of methanol, ethanol, acetone, isopropanol, and NO_2. The sample sensitivity to the ethanol gas is higher than the others, and thus the ethanol gas is also selected as a model gas for the following mechanism study. Note that the selectivity of the sample is fair as compared to those reported,[47-55] and a comparison shown in Table 4-2 suggests that this fair selectivity should be related to the low operated temperature (room temperature) and the low target gas concentration (25 ppm) in this work. Additionally, compared to the fair selectivity shown by the sample in this work, the sample sensitivity of the specific response to the ethanol gas is high. In Table 4-3, this work makes a comparison among the room temperature responses of SnO_2 gas sensors to the reductive gases,[10d, 56-61] and finds that the sensitivity of the 289 nm sample is also competitive. For example, in the room temperature detection of ethanol gas, the high sensitivity in the references is around 7 for 50 ppm ethanol,[57] which is closed to that of the sample used in this work.

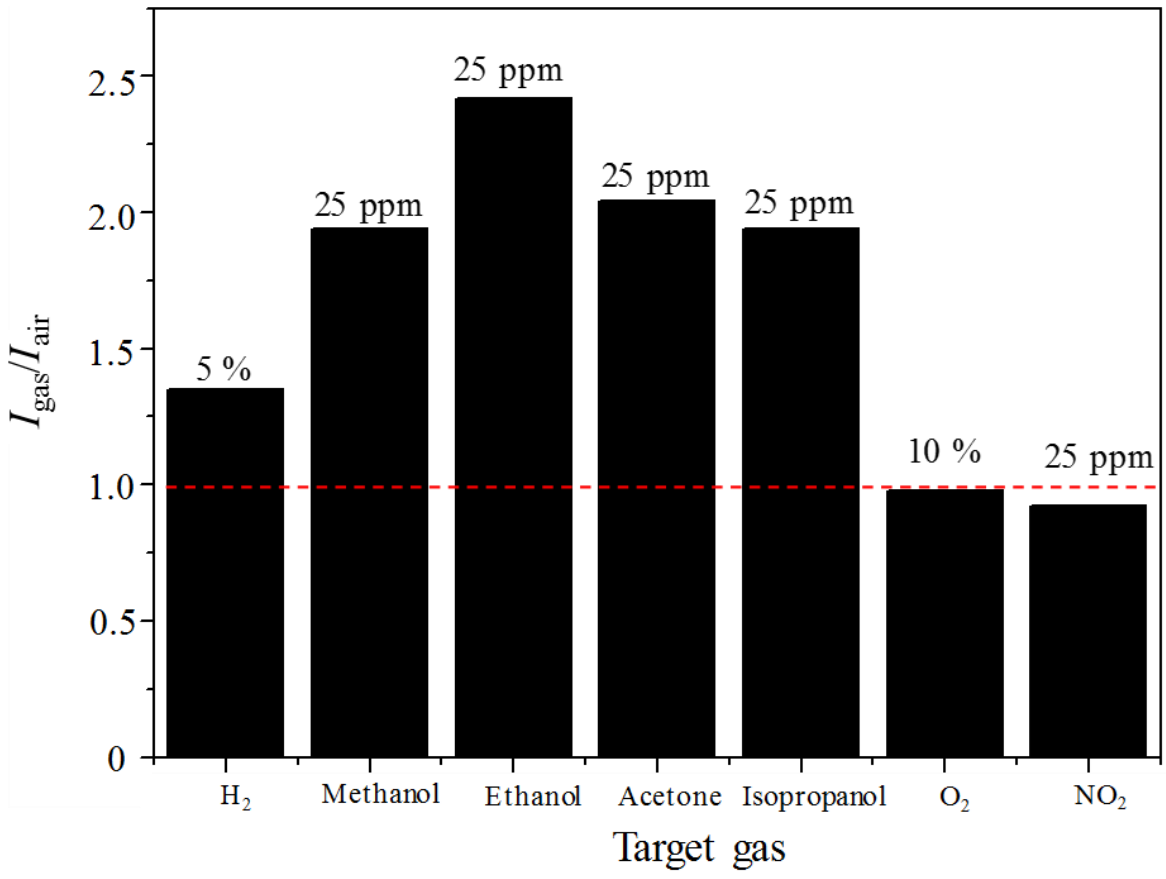

Figure 4-11. Gas-sensing responses of the SnO_2-layer gas sensor (with a 289 nm period) to different target gases, including 5% H_2, 10% oxygen, 25 ppm of methanol, ethanol, acetone, and NO_2.

Table 4-2. The Gas-Sensing Selectivity of the SnO_2 Gas Sensors.

Material Morphology	Working Temperature	Target Gas	Sensitivity/Gas Concentration	References
Hierarchical Fibers	300℃	Ethanol	67/500 ppm	47
		Methanol	22/500 ppm	
		Acetone	14/500 ppm	
Hollow Nanofiber	300℃	Ethanol	76/500 ppm	48
		Methanol	3.6/500 ppm	
		Acetone	21/500 ppm	
Porous Nanoflowers	240℃	Ethanol	7.5/10 ppm	49
		Methanol	5/10 ppm	
		Acetone	4/10 ppm	
Porous Nanocrystalline	150℃	Ethanol	42/100 ppm	50
		Methanol	5/100 ppm	
		Acetone	2.5/100 ppm	
Mesoporous Structure	240℃	Ethanol	4.95/100 ppm	51
		Methanol	2.55/100 ppm	
		Acetone	5.05/100 ppm	
Thin Film	25℃	Ethanol	1.07/47 ppm	52
		Methanol	1.01/47 ppm	
		Acetone	1.03/47 ppm	

Nanorod Arrays	370℃	Ethanol	3/1 ppm	53
	320℃	Methanol	2/1 ppm	
	320℃	Acetone	4/1 ppm	
Hierarchical Nanosheets	275℃	Ethanol	32.7/100 ppm	54
		Acetone	7.5/100 ppm	
Porous Nanospheres	400℃	Ethanol	8.7/100 ppm	55
		Methanol	8/100 ppm	
A Layer with Triangular Convexes	25℃	Ethanol	2.42/25 ppm	This Work
		Methanol	1.95/25 ppm	
		Acetone	2.03/25 ppm	

Table 4-3. The Room Temperature Responses of SnO_2 Gas Sensors to the Reductive Gases.

Material Morphology	Working Temperature	Target Gas	Sensitivity/Gas Concentration	References
Quantum Dot	75℃	Ethanol	2.5/50 ppm	56
Nanorod Array	Room Temperature	Ethanol	1.09/25 ppm	10d
Hollow Nanospheres	Room Temperature	Ethanol	7/50 ppm	57
Nanobelt	43℃	Ethanol	7.65/100 ppm	58
Nanowires	Room Temperature	CO	4/20 ppm	59
Nanoparticles	Room Temperature	NH_3	34/600 ppm	60

Nanobelt	Room Temperature	H_2	1.6/2%	61
A Layer with Triangular Convexes	Room Temperature	Ethanol	2.42/25 ppm	This Work

4.3.5. Adsorption Enhancements on the SnO_2 Gas Sensors.

To demonstrate the existence of ethanol gaseous molecules on the sample surface for introducing ethanol gas, this work has measured the Fourier-transform infrared spectroscopy (FTIR) for the sample, before which the sample is stored in the atmosphere permeated with ethanol gas. In the FTIR test, this work takes the sample out of the ethanol atmosphere, and immediately carries out this characterization in order to detect the adsorbed ethanol gas on the sample surface before its removal. Figure 4-12 shows the FTIR spectrum of the sample that, there are three featuring peaks for O-H (3390 cm^{-1}), C-H (2970 cm^{-1}), and C-O (1055 cm^{-1}) of ethanol molecules. It means that, by the FTIR characterization, the ethanol gaseous molecules are confirmed to exist on the sample surface.

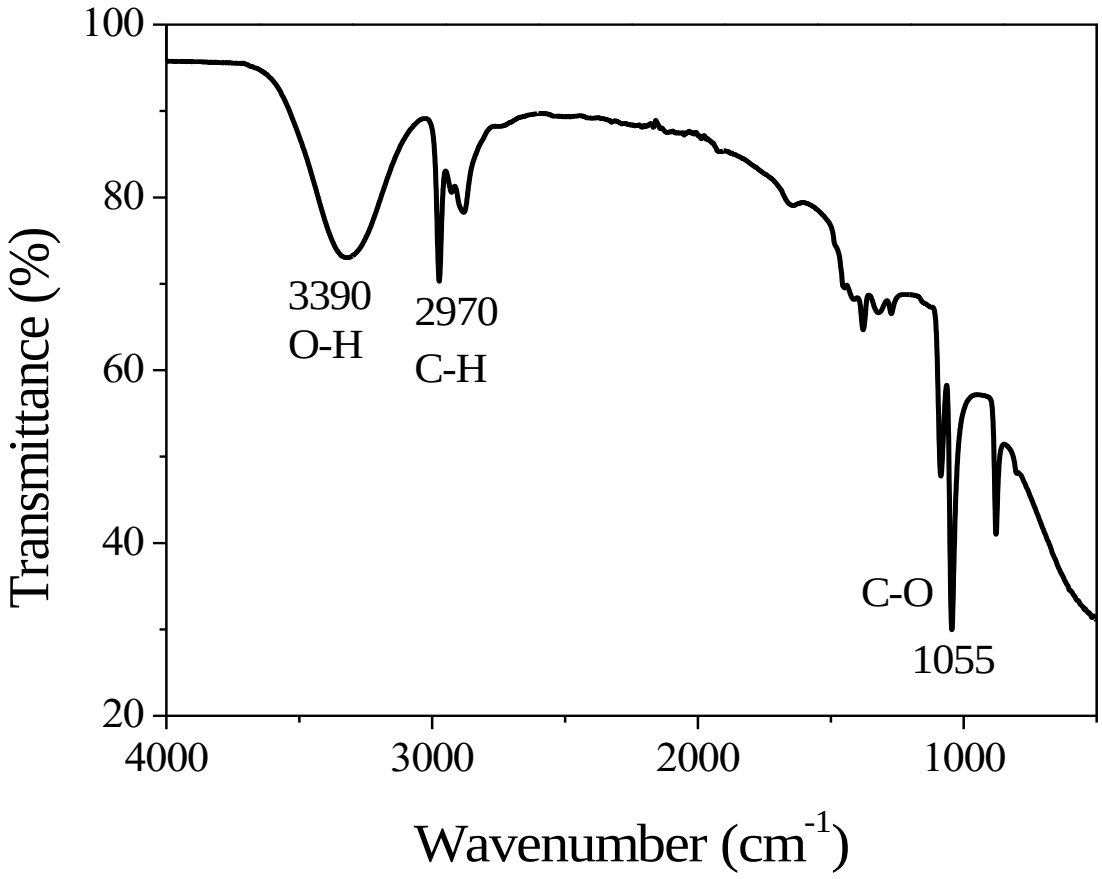

Figure 4-12. The FTIR spectrum of the sample.

Next, to demonstrate the TCAAS-origin of the sensitivity is positively associated with the adsorption quantity of ethanol gas, this work performs KFM characterizations on a 3.5 μm^2 area of each sample. Figure 4-13a schematically shows KFM setups, a line scanned across the samples, and the KFM roughness statistics based on the line-scanned surface potentials. Note that results of the KFM roughness statistics can show the percentages of different surface potential values. A positive and a negative shift of a surface-potential-percentage-dependent curve represent an increase and a decrease of surface potential, respectively. Next, according to the detecting atmosphere aforementioned, successive changes in the atmosphere are made prior to each KFM image acquisition: (i) in air and (ii) with 25 ppm ethanol (i.e., without and with ethanol gas). Figure 4-13b-e present the KFM images of the samples with *d* of 289 nm (Figure 4-13b), 433 nm (Figure 4-13c), 577 nm (Figure 4-13d), and 1154 nm (Figure 4-13e),

where the right column describes the KFM roughness statistics. It is found that, the samples with *d* of 289 and 433 nm exhibit a distinctly positive shift of the curve. In contrast, an ambiguous shift is observed for the sample with *d* of 577 and 1154 nm. This comparison reveals that a larger surface potential increase occurs on the samples with *d* of 289 and 433 nm. As shown in Table 4-4, the increase of surface potential average is up to 0.58 and 0.18 mV for the samples with *d* of 289 and 433 nm, respectively. Whereas the ambiguous increases of 0.06 and 0.005 mV respectively occur for the samples with *d* of 577 and 1154 nm. Considering the fact that the surface potential of the SnO_2 can increase for the introduction of the ethanol gas, the larger surface potential increase in the 289 nm and the 433 nm sample proves their higher adsorption quantity of the ethanol gas, where they possess a large TCAAS.

Table 4-4. Calculated surface-potential-average variations of the samples with different TCAAS sizes (i.e., different *d* values) for 25 ppm ethanol gas.

d [nm][a)]	*R*[b)]	Δ*V* [mV][c)]
289	1.94	0.58
433	1.59	0.18
577	1.58	0.06
1154	0.73	0.005

[a)]The inter-TCAAS spacing; [b)]Roughness averages for the samples; [c)]Calculated surface-potential-average variations of the samples for 25 ppm ethanol gas.

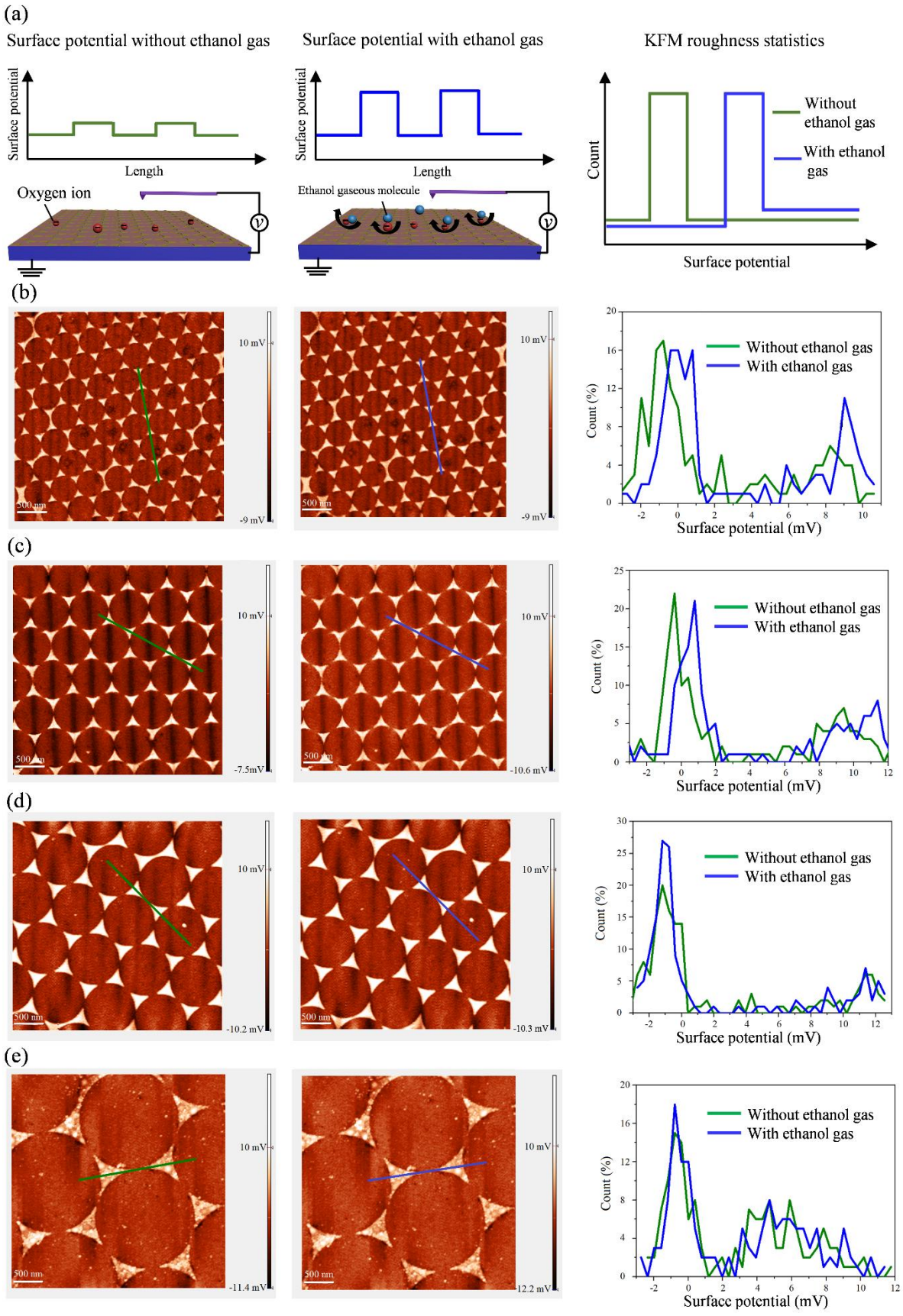
(a)
Surface potential without ethanol gas
Surface potential with ethanol gas
KFM roughness statistics
Surface potential
Length
Oxygen ion
Ethanol gaseous molecule
Count
Without ethanol gas
With ethanol gas
Surface potential
(b)
(c)
(d)
(e)
10 mV
-9 mV
-7.5mV
-10.6 mV
-10.2 mV
-10.3 mV
-11.4 mV
-12.2 mV
500 nm
Count (%)
Surface potential (mV)

Figure 4-13. Surficial potential variations of SnO_2 films on triangle arrays during gas-sensing. (a) Schematic representations showing the KFM setup for measuring a line-scanned surface potential across the samples, and the KFM roughness statistics based on the line-scanned surface potential. Successive changes in atmosphere are made prior to each image acquisition: (i) in air and (ii) with 25 ppm ethanol, i.e., without and with ethanol gas. The right column shows KFM roughness statistics based on a line-scanned surface potential across a certain length of the samples. (b-e) KFM images of the samples with different values of *d*, such as 289 nm (b), 433 nm (c), 577 nm (d) and 1154 nm (e).

4.4. Conclusions.

To summarize, this work offers a concept of adsorption active site for designing gas sensors with high sensitivity. In this concept, the adsorption active site is an area on the sensor where an adsorption enhancement can be realized. Depositing an SnO_2 film on a triangle array for an ensemble of triangular convex adsorption active sites (i.e., TCAASs), and the generated SnO_2 gas sensor exhibits an adsorption-active-site-dependent sensitivity in a room temperature detection of ethanol gases. Shown by the sample with the largest TCAAS, the most sensitive gas-sensing presents a low detection limit of around 6 ppm ethanol gas. In contrast, without adsorption active sites, the flat film of SnO_2 has no responses even to 25 ppm ethanol gas. To reveal the mechanism of this adsorption-active-site-origin of sensitivity, this work uses KFM to investigate adsorption quantity of ethanol gas on the sample by its surface potential variation for ethanol gas. Importantly, the KFM results distinctly show an adsorption enhancement on the TCAAS by it large increase of surface potential after introducing ethanol gas. Based on the above, this work confirms that the creation of adsorption active sites can efficiently enhance surface adsorption for sensitive gas-sensing. It is anticipated that the concept of the adsorption active site is applicable to different gas-sensing systems, serving as a general gas-sensing concept to design future gas sensors.

5. Summary and Outlook

To summarize, the template-based method is demonstrated to be an efficient way to fabricate nanostructure-array-based gas sensors with an enhanced performance. The related works in this dissertation are concluded below:

(1) The first research indicates a gas-sensing mode, CMDGS, different from the conventional mode of CDDGS, for inorganic semiconductor gas sensors. To demonstrate the CMDGS, this work designs and fabricates a regular array of SnO_2 nanorods on a bottom film, then use it for the room temperature gas-sensing. By modulating the length of arrayed nanorods, the gas-sensing behavior changes from CDDGS to a complete CMDGS mode. Moreover, the realized CMDGS-mode gas sensor is of a more than 4-times higher sensitivity than that of the CDDGS-mode. It is anticipated that the proposed CMDGS mode shall be applicable to other gas sensing systems of different inorganic semiconductors, providing a concept for designing gas sensors.

(2) The second research work offers a concept of adsorption active site for designing gas-sensors with high sensitivity. In this concept, the adsorption active site on the sensor is designed to facilitate the surface adsorption. By depositing an SnO_2 film on a triangle array, an SnO_2 film gas sensor with an ensemble of triangular convex adsorption active sites (i.e., TCAASs) exhibits an adsorption-active-site-dependent sensitivity in a room temperature detection of ethanol gases. Shown by the sample with the largest TCAAS, the most sensitive gas-sensing presents a low detection limit of around 6 ppm ethanol gas. In contrast, without adsorption active sites, the flat film of SnO_2 has no responses even to 25 ppm ethanol gas. To reveal the mechanism of this adsorption-active-site-origin of sensitivity, I use KFM to investigate adsorption quantity of ethanol gas on the sample by its surface potential variation for ethanol gas. Importantly, the KFM results distinctly show an adsorption enhancement on the TCAAS by it large increase of surface potential after introducing ethanol gas. Based on the above, this work confirms that the creation of adsorption active sites can efficiently enhance surface

adsorption for sensitive gas-sensing. It is anticipated that the concept of the adsorption active site is applicable to different gas-sensing systems, serving as a general gas-sensing concept to design future gas sensors.

Future researches about the template-assisted fabrications of nanostructure-array gas sensor shall more focus on their wireless portability and miniaturized integrability. Since the wide range applications of the notebooks and cellphone, the wireless portability of the sensor integrated in such portable electronics becomes increasingly important. Combining the arrays with the triboelectric effect looks promising for the wireless portability of the nanostructure-array-based sensor. In the recent works conducted by Wang and co-workers, vibrations from touching or water wave produce the triboelectric effect for the arrays, and the generated environment power, ranging from micro- to milli-Watt, is applicable for the array-based sensor operation.[76] Such self-powered nanosystems fulfil the wireless portability of the array-based sensors. Additionally, the miniaturized integrability of the array-based sensors is critical to the fabrication of e-skin, which shall integrate a wide range of sensor networks (e.g., pressure, strain, light, temperature, and humidity). The micro-scale size of the arrayed nanostructure is highly accessible to the multiple integration, and thus it is promising to conduct a further research on the miniaturized integrability of the array-based sensors.

6. Bibliography

[1] a) X. Pan, X. Liu, A. Bermak, Z. Fan, *ACS Nano* **2013**, *7*, 9318; b) S. Cui, H. Pu, S. A. Wells, Z. Wen, S. Mao, J. Chang, M. C. Hersam, J. Chen, *Nat. Commun.* **2015**, *6*, 8632; c) J. Zhang, X. Liu, G. Neri, N. Pinna, *Adv. Mater.* **2016**, *28*, 795; d) X. Li, M. Le Thai, R. K. Dutta, S. Qiao, G. T. Chandran, R. M. Penner, *ACS Sensors* **2017**, *2*, 282; e) W.-T. Koo, S. Qiao, A. F. Ogata, G. Jha, J.-S. Jang, V. T. Chen, I.-D. Kim, R. M. Penner, *ACS Nano* **2017**, *11*, 9276; f) M.-A. Stoeckel, M. Gobbi, S. Bonacchi, F. Liscio, L. Ferlauto, E. Orgiu, P. Samorì, *Adv. Mater.* **2017**, *29*, 1702469; g) W. Huang, X. Zhuang, F. S. Melkonyan, B. Wang, L. Zeng, G. Wang, S. Han, M. J. Bedzyk, J. Yu, T. J. Marks, A. Facchetti, *Adv. Mater.* **2017**, *29*, 1701706; h) Z. Wang, L. Huang, X. Zhu, X. Zhou, L. Chi, *Adv. Mater.* **2017**, *29*, 1703192; i) N. Michieli, R. Pilot, V. Russo, C. Scian, F. Todescato, R. Signorini, S. Agnoli, T. Cesca, R. Bozio, G. Mattei, *RSC Adv.* **2017**, *7*, 369-378; j) L. Qin, L. He, J. Zhao, B. Zhao, Y. Yin, Y. Yang, *Sens. Actuat. B-Chem.* **2017**, *240*, 779; k) S. K. Cha, J. H. Mun, T. Chang, S. Y. Kim, J. Y. Kim, H. M. Jin, J. Y. Lee, J. Shin, K. H. Kim, S. O. Kim, *ACS Nano* **2015**, *9*, 5536; 1l) G. Korotcenkov, *Mater. Sci. Eng. B* **2007**, *139*, 1; m) X. Huang, F. Meng, Z. Pi, W. Xu, J. Liu, *Sensor. Actuat. B: Chem.* **2004**, *99*, 444.

[2] a) S. Rasappa, T. Ghoshal, D. Borah, R. Senthamaraikannan, J. D. Holmes, M. A. Morris, *Sci. rep.* **2015**, *5*, 13270; b) T. Tian, J. Dong, J. Xu, *Microchim. Acta* **2016**, *183*, 1925.

[3] G. B. Jung, Y. M. Bae, Y. J. Lee, S. H. Ryu, H.-K. Park, *Appl. Surf. Sci.* **2013**, *282*, 161.

[4] Y. Li, G. Duan, G. Liu, W. Cai, *Chem. Soc. Rev.* **2013**, *42*, 3614.

[5] a) G. M. Wallraff, W. D. Hinsberg, *Chem. Rev.* **1999**, *99*, 1801; b) G.-Y. Liu, S. Xu, Y. Qian, *Accounts Chem. Res.* **2000**, *33*, 457; c) R. D. Piner, J. Zhu, F. Xu, S. Hong, C. A. Mirkin, *Science* **1999**, *283*, 661.

[6] T. Ding, D. O. Sigle, L. O. Herrmann, D. Wolverson, J. J. Baumberg, *ACS Appl. Mater. Inter.* **2014**, *6*, 17358.

[7] a) B. Ai, H. Möhwald, D. Wang, G. Zhang, *Adv. Mater. Inter.* **2017**, *4*, 1600271; b) S.-M. Yang, S. G. Jang, D.-G. Choi, S. Kim, H. K. Yu, *Small* **2006**, *2*, 458-475; c) J. Zhang, Y. Li, X. Zhang, B. Yang, *Adv. Mater.* **2010**, *22*, 4249.

[8] a) Y. Li, X. Ye, Y. Ma, L. Qi, *Small* **2015**, *11*, 1183; b) H. Xiaoye, Z. Peng, M. Guowen, H. Qing, Z. Chuhong, H. Fangming, H. Zhulin, L. Zhongbo, W. Zhaoming, W. Nianqiang, *Nanotechnology* **2016**, *27*, 384001; c) S. Xu, F. Sun, S. Yang, Z. Pan, J. Long, F. Gu, *Sci. Rep.* **2015**, *5*, 8939.

[9] M. Hideki, S. Masahiro, *Jpn. J. Appl. Phys.* **1996**, *35*, L126.

[10] a) Z. Zhan, R. Xu, Y. Mi, H. Zhao, Y. Lei, *ACS Nano* **2015**, *9*, 4583; b) Z. Zhan, Y. Lei, *ACS Nano* **2014**, *8*, 3862; c) N. Lim, Y. Pak, J. T. Kim, Y. Hwang, R. Lee, Y. Kumaresan, N. Myoung, H. C. Ko, G. Y. Jung, *Nanoscale* **2015**, *7*, 13489; d) S. P. Xu, H.P. Zhao, Y. Xu, R. Xu, Y. Lei, *ACS Appl. Mater. Interfaces* **2018**, *10*, 13895.

[11] Y. Lei, S. Yang, M. Wu, G. Wilde, *Chem. Soc. Rev.* **2011**, *40*, 1247.

[12] U. C. Fischer, H. P. Zingsheim, *J. Vac. Sci. Technol.* **1981**, *19*, 881.

[13] J. C. Hulteen, D. A. Treichel, M. T. Smith, M. L. Duval, T. R. Jensen, R. P. Van Duyne, *J. Phys. Chem. B* **1999**, *103*, 3854.

[14] N. Denkov, O. Velev, P. Kralchevski, I. Ivanov, H. Yoshimura, K. Nagayama, *Langmuir* **1992**, *8*, 3183.

[15] A. S. Dimitrov, K. Nagayama, *Langmuir* **1996**, *12*, 1303.

[16] a) H. W. Deckman, J. H. Dunsmuir, *Appl. Phys. Lett.* **1982**, *41*, 377; b) J. C. Hulteen, R. P. V. Duyne, *J. Vac. Sci. Technol. A* **1995**, *13*, 1553.

[17] a) M. Kondo, K. Shinozaki, L. Bergstroem, N. Mizutani, *Langmuir* **1995**, *11*, 394; b) S. Reculusa, S. Ravaine, *Chem. Mater.* **2003**, *15*, 598; c) W. Wang, B. Gu, *J. Phys. Chem. B* **2005**, *109*, 22175.

[18] M. Retsch, Z. Zhou, S. Rivera, M. Kappl, X. S. Zhao, U. Jonas, Q. Li, *Macromol. Chem. Phys.* **2009**, *210*, 230.

[19] a) K. Kempa, B. Kimball, J. Rybczynski, Z. P. Huang, P. F. Wu, D. Steeves, M. Sennett, M. Giersig, D. V. G. L. N. Rao, D. L. Carnahan, D. Z. Wang, J. Y. Lao, W. Z. Li, Z. F. Ren, *Nano Lett.* **2003**, *3*, 13; b) A. Valsesia, P. Colpo, M. Manso Silvan, T. Meziani, G. Ceccone, F. Rossi, *Nano Lett.* **2004**, *4*, 1047; c) M. Albrecht, G. Hu, I. L. Guhr, T. C. Ulbrich, J. Boneberg, P. Leiderer, G. Schatz, *Nat. Mater.* **2005**, *4*, 203; d) J. Fischer, N. Vogel, R. Mohammadi, H.-J. Butt, K. Landfester, C. K. Weiss, M. Kreiter, *Nanoscale* **2011**, *3*, 4788; e) D. Xie, Y. Hou, Y. Su, F. Gao, J. Du, *Nanoscale Res. Lett.* **2015**, *10*, 153.

[20] B. J. Y. Tan, C. H. Sow, K. Y. Lim, F. C. Cheong, G. L. Chong, A. T. S. Wee, C. K. Ong, *J. Phys. Chem. B* **2004**, *108*, 18575.

[21] a) G. Eranna, B. C. Joshi, D. P. Runthala, R. P. Gupta, *Crit. Rev. Solid State* **2004**, *29*, 111; b) H. Ogawa, M. Nishikawa, A. Abe, *J. Appl. Phys.* **1982**, *53*, 4448; c) J. Watson, K. Ihokura, G. S. V. Coles, *Meas. Sci. Technol.* **1993**, *4*, 711.

[22] A. Gurlo, R. Riedel, *Angew. Chem.-Int. Edit.* **2007**, *119*, 3900.

[23] J. N. Zemel, *Thin Solid Films* **1988**, *163*, 189.

[24] a) N. Barsan, U. Weimar, *J. Electroceram.* **2001**, *7*, 143-167; b) N. Bârsan, U. Weimar, *J. Phys. Condens. Matter.* **2003**, *15*, R813.

[25] A. Rothschild, Y. Komem, *J. Appl. Phys.* **2004**, *95*, 6374.

[26] a) X.-H. Liu, P.-F. Yin, S. A. Kulinich, Y.-Z. Zhou, J. Mao, T. Ling, X.-W. Du, *ACS Appl. Mater. Inter.* **2017**, *9*, 602; b) J. Z. Ou, W. Ge, B. Carey, T. Daeneke, A. Rotbart, W. Shan, Y. Wang, Z. Fu, A. F. Chrimes, W. Wlodarski, S. P. Russo, Y. X. Li, K. Kalantar-zadeh, *ACS Nano* **2015**, *9*, 10313.

[27] A. Gurlo, R. Riedel, *Angew. Chem.-Int. Edit.* **2007**, *46*, 3826.

[28] a) H.-W. Yoo, S.-Y. Cho, H.-J. Jeon, H.-T. Jung, *Anal. Chem.* **2015**, *87*, 1480; b) F. Yang, K. C. Donavan, S.-C. Kung, R. M. Penner, *Nano letters* **2012**, *12*, 2924; c) G. T. Chandran, X. Li, A. Ogata, R. M. Penner, *Anal. Chem.* **2017**, *89*, 249; d) J. Sun, M. Muruganathan, H. Mizuta, *Sci. Adv.* **2016**, *2*.

[29] a) I. Cho, K. Kang, D. Yang, J. Yun, I. Park, *ACS Appl. Mater. Inter.* **2017**, *9*, 27111; b) X. Wang, N. Aroonyadet, Y. Zhang, M. Mecklenburg, X. Fang, H. Chen, E. Goo, C. Zhou, *Nano letters* **2014**, *14*, 3014; c) Y.-X. Li, Z. Guo, Y. Su, X.-B. Jin, X.-H. Tang, J.-R. Huang, X.-J. Huang, M.-Q. Li, J.-H. Liu, *ACS Sensors* **2017**, *2*, 102; d) S. Xu, F. Sun, Z. Pan, C. Huang, S. Yang, J. Long, Y. Chen, *ACS Appl. Mater. Inter.* **2016**, *8*, 3428.

[30] a) Y. Lei, W. K. Chim, H. P. Sun, G. Wilde, *Appl. Phys. Lett.* **2005**, *86*, 103106; b) L. Wen, Y. Mi, C. Wang, Y. Fang, F. Grote, H. Zhao, M. Zhou, Y. Lei, *Small* **2014**, *10*, 3162.

[31] F. Sun, W. Cai, Y. Li, L. Jia, F. Lu, *Adv. Mater.* **2005**, *17*, 2872.

[32] Y.-T. Wang, W.-T. Whang, C.-H. Chen, *ACS Appl. Mater. Inter.* **2015**, *7*, 8480.

[33] A. Tricoli, M. Righettoni, A. Teleki, *Angew. Chem.-Int. Edit.* **2010**, *49*, 7632.

[34] X. Zou, J. Wang, X. Liu, C. Wang, Y. Jiang, Y. Wang, X. Xiao, J. C. Ho, J. Li, C. Jiang, Y. Fang, W. Liu, L. Liao, *Nano letters* **2013**, *13*, 3287.

[35] S. J. Yun, S. H. Chae, H. Kim, J. C. Park, J.-H. Park, G. H. Han, J. S. Lee, S. M. Kim, H. M. Oh, J. Seok, M. S. Jeong, K. K. Kim, Y. H. Lee, *ACS Nano* **2015**, *9*, 5510.

[36] a) M. Kimura, R. Sakai, S. Sato, T. Fukawa, T. Ikehara, R. Maeda, T. Mihara, *Adv. Funct. Mater.* **2012**, *22*, 469; b) D. P. Volanti, A. A. Felix, M. O. Orlandi, G. Whitfield, D.-J. Yang, E. Longo, H. L. Tuller, J. A. Varela, *Adv. Funct. Mater.* **2013**, *23*, 1759; c) H. Wang, K. Dou, W. Y. Teoh, Y. Zhan, T. F. Hung, F. Zhang, J. Xu, R. Zhang, A. L. Rogach, *Adv. Funct. Mater.* **2013**, *23*, 4847.

[37] S.P. Xu, F. Sun, F. Gu, Y. Zuo, L. Zhang, C. Fan, S. Yang, W. Li, *ACS Appl. Mater. Inter.* **2014**, *6*, 1251.

[38] a) Z.-Y. Zhou, N. Tian, J.-T. Li, I. Broadwell, S.-G. Sun, *Chem. Soc. Rev.* **2011**, *40*, 4167; b) A. Gurlo, *Nanoscale* **2011**, *3*, 154; c) Q. Kuang, X. Wang, Z. Jiang, Z. Xie, L. Zheng, *Accounts Chem. Res.* **2014**, *47*, 308.

[39] a) J. Wu, S. Feng, X. Wei, J. Shen, W. Lu, H. Shi, K. Tao, S. Lu, T. Sun, L. Yu, C. Du, J. Miao, L. K. Norford, *Adv. Funct. Mater.* **2016**, *26*, 7462; b) L. E. Kreno, J. T. Hupp, R. P. Van Duyne, *Anal. Chem.* **2010**, *82*, 8042; c) J. X. Wang, X. W. Sun, S. S. Xie, Y. Yang, H. Y. Chen, G. Q. Lo, D. L. Kwong, *J. Phys. Chem. C* **2007**, *111*, 7671; d) W. Ma, H. Yang, W. Wang, P. Gao, J. Yao, *Sensors* **2011**, *11*, 8643.

[40] a) N. Liu, M. L. Tang, M. Hentschel, H. Giessen, A. P. Alivisatos, *Nat Mater.* **2011**, *10*, 631; b) R. Morarescu, H. Shen, R. A. L. Vallee, B. Maes, B. Kolaric, P. Damman, *J. Mater. Chem.* **2012**, *22*, 11537; c) A. J. Haes, S. Zou, G. C. Schatz, R. P. Van Duyne, *J. Phys. Chem. B* **2004**, *108*, 109.

[41] E. P. Stuckert, E. R. Fisher, *Sensor. Actuat. B: Chem.* **2015**, *208*, 379.

[42] G. K. Hall, C. H. B. Mee, *Surf. Sci.* **1971**, *28*, 598.

[43] S. Xu, Y. Xu, H. Zhao, R. Xu, Y. Lei, *ACS Appl. Mater. Inter.* **2018**, *10*, 29092.

[44] R. F. Gouveia, F. Galembeck, *J. Am. Chem. Soc.* **2009**, *131*, 11381.

[45] G. M. An, N. Na, X. R. Zhang, Z. J. Miao, S. D. Miao, K. L. Ding, Z. M. Liu, *Nanotechnology* **2007**, *18*, 435707.

[46] P. Manoravi, P. R. Willmott, J. R. Huber, T. Greber, *Appl. Phys. A* **1999**, *69*, S865.

[47] X.-X. Fan, X.-L. He, J.-P. Li, X.-G. Gao, J. Jia, *Vacuum* **2016**, *128*, 112.

[48] L. Cheng, S. Y. Ma, T. T. Wang, X. B. Li, J. Luo, W. Q. Li, Y. Z. Mao, D. J. GZ, *Mater. Lett.* **2014**, *131*, 23.

[49] J. F. Chao, X. Xu, H. T. Huang, Z. Liu, B. Liang, X. F. Wang, S. H. Ran, D. Chen, G. Z. Shen, *CrystEngComm* **2012**, *14*, 6654.

[50] Y. Zong, Y. L. Cao, D. Z. Jia, P. F. Hu, *Sens. Actuator, B* **2010**, *145*, 84.

[51] L. Li, H. M. Lin, F. Y. Qu, *J. Sol-Gel Sci. Technol.* **2013**, *67*, 545.

[52] N. H. Touidjen, B. Bendahmane, M. L. Zeggar, F. Mansour, M. S. Aida, *Sensing and Bio-Sensing Research* **2016**, *11*, 52.

[53] J. Xu, Y. S. Li, H. T. Huang, Y. G. Zhu, Z. R. Wang, Z. Xie, X. F. Wang, D. Chen, G. Z. Shen, *J. Mater. Chem.* **2011**, *21*, 19086.

[54] P. Sun, X. D. Mei, Y. X. Cai, J. Ma, Y. F. Sun, X. S. Liang, F. M. Liu, G. Y. Lu, *Sens. Actuator, B* **2013**, *187*, 301.

[55] X. C. Ma, H. Y. Song, C. S. Guan, *Sens. Actuator, B* **2013**, *177*, 196.

[56] Y. F. He, P. G. Tang, J. Li, J. J. Zhang, F. Y. Fan, D. Q. Li, *Mater. Lett.* **2016**, *165*, 50.

[57] Q. Zhao, Y. Gao, X. Bai, C. Wu, Y. Xie, *Eur. J. Inorg. Chem.* **2006**, *2006*, 1643.

[58] G. H. Chen, S. Z. Ji, H. D. Li, X. L. Kang, S. J. Chang, Y. N. Wang, G. W. Yu, J. R. Lu, J. Claverie, Y. H. Sang, H. Liu, *ACS Appl. Mater. Interfaces* **2015**, *7*, 24950.

[59] Y. L. Wang, X. C. Jiang, Y. N. Xia, *J. Am. Chem. Soc.* **2003**, *125*, 16176.

[60] K. P. Gattu, K. Ghule, A. A. Kashale, R. S. Mane, R. Sharma, D. M. Phase, S. H. Han, A. V. Ghule, *Curr. Nanosci.* **2015**, *11*, 253.

[61] L. L. Fields, J. P. Zheng, Y. Cheng, P. Xiong, *Appl. Phys. Lett.* **2006**, *88*, 263102.

7. Scientific Contributions

In total, I have published and jointly published 4 papers in SCI-indexed international scientific journals during my Ph.D. period from Sep. 2015 to Aug. 2018. Among them, I am the first author in three papers, two research articles in ***ACS Applied Materials & Interfaces*** and one review article in ***ChemPlusChem***.

I also have 9 contributions at conferences, including 5 talks and 4 posters.

Publications in SCI-Indexed Scientific Journals

1. Xu, S.P.; Zhao, H.P.; Xu, Y.; Xu, R.; Lei, Y.* Carrier Mobility-Dominated Gas Sensing: A Room-Temperature Gas-Sensing Mode for SnO_2 Nanorod Array Sensors. ***ACS Applied Materials &Interfaces*** (Impact factor: 8.097), **2018**, *10*, 13895-13902.

2. Xu, S.P.; Lei, Y.* Template-Assisted Fabrications of Nanostructured Arrays for Sensing Applications. ***ChemPlusChem*** (Impact Factor: 3.205), **2018**, *83*, 741-755.

3. Xu, S.P.; Xu, Y.; Zhao, H.P.; Xu, R.; Lei, Y.* Sensitive Gas-Sensing by Creating Adsorption Active Sites: Coating an SnO_2 layer on Triangle Arrays. ***ACS Applied Materials &Interfaces*** (Impact factor: 8.097), **2018**, *10*, 29092-29099.

4. Xu, R.; Wen, L.Y.; Wang, Z.J.; Zhao, H.P.; Xu, S.P.; Mi, Y.; Xu, Y.; Sommerfeld, M.; Fang, Y.G.; Lei, Y.* Three-Dimensional Plasmonic Nanostructure Design for Boosting Photoelectrochemical Activity. ***ACS Nano*** (Impact Factor: 13.709), **2017**, *11*, 7382-7389.

Conference Contributions

1. Xu, S.P.; Zhao, H.P.; Xu, Y.; Xu, R.; Zhang, H.M.; Liu, L.; Lei, Y. Template-Assisted Fabrications of Regular Arrays of Nanostructures for Sensitive Gas-Sensing. 82th, Annual Conference of the DPG, Mar 11- Mar 16, 2018, Berlin, Germany. Talk.

2. Xu, S.P.; Zhao, H.P.; Xu, R.; Zhang, H.M.; Liu, L.; Lei, Y. Template-Assisted Fabrications of Nanostructure-Array-Based Gas-Sensors. 82th, Annual Conference of the DPG, Mar 11- Mar 16, 2018, Berlin, Germany. Poster.

3. Xu, S.P.; Zhao, H.P.; Xu, Y.; Xu, R.; Wen, L.Y.; Lei, Y. Fabrications of Nanoporous Film and Nanowire Arrays with High Gas-Sensing Performances. 81th, Annual Conference of the DPG, Mar 19- Mar 24, 2017, Dresden, Germany. Talk.

4. Xu, R.; Wen, L.Y.; Wang, Z.J.; Zhao, H.P.; Xu, S.P.; Mi, Y.; Xu, Y.; Sommerfeld, M.; Fang. Y.G.; Lei, Y. Three-Dimensional Plasmonic Nanostructure Design for Boosting Photoelectrochemical Activity. 82th, Annual Conference of the DPG, Mar 11- Mar 16, 2018, Berlin, Germany. Poster.

5. Zhang, H.M.; Zhou, M.; Xu, Y.; Xu, S.P.; Meng, F.N.; Qi, L.H.; Chen, Y.J.; Lei Y. Enhanced Photocatalytic Activities of Net-Like Hematite Nanoparticle Modified with Graphene Oxide and Mechanism Insight. 82th, Annual Conference of the DPG, Mar 11- Mar 16, 2018, Berlin, Germany. Poster.

6. Zhang, H.M.; Zhou, M.; Xu, Y.; Xu, S.P.; Chen, Y.J.; Lei Y. Growth of Fe_3O_4 Nanorod Arrays on Graphene Sheets for Application in Electromagnetic Absorption Fields. 82th, Annual Conference of the DPG, Mar 11- Mar 16, 2018, Berlin, Germany. Talk.

7. Xu, R.; Wen, L.Y.; Zhao, H.P.; Xu, S.P.; Sommerfeld, M.; Xu, Y.; Mi, Y.; Fang. Y.G.; Lei, Y. Omnidirectional Photoelectrochemical Activity of Ultrathin CdS Film on Periodic Three-Dimensional Composite Pillar/Truncated-Pyramid Au Arrays. 81th, Annual Conference of the DPG, Mar 19- Mar 24, 2017, Dresden, Germany. Talk.

8. Liu, L.; Zhao, H.P.; Xu, Y.; Xu, S.P.; Zhang, C.L.; Zeng, Z.Q.; Lei, Y. Evaluate the Role of Nanostructure Current Collector in Supercapacitor Electrode when the Electroactive Material is in the Form of Thick Layer. 82th, Annual Conference of the DPG, Mar 11- Mar 16, 2018, Berlin, Germany. Talk.

9. Liu, L.; Zhao, H.P.; Xu, R.; Xu, S.P.; Zhang, C.L.; Lei, Y. Transparent CdS@TiO_2 Nanotextile Photoanode with Boosted Photoelectrocatalytic Efficiency and Stability. 82th, Annual Conference of the DPG, Mar 11- Mar 16, 2018, Berlin, Germany. Post.

8. Declaration

I hereby declare that this Ph.D. dissertation entitled “Template-Assisted Fabrications of Nanostructure Arrays for Gas-Sensing Applications” was carried out by me for the degree of Doctor of Philosophy under the supervision of Prof. Dr. Yong Lei. All dates and information in this dissertation those have been directly or indirectly consulted or used from other sources are clearly stated. This dissertation has not been submitted, in part or in whole, for any other degree or examination in any other University. I have acknowledged all main sources of assistances, and I have made clear exactly what was done by others and what I have contributed when the work was done jointly with others. Some of the results may have been published in scientific journals or elsewhere. I am aware that the falsity of this declaration will be regarded as an attempt of deception and will cause the derogation of the doctoral procedure.

Ilmenau, 12nd, November

Shipu Xu